# Mixed Convection in Horizontal Fluid-Superposed Porous Layers

A Dissertation

Submitted to the Faculty of the Graduate School of the University of Minnesota by

John Dixon

In partial fulfillment of the requirements for the degree of

Doctor of Philosophy

Francis A. Kulacki, Adviser

August 2013

August 2013

## Acknowledgements

I would like to thank Professor Francis A. Kulacki for his guidance, patience, and encouragement throughout my PhD studies. He set the bar high and gave me enough prodding to keep me on track. His advice and help has been invaluable. I would also like to thank Professor Terrence Simon, Professor Wojciech Lipinski, and Professor Vaughn Voller for serving on my committee and for reviewing my dissertation.

I would like to thank my wife, Amber, for her incredible support and sacrifice throughout my graduate studies. She has been such a blessing and encouragement through many difficulties. I would like to thank my 9-month old son, Micah, for being such a joy and delight. I would like to thank my parents for all their support, for instilling in me a love of learning, and for all their counsel and advice as I considered leaving my career in industry to return to graduate school. Most importantly, I thank and praise God for Jesus Christ, my rock and my salvation.

## Dedication

I dedicate this to my wife, Amber, and son, Micah.

## Abstract

Mixed convection in horizontal fluid-superposed porous layers is studied in the following work. Much research has been done in the field of natural, mixed, and forced convection in a porous layer. Several studies have investigated natural and forced convection in a two-domain system that includes a porous and a fluid layer, but mixed convection has not been addressed. This problem can be found in many natural and engineering applications. Some examples include beach sand, human lungs, bread, gravel, soil, rock, packed bed reactors, fiberglass insulation, thermal energy storage systems, electronic cooling, crude oil extraction, nuclear reactors, and the list goes on. The present study is motivated by the wide range of applications and seeks to fill the gap in the literature regarding mixed convection.

The problem considers a long, narrow channel that is partially filled with a porous layer and has a fluid layer above the porous layer. The channel is partially heated on the bottom and cross flow along the length of the channel is added in varying degrees. The problem is studied at a fundamental level, with the governing equations being derived, non-dimensionalized, discretized, and solved numerically. The two layers are treated as a single domain and the porosity is used as a switching parameter, causing the governing equations to transition from an extended form of the Darcy-Brinkman-Forchheimer equation in the porous layer to the Navier-Stokes equations in the fluid layer. This method avoids the need for interfacial boundary conditions to be explicitly defined at the interface between the two domains. Several dimensionless numbers are varied and their effects on the overall Nusselt number of the system are documented. The parameters varied include the Peclet number, the Rayleigh number, the porous layer height ratio, the Darcy number, the Prandtl number, and the conductivity ratio between the solid and fluid phases. In addition, the impact of the various additional terms in the extended form of Darcy's law is investigated and documented as well.

The conductivity ratio, Darcy number, porous layer height ratio, Rayleigh number, and Peclet number all have a strong effect on the overall Nusselt number of the system, while the Prandtl number, the Brinkman term, the Forchheimer term, and the convective terms have a negligible effect. A critical Peclet number was observed, where the Nusselt number is a minimum, and was shown to be proportional to the Rayleigh-

Darcy number and inversely proportional to the porous layer height ratio. A critical porous layer height ratio was also found, where the Nusselt number is a minimum, and was shown to be proportional to the Rayleigh-Darcy number and inversely proportional to the Peclet number. The streamlines capture the transition from the natural convection regime to the forced convection regime. In the transition region the flow patterns have characteristics of both domains. The isotherms capture the plume flow and show the influence of the cross flow on the shape and character of the plume.

An experimental apparatus is designed in order to collect data over a similar range of parameters as explored numerically. The average error between the numerical and experimental results is 30%, with a peak of 67%. The numerical results show good agreement with the experimental data within the bounds of uncertainty. The experimental results confirm the presence of a critical Peclet number. However, they do not show the same trends at intermediate porous layer height ratios. The effect of the porous layer height ratio, $\eta = h_p/H$, on the Nusselt number is shown to be small in the range of $\eta = 0.5$ to $\eta = 1$ and large in the range of $\eta = 0$ to $\eta = 0.5$. Also, the transition to the forced convection regime occurs earlier for the numerical results than it does for the experimental results. This points towards future research opportunities that focus on the lower range of porous layer height ratio values.

## Table of Contents

## List of Tables

## List of Figures

## Nomenclature

A – constant in variable porosity equation
$a_{fs}$ – surface area per unit volume
$c_f$ – Forchheimer drag coefficient
$c_p$ – specific heat
$Da = \frac{K}{H^2}$ – Darcy number
$d_p$ – particle diameter
g – acceleration due to gravity
h – convection coefficient
H – height of the total chamber
$h_p$ – height of the porous layer
K – permeability
k – thermal conductivity
$L_h$ – length of the heater
N – total number of grid points
$N_x$ –number of grid points in x-direction
$N_y$ – number of grid points in y-direction
$Nu = \frac{q"H}{k_m \Delta T}$ – Nusselt number
P – pressure
$Pe = \frac{U_0 H}{\alpha_f}$ – Peclet number
Pr – Prandtl number
$q'''$ – volumetric energy generation rate
$Ra = \frac{g\beta H^3 \Delta T}{\nu \alpha_f}$ – Rayleigh number
$RaDa = \frac{Kg\beta H \Delta T}{\nu \alpha_f}$ – Rayleigh-Darcy number
$Ri = \frac{RaPr}{Pe^2}$ – Richardson number
$Re = \frac{Pe}{Pr} = \frac{U_0 H}{\upsilon}$ – Reynolds number
T – temperature
$U_0$ – average cross flow velocity
$\mathbf{v}$ – velocity
$|\mathbf{V}|$ – velocity magnitude
w – weighting factor

Greek Symbols
α – thermal diffusivity
$\propto_{BJ}$ – Beavers-Joseph coefficient
β – coefficient of volumetric expansion
$\eta = {h_p}/{H}$ – dimensionless height ratio

μ – fluid viscosity
$\tilde{\mu}$ – Brinkman viscosity
ϕ – porosity
$\kappa = {k_s}/{k_f}$ – conductivity ratio

$\lambda = {k_e}/{k_f}$ – effective conductivity ratio

$\delta = \frac{L_h}{H}$ – dimensionless heater length
Ψ – stream function
σ – specific heat ratio of porous domain
ρ – density
$\tau = {t\alpha_f}/{H^2}$ – dimensionless time

$\theta = \frac{T - T_0}{T_h - T_0}$ – dimensionless temperature
ω – vorticity

Subscripts
0 – initial/free stream condition
B – boundary grid point
D – based on heater length
e – effective value
f – fluid phase
s – solid phase
fs – solid-fluid interface in porous medium
m – average/stagnant value of two phases
H – based on total height
*e, w, n, s* – boundaries of grid point
E, W, N, S – adjacent grid points
P – current grid point

# Chapter 1. Introduction

The motivation for this study is to move forward the fundamental understanding of heat transfer in porous media. Much work has been done in this field over the years, but there remain many open problems. Mixed convection in horizontal fluid-superposed porous layers is an open question that has not been addressed in the literature. One open issue in this field is in handling the interface between the overlying pure fluid layer and the porous layer. Much work has been done in this area over the years [1-7], but nothing has been produced that is directly applicable to buoyancy-driven flows.

Recent work [1] studying natural convection in horizontal fluid-superposed porous layers heated from below has shown disagreement between numerical predictions and experimental results. This could be due to the limitations of the current methods being used and further highlights the need for an appropriate method to handle the interface between the pure fluid layer and fluid-saturated porous layer.

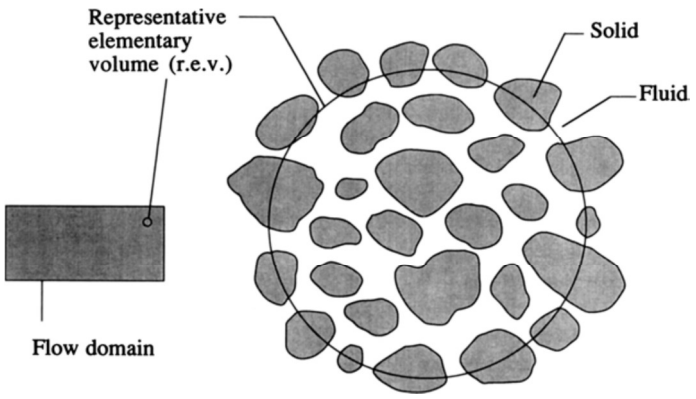


Figure 1. Representative elementary volume (REV) of a larger flow domain [2].

From the earliest stages of porous media research, the mathematical approach has been to treat the porous medium as a continuum, using a representative elementary volume (Figure 1) that averages out any pore-size flow characteristics, replacing them with a larger scale average value.

Carefully defining the geometry and using the Navier-Stokes equations would certainly be a valid (and more accurate) approach to solving the problem, but using this averaging scheme allows for great simplification of the problem. However, as with the study of turbulence, some physics of the problem are lost in the process of averaging, and

they need to be carefully added back in. Herein lays the challenge of defining the boundary conditions between a fluid and a porous layer.

The objectives of the proposed work are:

1. Obtain a numerical solution to the problem of mixed convection in horizontal fluid saturated porous layers heated from below with a variable porous layer height.
2. Determine a suitable method for handling the boundary between a fluid and porous layer for buoyancy-driven flows. Use this method to numerically solve the problem and determine the Nusselt/Peclet/Rayleigh number correlations.
3. Construct a test apparatus and collect experimental data to verify the numerical results.

Porous media can be found in many naturally occurring applications as well as engineering applications. Some examples include beach sand, human lungs, bread, gravel, soil, rock, and engineering applications include packed bed reactors, fiberglass insulation, thermal energy storage systems, electronic cooling, crude oil extraction, nuclear reactors, and the list goes on. For many of these applications, depending on the flow regime, buoyancy effects could play a major role in the total heat transfer, and many of these applications consist of a porous medium bounded by a non-porous medium. Clearly, mixed convection in superposed fluid and porous layers is an important problem to consider. Although there are many applications, the fundamental understanding of mixed convection in adjacent fluid and porous layers is lacking. There is very limited research addressing this application, and the treatment of the boundary conditions between the fluid and porous layers is not necessarily sufficient for careful study.

Heat transfer and fluid flow in porous media has been studied for over 150 years. At present, there are over 200 papers on the topic per year being published [2]. Textbooks are available that provide clear derivations of the governing equations and give a condensed review of the relevant subsequent literature. In particular, Nield and Bejan [2] provide a critical review of literature up through 2006, and Whitaker [3]

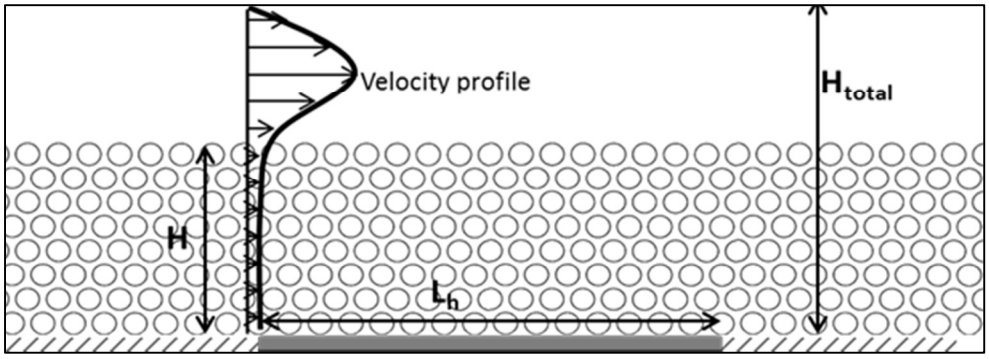

Figure 2. Mixed convection in horizontal fluid superposed porous layers.

thoroughly derives various forms of Darcy's Law and other relevant equations through an exposition of volume averaging methods.

The problem under consideration in this study is mixed convection in horizontal fluid-superposed porous layers heated from below. This problem has not directly been addressed in the literature to date, but similar problems have been considered that can provide valuable insight. Mixed convection in porous media has been considered by many authors, and solutions/correlations exist for a wide variety of problems.

# Chapter 2. Literature Review

As previously stated, heat transfer and fluid flow in a porous medium is an active field of research, with over 200 publications being published every year. In conducting a literature review in such a broad field, countless papers are available, but only a selection of them shed light on the problem of the current study. It is the goal of this literature review to first, review the historical development of the governing equations for porous media, including a justification of the terms being used, second, to review the relevant research regarding the interfacial boundary conditions between the porous and the pure fluid layers, third, to review the relevant (but limited) literature on mixed convection in porous layers, and fourth, to review recent work studying natural convection in fluid-superposed porous layers, which includes both porous and pure fluid layers.

## 2.1 Governing Equations in Porous Media

Darcy's Law was first established in 1856 [2], and is given as,

$$v = -\frac{K}{\mu}\nabla P. \tag{1}$$

This equation directly relates the bulk velocity (the Darcy velocity, drift velocity, etc) to the pressure gradient, the fluid viscosity, and K, the permeability, which is only dependent on the geometry of the porous medium. This equation is simple and easy to use, but it can clearly be seen that it does not allow for any variation in the velocity profile due to boundaries (solid or otherwise). For a fixed pressure gradient (which is typical of most flow problems being considered), the velocity profile is flat, thus ignoring any edge effects due to solid or free boundaries.

The Forchheimer term was later added to account for inertial effects in the flow [4]. Proper definition of the constant on the Forchheimer term ($c_f$) has been debated [2,5], but the general form is,

$$\nabla P = -\frac{\mu}{K}v - c_f K^{-\frac{1}{2}}\rho_f |v| v. \tag{2}$$

The Forchheimer term is also known as the quadratic drag term, and becomes significant at higher flow velocities. The pressure drop for fluid flow through an orifice/pipe/fitting/nozzle is proportional to the square of the fluid velocity, so including the Forchheimer term provides a more physically realistic governing equation. However, the Forchheimer term can safely be neglected at the typical low flow velocities found in many porous media applications.

Brinkman [6] then derived a new equation treating the problem as flow over a sphere, resulting in what is commonly known as the Brinkman equation,

$$\nabla P = -\frac{\mu}{K} v + \tilde{\mu} \nabla^2 v. \tag{3}$$

This equation is very similar to Darcy's Law, but the Brinkman term is not universally accepted, has a limited range of validity, and is typically negligible outside of boundary regions [2]. In this equation, $\tilde{\mu}$ is the porous viscosity, which is often taken as equal to the fluid viscosity, although it is not necessarily equal [2]. It can clearly be seen that including the Brinkman term will allow for variation in the velocity profile as would be found near solid boundaries or other boundary conditions.

To account for time varying flow in porous media, authors used the work of Wooding [7] and added similar acceleration terms (Eqn. (4)), but the appropriateness of these additions has been questioned [2,5],

$$\rho_f \left[ \phi^{-1} \frac{\partial v}{\partial t} + \phi^{-2} (v \cdot \nabla) v \right] = -\nabla P - \frac{\mu}{K} v. \tag{4}$$

In particular, the convective term was considered to be an inappropriate expression of the non-linear drag forces, and the Forchheimer term is preferred. Other expressions have been suggested to account for the transient effects [2], but they are shown to be negligible for any practical application. In fact, even for liquid metal flowing through an exceptionally high permeability medium, the characteristic time is still much less than one second [2]. Thus, transient terms can safely be neglected for most applications. It

should also be noted that the inclusion of the porosity on the transient and convective terms is ad hoc and no rigorous development or justification is available [5].

Furthermore, when considering the effects of buoyancy, an additional term is added to Darcy's law,

$$v = -\frac{K}{\mu}(\nabla P + \rho g). \tag{5}$$

The Boussinesq approximation allows the density in the buoyant term to vary linearly with temperature, and is widely used when the temperature variation is not too large. However, Carr and Straughan [8] considered water near freezing, and have suggested using a quadratic function that allows for the minimum density of water to occur at 4 $^{o}$C.

Combining the Forchheimer, Brinkman, Wooding, and buoyancy terms with Darcy's law, and using the Boussinesq approximation, provides Eqn. (6), which governs flow in a porous medium,

$$\rho_f\left[\phi^{-1}\frac{\partial \mathbf{v}}{\partial t} + \phi^{-2}(\mathbf{v}\cdot\nabla)\mathbf{v}\right] = -\nabla P - \frac{\mu}{K}\mathbf{v} + \tilde{\mu}\nabla^2\mathbf{v} - \frac{c_f\rho_f|\mathbf{v}|\mathbf{v}}{K^{\frac{1}{2}}} - \rho_0\mathbf{g}\big(1-\beta(T-T_0)\big). \tag{6}$$

To review, the left-hand side of Eqn. (6) represents the transient and convective terms, which are typically negligible. The first term on the right-hand side is the pressure gradient, which is the driving force of any bulk flow. The second term on the RHS represents the linear drag forces and the fourth term represents the quadratic drag forces. The third term accounts for the edge effects in the flow, and without it, the basic velocity profile would be uniform. The fifth term accounts for the buoyancy effects and works in the direction of gravity.

The development of the energy equations for a porous medium is much less debated than the development of the flow equations. However, there are several unique aspects to consider due to the two-phase nature of a porous medium. The basic energy equations are given as [2],

$$(1-\phi)\rho_s c_{p,s}\frac{\partial T_s}{\partial t} = (1-\phi)\nabla\cdot(k_s\nabla T_s) + (1-\phi)q_s''' \tag{7}$$

$$\phi\rho_f c_{p,f}\frac{\partial T_f}{\partial t} + \rho_f c_{p,f}\mathbf{v}\cdot\nabla T_f = \phi\nabla\cdot(k_f\nabla T_f) + (1-\phi)q_f''', \tag{8}$$

where Eqn. (7) represents the temperature of the solid phase and Eqn. (8) represents the temperature of the fluid phase. Heat transfer between the solid and fluid phases occurs at the solid-fluid interface. Heat transfer between the phases has been handled in different ways [2,3], but the results are most simply explained by defining an effective heat transfer coefficient between the two phases,

$$(1-\phi)\rho_s c_{p,s}\frac{\partial T_s}{\partial t} = (1-\phi)\nabla\cdot(k_s\nabla T_s) + (1-\phi)q_s''' + h_{fs}(T_f - T_s) \tag{9}$$

$$\phi\rho_f c_{p,f}\frac{\partial T_f}{\partial t} + \rho_f c_{p,f}\mathbf{v}\cdot\nabla T_f = \phi\nabla\cdot(k_f\nabla T_f) + (1-\phi)q_f''' + h_{fs}(T_s - T_f). \tag{10}$$

Determining the values of the inter-phase heat transfer coefficient, $h_{fs}$, remains a challenge, but they were experimentally determined by Polyaev [9] and shown to be in general agreement with the theoretical work of Dixon and Cresswell [10]. For a porous bed of particles, the following formulas define the heat transfer coefficient [2], where $a_{fs}$ is the surface area per unit volume, $d_p$ is the particle diameter, and B = 10 for spherical particles,

$$h_{fs} = a_{fs}h^* \tag{11}$$

$$a_{fs} = 6(1-\phi)/d_p \tag{12}$$

$$\frac{1}{h^*} = \frac{d_p}{Nu_{fs}k_f} + \frac{d_p}{Bk_s} \tag{13}$$

$$Nu_{fs} = \left(\frac{0.255}{\phi}\right)Pr^{1/3}Re_p^{2/3}. \tag{14}$$

Although other models have been proposed, they were shown to have good agreement and will be omitted from the present review [11].

Thorough analysis of this interface heat transfer has been conducted [3,7] and volume averaging techniques have been employed, resulting in criteria for local thermal

equilibrium. In many practical applications it is often appropriate to make the assumption of local thermal equilibrium, allowing the solid and fluid phase at any given point to be at equal temperature. The criteria are always met for steady-state problems and reduces the energy equations to a single governing equation,

$$\rho_m c_{p,m} \frac{\partial T}{\partial t} + \rho_f c_{p,f} \mathbf{v} \cdot \nabla T = \nabla \cdot (k_m \nabla T) + q'''_m, \tag{15}$$

where the subscript m represents the volume averaged, or combined properties of the two-phase system. Furthermore, the volume averaged properties are defined,

$$\rho_m c_{p,m} = (1 - \phi)\rho_s c_{p,s} + \phi \rho_f c_{p,f} \tag{16}$$

$$q'''_m = (1 - \phi) q'''_s + \phi q'''_f. \tag{17}$$

The thermal conductivity of the combined system can be far more complicated, but in the most basic case is defined,

$$k_m = (1 - \phi) k_s + \phi k_f. \tag{18}$$

Much research exists to further develop the effective thermal conductivity in a fluid saturated porous medium and is explored in the following section.

## 2.2 Effective Thermal Conductivity

Characterizing the heat transfer and fluid flow characteristics in a porous medium at present requires large-scale averaging of the flow. In the process of this large-scale averaging, the pore level physics are lost and are added back in a variety of creative ways. At the start, the relevant physics should be discussed to provide a context for the various ‘corrections’ to be reviewed.

For example, consider a porous medium of glass spheres filled with stagnant water and a heater at the bottom. Heat is transferred from the heater up into the water and into the glass spheres, and as you might expect, the overall thermal conductivity is

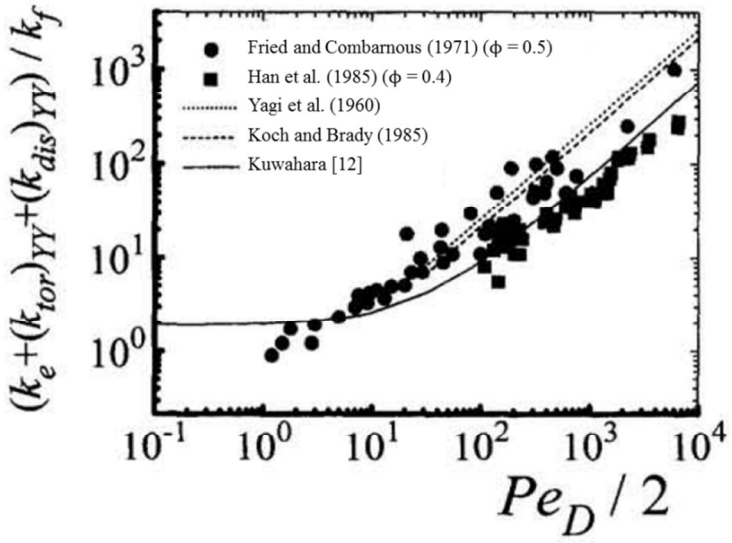


Figure 3. Correlation between Peclet number and overall effective thermal conductivity ratio [12].

some average of the value of water and the value of the glass spheres. The resulting value would depend on the amount of each of the phases (porosity), on the arrangement of the solid phase, and on the conductivities of each of the two phases. But next consider how this changes when there is motion of the fluid. Darcy's Law provides the bulk flow velocity, which may appear very laminar and orderly, but at the pore level the flow actually behaves much differently. Every glass sphere that is encountered splits the flow, forcing part of the stream upward and part downward, effectively dispersing the flow. Due to this, the flow path is not a straight line, but a much more tortuous path. In laminar flow in pure fluids, heat transfer perpendicular to the flow occurs strictly through conduction in the fluid, but flow in porous media much more effectively transfers the heat in the direction perpendicular to the flow due to the tortuosity and dispersion. This effect is well described in the numerical work of Kuwahara, Nakayama, and Koyama [12]. This dispersion not only affects the heat transfer, or thermal conductivity, but also the momentum transfer, or viscosity.

Many other creative and distinct approaches have been made over the years that include the effects of dispersion on heat and momentum transfer in porous media. For

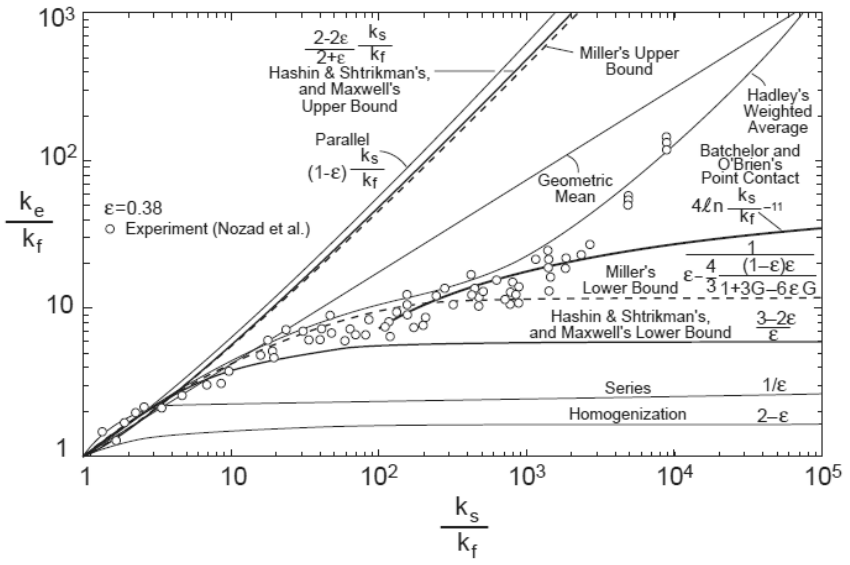


Figure 4. Summary of correlations for effective thermal conductivity [5].

the most general case of a non-isotropic porous media with varying flow direction, a full dispersion tensor can be used [3], defining unique values for each direction. For more simple cases, two terms, a longitudinal dispersion and a transverse dispersion term are separately defined [2,13], with the longitudinal dispersion in the direction of the streamlines and the transverse dispersion perpendicular to the streamlines. However, for easy implementation into standard numerical and analytical schemes, a single, effective value is preferred. Many authors have approached this problem and have developed correlations and theoretical predictions for a large range of values.

A recent monograph [14] thoroughly reviews the various approaches and methods for determining the effective thermal conductivity, and further review will not be considered in the present study. The effective thermal conductivity is shown to be a function of the solid-fluid conductivity ratio, the porosity, the nature of the solid phase (foam metal matrix verses monodisperse spherical particles verses polydisperse miscellaneous shapes, etc.), and the geometry of the solid-fluid interface. Many correlations are provided that are applicable to the present study. However, for low conductivity ratios (such as that found in the present study), most of the methods produce quite similar results and there is negligible difference between most of the models. It should also be noted that the results shown in Figure 4 do not include the effects of dispersion due to bulk motion of the fluid.

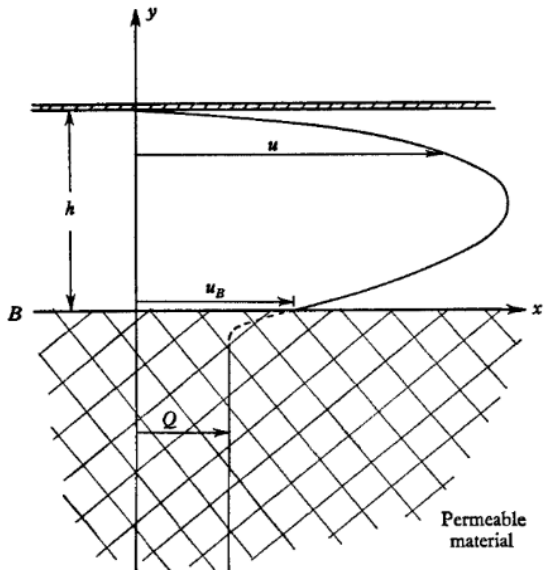

Figure 5. Flow domain for Beavers and Joseph experiments [9].

It is important to properly account for the effects of dispersion due to bulk motion of the fluid. Combining the existing experimental data, correlations have been developed [15] that provide both the longitudinal and transverse dispersion coefficients, increasing the effective diffusivity in both directions. Depending on the geometry of the porous medium and the local Peclet number, the transverse dispersion can be approximately equal to the longitudinal dispersion or can be up to 100 times greater [16]. Practically speaking, however, at high flow rates, the bulk of the longitudinal heat transfer occurs due do convection, not conduction, so this difference may not need to be accounted for.

## 2.3 Interfacial Boundary Conditions

The initial work considering the interfacial boundary conditions between a porous layer and a fluid layer was conducted by Beavers and Joseph in 1967 [17]. At the point of their research, the most basic form of Darcy's law was being used, providing a flat velocity profile in the porous region, and a no-slip velocity profile was used at the interface between the porous region and the pure fluid region, fixing the edge velocity in the fluid region to be equal to that of the porous region. However, experimental data of Poiseuille flow over a porous block showed higher than expected flow rates.

As can be seen in Figure 5, the velocity at the interface is shown to be higher than the velocity in the porous region. This boundary condition is known as a slip velocity and is determined by,

$$\frac{\partial u_f}{\partial y} = \frac{\propto_{BJ}}{K^{1/2}}(u_f - u_m). \tag{19}$$

This result provides a simple and elegant way of calculating the velocity profile, provided the constant, $\propto_{BJ}$ is known, which must be determined experimentally [2]. Neale and Nader [18] showed that the Brinkman term in Darcy's Law can be used instead of the Beavers-Joseph boundary condition to achieve the same result.

Jones [19] built on the work of Beavers and Joseph, but considered flow over a thin spherical shell. He assumed the slip velocity was based on the shear stress, resulting in an equation that considers both horizontal and vertical velocity components. However, this relation has not yet been verified [20],

$$\frac{\partial u_f}{\partial y} + \frac{\partial v_f}{\partial x} = \frac{\propto_{BJ}}{K^{1/2}}(u_f - u_m). \tag{20}$$

Ochoa-Tapia and Whitaker [21-23] use volume averaging methods to develop boundary conditions that have a jump in the stress and the heat flux, but not the velocity or temperature, and Sahraoui and Kaviani [24] propose a slip in the temperature and continuity in the heat flux, velocity, and shear stress. Experiments are required, however, to determine an unknown parameter in each of their formulations.

Alamzi and Vafai [25] show that all of these boundary conditions produce similar results for Poiseuille flow, but no other conditions were considered. They find small discrepancies in the fluid flow at the interface, smaller discrepancies in the temperature profiles, and even smaller discrepancies in the Nusselt number predictions. However, all of these boundary conditions have been developed for simple Poiseuille flow and have neglected the effects of buoyancy and flow normal to the interface.

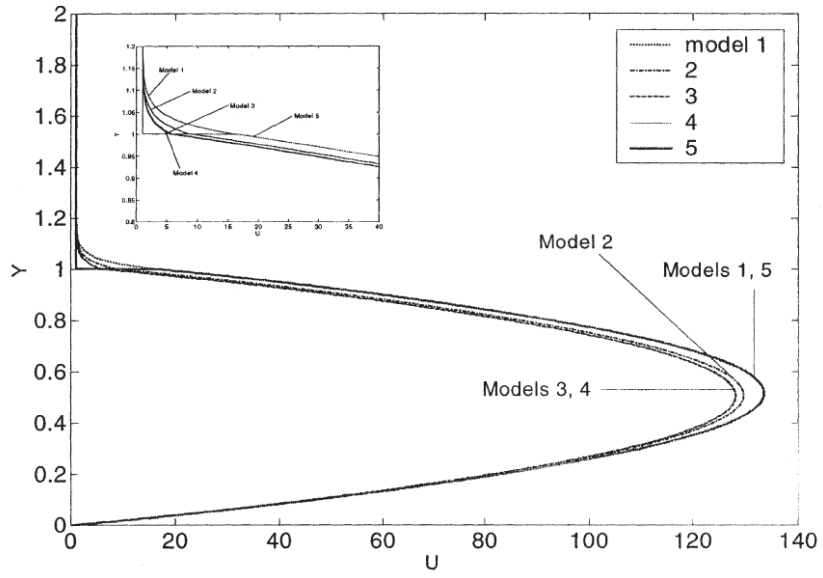


Figure 6. Velocity profile for various interfacial boundary conditions [25].

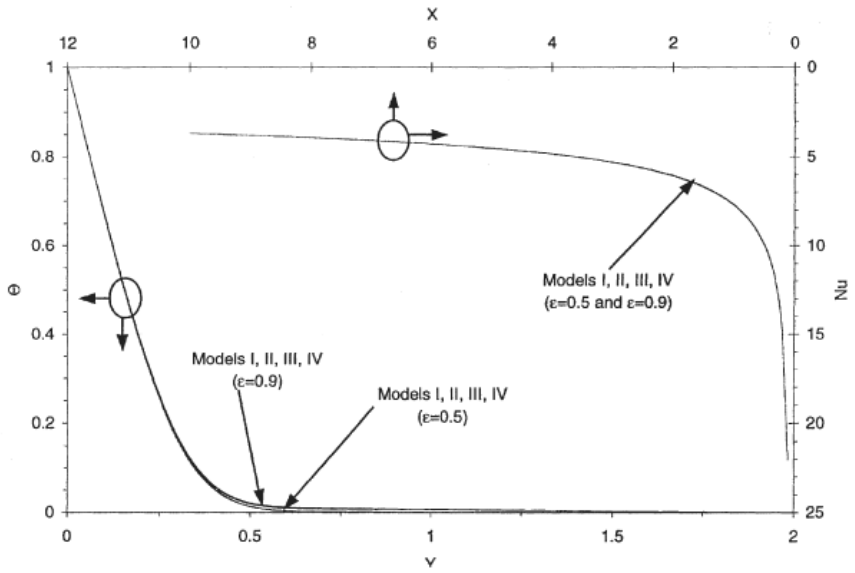


Figure 7. Temperature and Nusselt number for various interfacial boundary conditions [25].

Some modern work has used lattice Boltzmann numerical methods to investigate the interfacial boundary conditions. Nabovati [26] considered parallel flow and confirmed the slip parameter of Beavers-Joseph, finding it to depend on the porosity. Bai and Yu [27] also implement lattice Boltzmann methods, considering flows other than Poiseuille flow, and using Ochoa-Tapia and Whitaker's stress-jump boundary conditions. Both Nabovati and Bai and Yu neglect buoyancy effects. The lattice Boltzmann methods

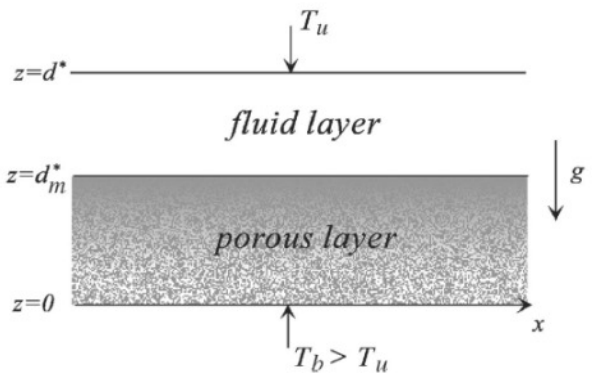


Figure 8. Problem domain for natural convection with fluid-superposed porous layers heated from below [28].

confirm prior findings, but they have not yet provided new insights into the boundary conditions between porous and fluid layers.

## 2.4 One Domain Formulation

When considering convection in a porous medium with an overlying fluid layer there are two distinct domains – the porous domain and the pure fluid domain. In the porous domain, some form of Darcy's Law governs the flow, and in the pure fluid domain, the Navier-Stokes equations govern the flow. The approach thus far has kept each of the two domains separate and has joined them with a variety of interfacial boundary conditions. However, some authors [1,28] use a form of Darcy's Law that reduces to the Navier-Stokes equations as the porosity goes to unity, allowing for the problem to be treated as a single domain, thus, avoiding the need to explicitly define interfacial boundary conditions. This method allows for a far simpler numerical solution in many situations.

Hirata [28] considered the problem of natural convection in a porous layer with an overlying pure fluid layer (Figure 8). He considered both the one domain and the two domain approaches and showed that the one domain approach can be made to match the results of the two domain approach, provided that the sharp change in porosity at the interface be properly accounted for. Hirata accomplished this by defining the porosity, Darcy number, and thermal diffusivity with Heaviside (step) functions and included the derivatives of these functions in the mathematical formulation. This effectively added

variable porosity terms to the source term at the interface, but nowhere else in the domain.

Bagchi [1] thoroughly reviewed the literature for the study of natural convection in porous media. In particular, he reviewed the problem of natural convection in a saturated porous layer with an overlying pure fluid layer. Although historically the two domain approach was standard, in more recent years, the one domain approach has been widely used, and will be used for the present study. That said there is still much to consider regarding the proper handling of the interface.

## 2.5 Mixed Convection in Porous Media

Mixed convection in porous media has been studied by many authors over the years. The work of these authors has provided a great deal of insight into the present study, even though the specific problem of mixed convection in a horizontal porous layer with an overlying pure fluid layer has not been addressed in the literature. In addition, studies of natural convection in porous layers, particularly in porous layers with an overlying pure fluid layer, also provide valuable insight into the present study.

Wooding [29] first studied mixed convection in porous media, studying the theoretical effect of large Reynolds number on the convection characteristics of the system. Prats [30] continued the theoretical study, considering the effect of cross flow on the convection currents. Sutton [31] revisited the classical 'onset of convection' problem, but included a net cross-flow, and was the first to discover that the critical Rayleigh number increases with the increasing cross flow. As the flow rate approaches zero, the critical Rayleigh number approaches the theoretical limit of $Ra_c = 4\pi^2$. This result was confirmed by Homsy and Sherwood [32], who also showed that reversing the flow direction does not change the results.

Rubin [13] studied the effect of heat dispersion due to bulk fluid motion, allowing for different thermal diffusivity in the transverse and longitudinal directions. His theoretical results further confirmed the finding that the critical Rayleigh number increases with an increasing Peclet number.

Combarnous and Bia [33] experimentally studied mixed convection in horizontal layers at low Peclet numbers. Their data did not show any change in the onset of

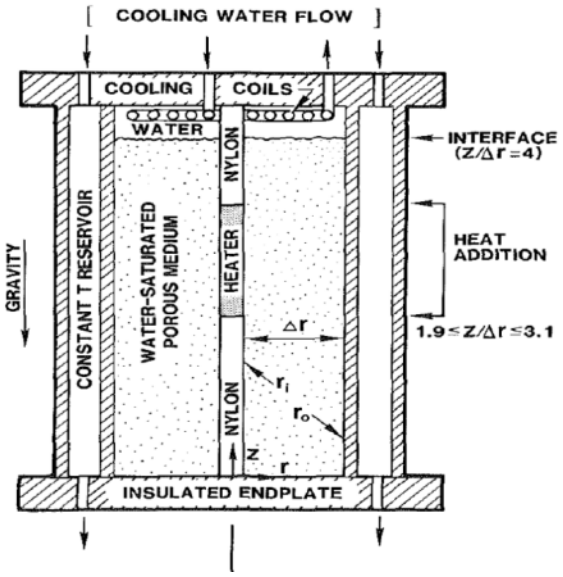


Figure 9. Experimental diagram for Reda mixed convection study [34].

convection due to cross flow. Reda [34] later conducted mixed convection experiments in a vertical chamber around a cylindrical heat source with the flow opposing the buoyancy-induced upward motion (Figure 9), showing that the parameter of Ra/Pe characterizes the heat transfer of the system. It was found that the transition from mixed to forced convection occurs at approximately Ra/Pe = 0.5, independent of the size of the heater or the amount of total power.

Lai and Kulacki published a series of papers studying mixed convection in porous media analytically, numerically, and experimentally. Transient mixed convection in horizontal porous layers with localized heating from below over a range of Peclet and Rayleigh numbers was investigated [35-37]. The results showed steady behavior in the buoyancy-dominated and forced flow dominated regimes, but oscillatory behavior in the transition region between natural and forced convection (Figure 10). This oscillatory behavior was initially shown to stabilize, but later findings disagreed [36], showing ongoing oscillations with a period,

$$\tau_p = 2.41\mathrm{Pe}^{-1.096}. \tag{21}$$

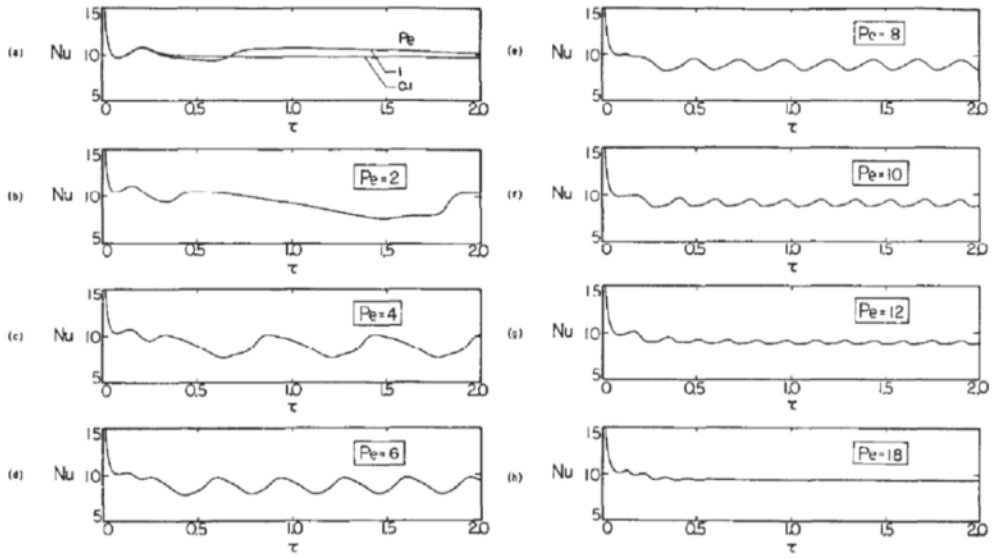


Figure 10. Oscillations in mixed convection heat transfer in a porous medium [36].

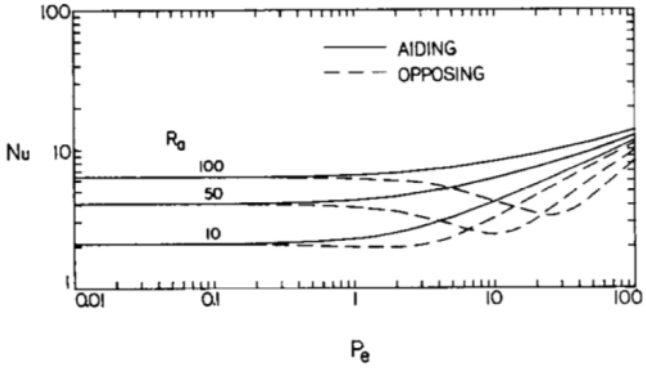


Figure 11. Aiding and opposed mixed convection in vertical flows [38].

Vertical flows in porous media with a local vertical heat source were considered [38]. Numerical solutions were obtained using the basic form of Darcy's law with the buoyancy term included. In the opposed flow case, the results show a critical Peclet number that results in a minimum heat transfer rate, but no such minimum was shown to occur in aided flow (Figure 11).

The same problem was later considered but included the Forchheimer term and the effect of thermal dispersion in their governing equations [37]. Similarity solutions were obtained and it was shown that including the Forchheimer term decreased the Nusselt number, but including the effects of dispersion greatly increased the Nusselt number. The general form of the correlations remained the same. Horizontal flow over a

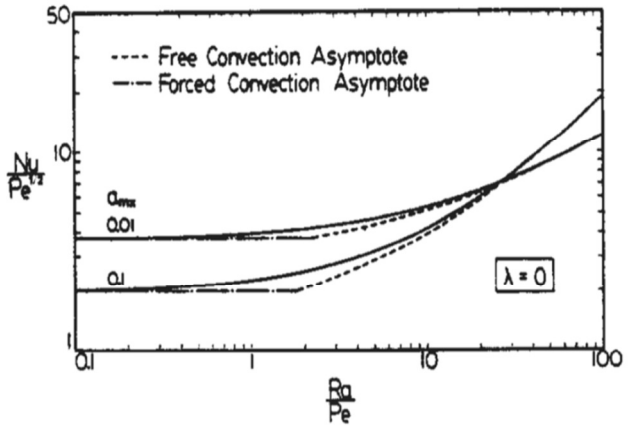


Figure 12. Mixed convection over a body of revolution [39].

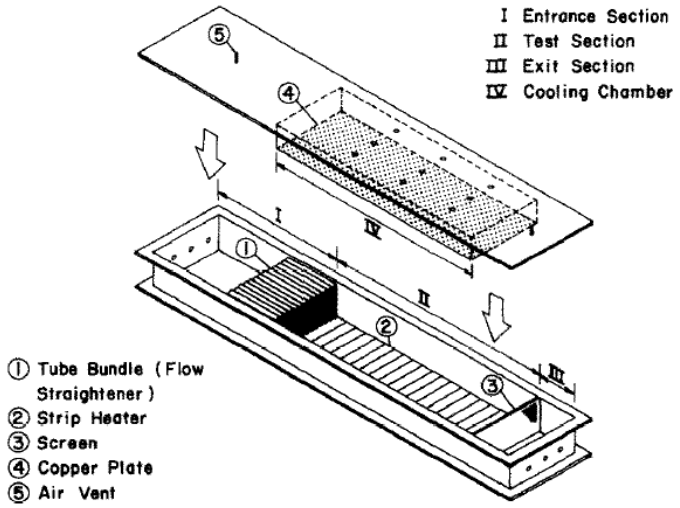


Figure 13. Experimental apparatus for mixed convection in porous media heated from below [40].

slender body of revolution was then considered [39]. Similarity solutions were obtained and the results (Figure 12) show a natural convection asymptote and a forced convection asymptote.

Mixed convection in horizontal porous layers heated locally from below was then experimentally studied [40]. A long test chamber was constructed (Figure 13), with three different sizes of heater length tested over a range of Rayleigh and Peclet numbers ($1 < \delta < 5$, $1 < Ra < 1000$, and $0.1 < Pe < 120$). Spherical glass beads filled the test section and fluid was forced horizontally through the chamber. The top surface was maintained at a constant temperature by circulating cooling water over a copper plate. The heater was placed towards the beginning of the porous region and the power input, heater

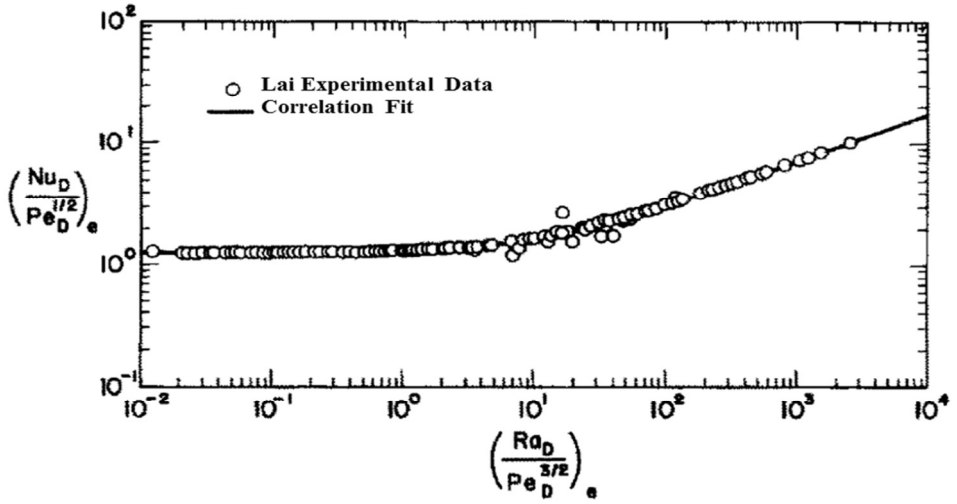


Figure 14. Corrected experimental results from mixed convection in porous medium study [40].

temperature, and inlet/ceiling temperatures were all measured. Using a more sophisticated (though not justified) effective thermal conductivity, Lai was able to correct the experimental results, leading to near perfect agreement between numerical and experimental data. Initially, the stagnant thermal conductivity was used to calculate the Nusselt number from the experimental data, however, Figure 14 shows the corrected data, which has excellent agreement. The effective thermal conductivity was calculated with the following equations,

$$k_e = (1 - w)k_m + wk_f, \tag{22}$$

$$w = 1 - \frac{Nu_{conduction}}{Nu_m}. \tag{23}$$

This method of correcting the Nusselt number leads to,

$$\frac{Nu_D}{Pe_D^{1/2}} = \left[1.895 + 0.200\left(\frac{Ra_D}{Pe_D^{3/2}}\right)\right]^{0.375} \text{ for corrected experimental data, and} \tag{24}$$

$$\frac{Nu_D}{Pe_D^{1/2}} = \left[1.917 + 0.210\left(\frac{Ra_D}{Pe_D^{3/2}}\right)\right]^{0.372} \text{ for numerical results.} \tag{25}$$

In addition, the critical Peclet number was numerically confirmed, but could not be shown experimentally (Figure 15).

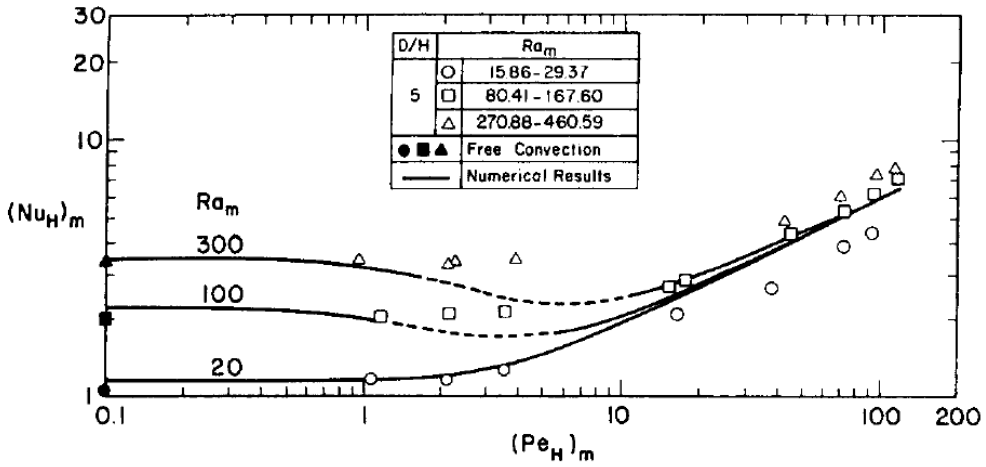


Figure 15. Discrepancy in critical Peclet number between numerical and experimental results [40].

It should also be noted that these correlation results show the independent parameter to be $Ra/Pe^{3/2}$, while the results of many prior studies reviewed showed $Ra/Pe$ while both show the independent parameter as $Nu/Pe^{1/2}$. Experiments were repeated [41], only with a sudden expansion at the beginning of the chamber (same as that shown in Figure 13) just prior to the heater, but this time the critical Peclet number was observed and is shown in Figure 16. Correlation equations showed similar results to those of prior studies, but it was also shown that the inclusion of non-Darcy terms had a negligible effect even beyond Pe = 100.

A series of papers by various authors studied mixed convection about a line source in an infinite fluid-saturated porous domain. Pop, Ingham, and Miskin [42] developed a similarity solution using the Darcy equation with the buoyancy terms included. Jang and Shiang [43] used an implicit finite difference method to numerically solve the Darcy-Brinkman-Forchheimer equation. Nakayama [44] divided the flow regime into five distinct regions (Figure 18) and presented similarity solutions for each region, showing where the addition of the Forchheimer and/or buoyancy terms is necessary. Zhou and Lai [45] numerically solved the vertical flow problem over a range of Reynolds number from 10 to 100 and Grashoff number from 0 to 400 using Darcy's

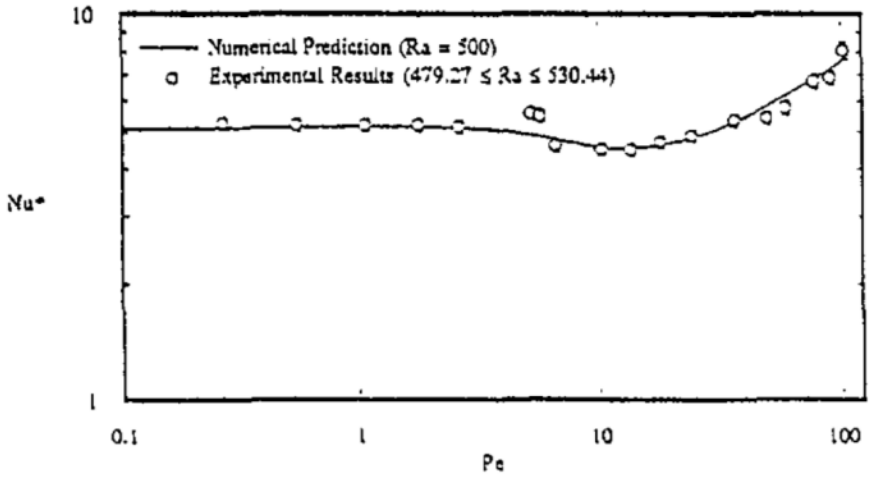


Figure 16. Experimental results showing critical Peclet number [41].

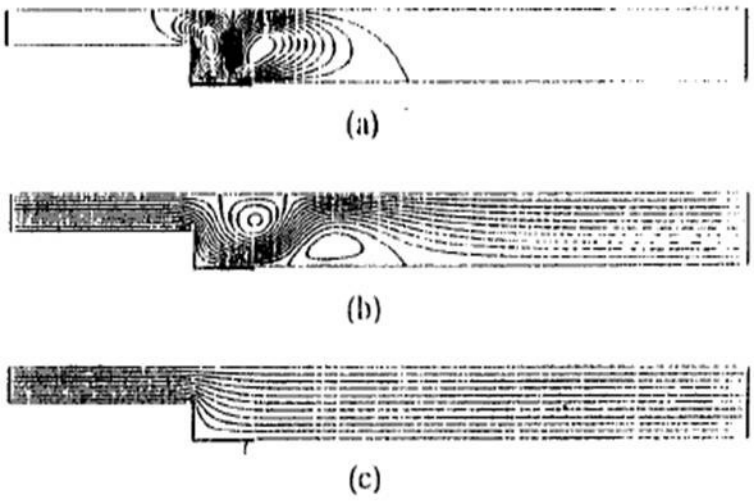


Figure 17. Streamlines of transitional flow in mixed convection [41]
a) Pe=1, b) Pe=10, c) Pe=100.

equation with the addition of the buoyancy term. The oscillatory behavior was again observed for opposed flow, and streamlines and isotherms showing the transient behavior were presented (Figure 19).

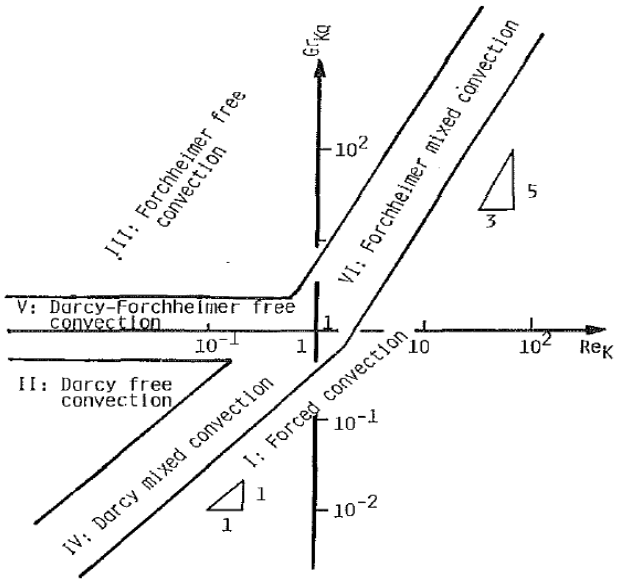


Figure 18. Flow regimes for mixed convection in porous media [44].

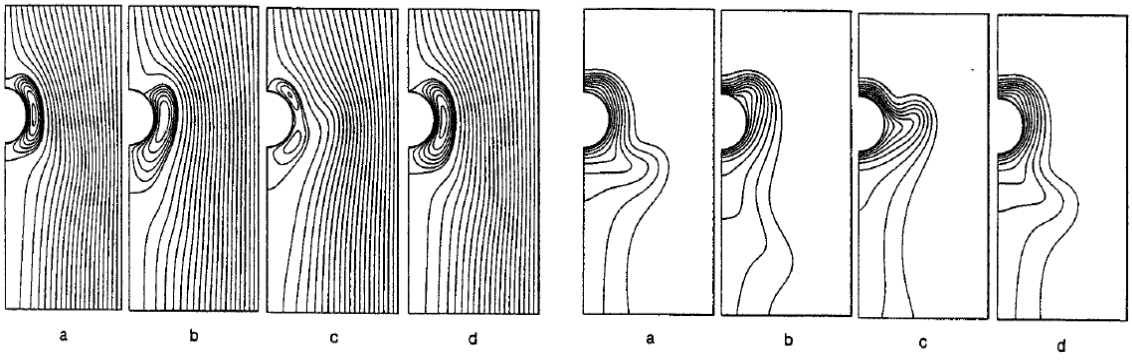


Figure 19. Streamlines and isotherms for transient opposing flow of mixed convection about a cylinder [45].

Kumar, Umavathi, and Pop [46] first considered mixed convection with both a pure fluid layer and a fluid-saturated porous layer in vertical flows. They considered both isothermal and isoflux boundary conditions and used the Darcy-Brinkman-Forchheimer equation with the buoyancy term as well, algebraically solving for the steady-state velocity and temperature profiles in a semi-infinite domain over a range of viscosity ratio, conductivity ratio, Darcy number, Grashoff number, and width ratios, employing continuity and no-slip boundary conditions at the interface. Although they were the first to consider the two-domain system in mixed convection, the results are of limited value to the present study due to the exceedingly high Darcy number range considered, ranging from 0.125 to 0.5 in value.

Bhargav [47] studied forced convection in a porous layer with an overlying pure fluid layer. After thoroughly reviewing the relevant literature, the problem was analytically solved. He considered two-dimensional flow, carefully solving the governing equations for fully-developed conditions in an infinite channel. Entrance effects were also considered. Various boundary conditions were considered for the heater and top surfaces, but Ochoa-Tapia and Whitaker's stress jump condition was applied at the interface between the porous and fluid regions. Results from the Darcy equation were compared to those from the Darcy-Brinkman equation and to those from the Forchheimer equation, showing significant differences at some conditions. In addition, the effects of viscous dissipation were considered, including 5 various forms of the dissipation function. Within a certain range of Darcy number (0.1 to 0.001), it was shown that the peak Nusselt number occurs at a porous height ratio ranging from 0.6 to 0.8.

## 2.6 Natural Convection in Porous Media

No other authors to date have considered mixed convection with both a pure fluid and a saturated porous domain. Although the research in mixed convection is limited in this way, natural convection studies are more numerous and can provide valuable insight into the problem of the present study.

Elder [48] first studied natural convection from a localized heat source, numerically solving the problem with a finite difference method. The domain considered is similar to that for mixed convection studies, being much longer than tall, with an aspect ratio of 10. Streamlines and isotherms were presented for a range of heater sizes and Rayleigh numbers. With a dimensionless heater length, $\delta = 1$, the fluid plume was shown to rise in a single narrow column. With $\delta = 2$, two recirculating regions form, rotating in opposite directions. With $\delta = 3$, a pair of Rayleigh cells are formed, and at $\delta = 6$, there are three pairs of Rayleigh cells.

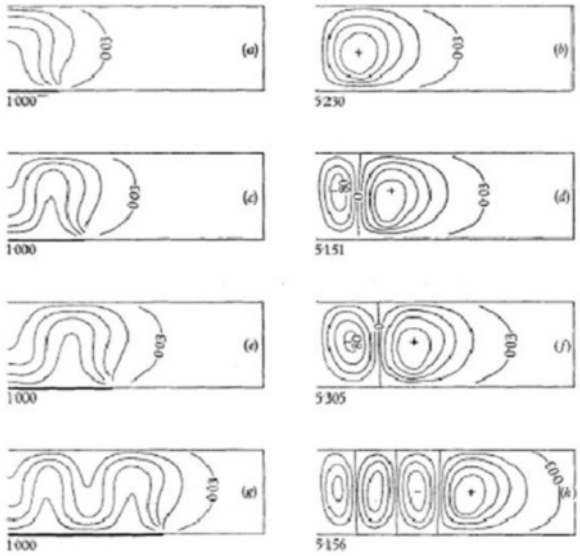

Figure 20. Effect of varying heater size on natural convection plume characteristic [48].

This same problem of localized heating was studied by Prasad and Kulacki [49] [50]. They solved the problem numerically, using finite difference equations, over a range of aspect ratios and dimensionless heater lengths. At a fixed heater size, it was shown that changing the aspect ratio has minimal effect on the overall heat transfer rate of the system. It was also shown that at small dimensionless heater lengths ($\delta > 2$) the recirculation due to natural convection was always unicellular, but beyond $\delta = 2$, the recirculation becomes multicellular.

Bagchi [1] thoroughly reviewed the limited literature regarding natural convection in a porous medium with an overlying fluid layer. The problem domain shown in Figure 21 was solved numerically using finite volume equations and was tested experimentally. The Darcy-Brinkman-Forchheimer equation, with the addition of the buoyancy term and the transient and convective terms, was used (Eqn. (6)). The problem formulation used the porosity as a switching parameter that causes Eqn. (6) to become the Navier-Stokes equation in the pure fluid layer when the porosity goes to unity. However, the derivatives of the porosity were not considered to account for the rapid change at the interface. Various heater size, height ratio (height of the porous layer to total height), Rayleigh number, Prandtl number, Darcy number, conductivity ratio, and aspect ratio were studied. The numerical results showed excellent agreement with the classical solutions to the Rayleigh-Benard problem (natural convection in a pure fluid layer) and to the Horton-

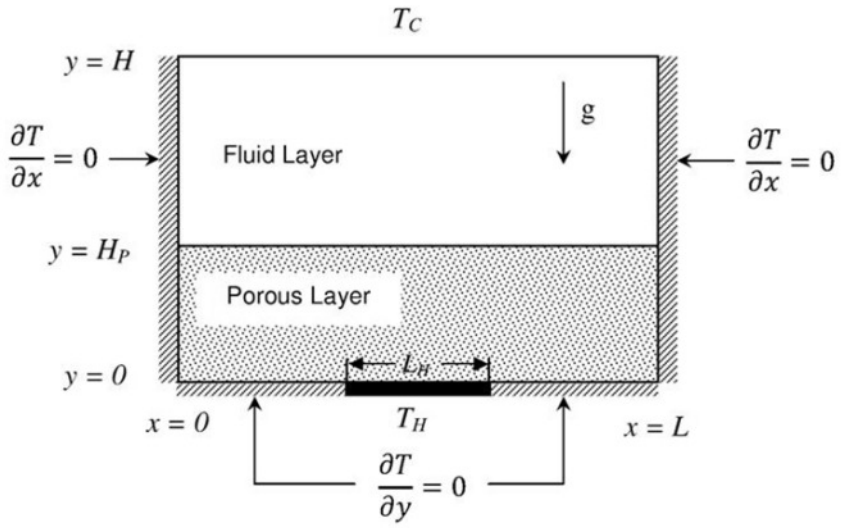


Figure 21. Problem domain for Bagchi natural convection study [1].

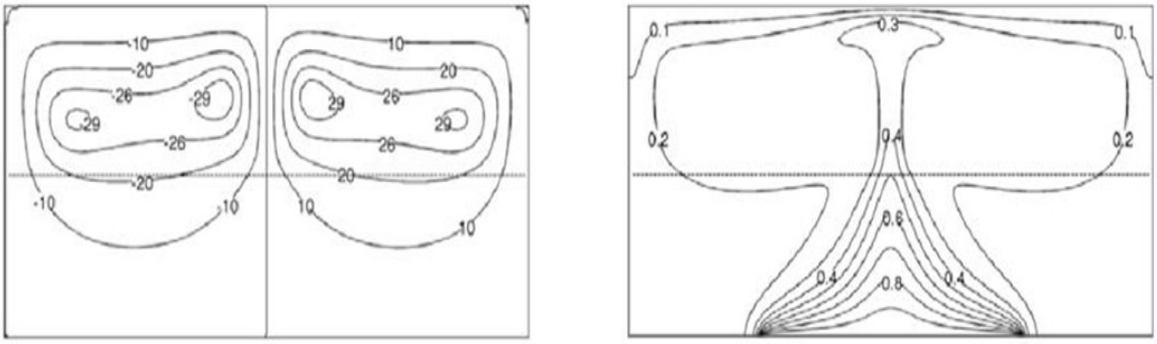


Figure 22. Streamlines and isotherms for fluid-superposed porous layers problem (RaDa = 1) [1].

Rogers-Lapwood problem (natural convection in a fluid-saturated porous medium). As the porous height ratio was reduced to less than one, the strength of the thermal plume greatly increased in the pure fluid region, and the recirculation was primarily contained in the pure fluid region as well.

It was shown that increasing the Darcy number increased the total heat transfer due to a decreased restriction to bulk fluid motion, that the Prandtl number had little effect on the overall heat transfer, and that the conductivity ratio between the solid and fluid phases had a large impact due to an increase in convective motion. Disagreement between numerical and experimental results (Figure 23) points towards some additional

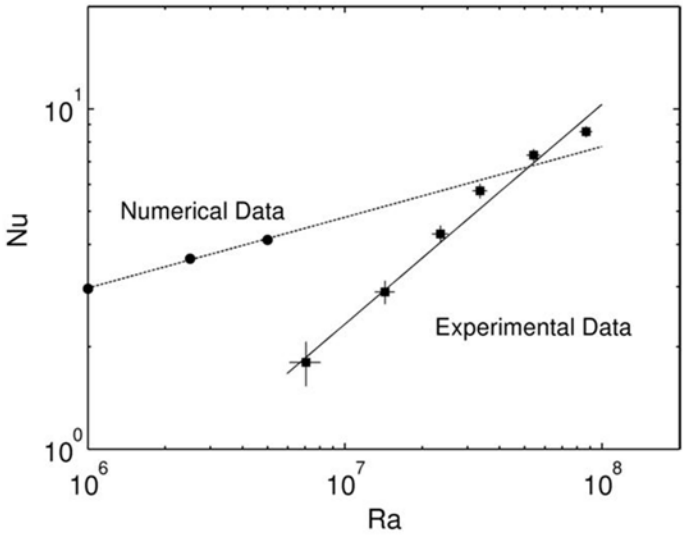


Figure 23. Comparison of numerical and experimental results from Bagchi natural convection study [1].

refinement of the numerical solution or potentially some unknown source of error in the experimental methods.

The results of Bagchi are further reviewed in the numerical results chapter as a base case for the numerical results of the present study.

## 2.7 Literature Review Conclusions

In conclusion, the development of the governing equations has been shown, the historical work considering the interfacial boundary conditions has been reviewed, the various approaches to the effective thermal conductivity have been explored, and the applicable research on natural/mixed convection in porous media has been reviewed.

The current state of research clearly favors the one-domain approach [1,28], using the porosity as a switching parameter, thus avoiding the need to explicitly define boundary conditions at the interface. Although this avoids the question of interfacial boundary conditions, it opens the question of porosity variation near the interface. However, there is no clear method used to properly transition from the porous layer to the pure fluid layer, and appropriate methods need to be determined. The present work further explores this in the following sections.

Determining the effective thermal conductivity of a porous medium has been a challenge, and there is an abundance of research on the subject. The effective thermal conductivity becomes somewhat of a catch-all to include various other effects as well, such as dispersion and tortuosity. The research for stagnant thermal conductivity provides many correlation equations that have a great deal of variation at high conductivity ratios but all converge at low conductivity ratios, and fortunately, the present study considers low conductivity ratios. The effects of dispersion, tortuosity, etc. can easily be included by using readily available correlation equations that correct for these effects.

Natural convection in porous media, particularly in a porous layer with an overlying fluid layer has been thoroughly addressed in the literature. Mixed convection, on the other hand, has not. There are many mixed convection studies that consider a full porous domain, but the literature is lacking for mixed convection in a porous layer with an overlying pure fluid layer.

## Chapter 3. Mathematical Formulation and Numerical Methods

The problem of mixed convection in horizontal fluid-superposed porous layers with localized heating from below is mathematically considered in the following chapter. First, the governing equations are presented, including the development and justification of the terms used, non-dimensionalization of the resulting equations, conversion to the stream function-vorticity form of the equations, and a presentation of the one-domain formulation with porosity variation at the interface. Second, the numerical methods are presented, including the discretization of the governing equations using control volumes, explanation and implementation of the boundary conditions, explanation of the implicit numerical scheme, convergence criteria, and grid independence.

The problem domain being solved in the present study is shown in Figure 24. The top surface is held at a constant temperature and has a no-slip velocity boundary condition applied. The bottom surface also has a no-slip velocity boundary condition, and has a constant temperature boundary condition along the heater surface and an insulated boundary condition along the rest of the bottom. The inlet and outlet have an insulated boundary condition and have one of two options for the velocity. For the natural convection case, no slip velocity boundary conditions are applied at the left and right boundaries, and for mixed convection a fixed velocity profile based on steady-state conditions is applied at the inlet and outlet. Further application of boundary conditions is discussed in later sections.

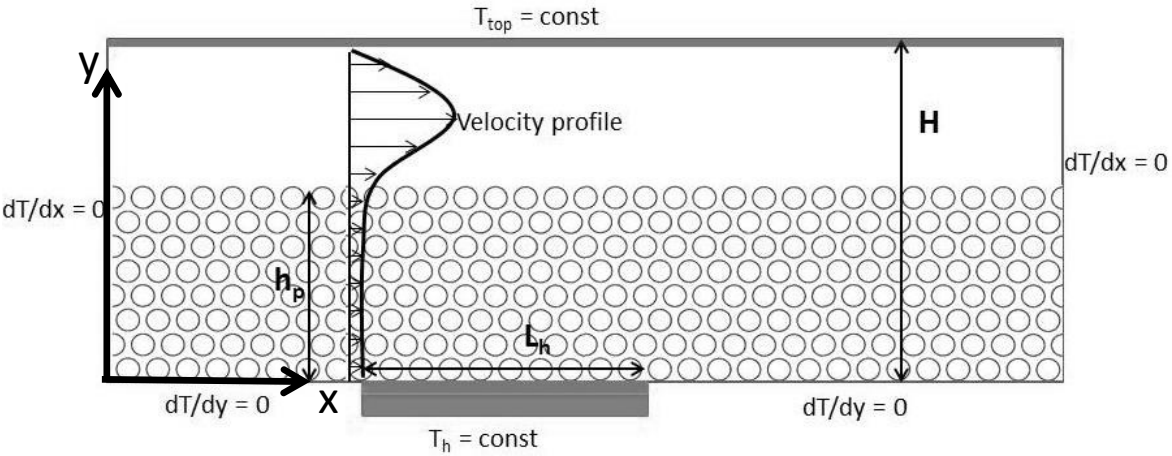


Figure 24. Problem domain for present study.

A Cartesian coordinate system is used, with the x direction being in the horizontal and the y-direction in the vertical. Gravity is in the negative y-direction, and with the bottom plate held at a higher temperature than the top plate, the effects of buoyancy drive the flow upward in the positive y-direction. Forced flow for the mixed convection case flows from left to right in the x-direction.

## 3.1 Governing equations

Two sets of equations are presented, one for the porous region and another for the fluid region. Equations governing the flow and the temperature are both presented for each region and then the equations are shown to reduce to a single set of equations as the porosity is transitions from $\phi = \phi_\infty$ to $\phi = 1$ as the domain shifts from the porous to the overlying fluid layer.

For incompressible flow, the governing equations for the porous layer include the continuity equation, the Darcy-Brinkman-Forchheimer equation (with the addition of the buoyancy term and the transient and convective terms), and the volume averaged energy equation. Although the steady-state solution is desired, the transient equations are required due to their coupled nature in natural/mixed convection problems.

### 3.1.1 Development of governing equations

The continuity equation for incompressible flow is,

$$\frac{\partial u}{\partial x} + \frac{\partial v}{\partial y} = 0. \tag{26}$$

The Darcy-Brinkman-Forchheimer equations, Eqns. (27)-(28), with the addition of the buoyancy term and the transient and convective terms included are given as follows for both the x and y directions. Although several of the terms have been debated, all terms are included for the sake of completeness and to allow for the one-domain formulation. Further explanation and discussion of the terms being used is provided in the literature review section of the present work. The Boussinesq approximation has been used.

$$\rho_f\left[\phi^{-1}\frac{\partial u}{\partial t}+\phi^{-2}\left(u\frac{\partial u}{\partial x}+v\frac{\partial u}{\partial y}\right)\right]=-\frac{\partial P}{\partial x}-\frac{\mu}{K}u+\tilde{\mu}\left(\frac{\partial^2 u}{\partial x^2}+\frac{\partial^2 u}{\partial y^2}\right)-\frac{c_F}{\sqrt{K}}\rho_f|\mathbf{V}|u, \tag{27}$$

$$\begin{aligned}\rho_f\left[\phi^{-1}\frac{\partial v}{\partial t}+\phi^{-2}\left(u\frac{\partial v}{\partial x}+v\frac{\partial v}{\partial y}\right)\right]&\\ =-\frac{\partial P}{\partial y}-\frac{\mu}{K}v+\tilde{\mu}\left(\frac{\partial^2 v}{\partial x^2}+\frac{\partial^2 v}{\partial y^2}\right)-\frac{c_F}{\sqrt{K}}\rho_f|\mathbf{V}|v&\\ -\rho_f g\big(1-\beta(T-T_0)\big).&\end{aligned} \tag{28}$$

Applying the conservation of energy principle yields the combined energy equation for the porous domain,

$$\sigma\frac{\partial T}{\partial t}+u\frac{\partial T}{\partial x}+v\frac{\partial T}{\partial y}=\frac{\partial}{\partial x}\left(\alpha_e\frac{\partial T}{\partial x}\right)+\frac{\partial}{\partial y}\left(\alpha_e\frac{\partial T}{\partial y}\right). \tag{29}$$

This equation assumes local thermodynamic equilibrium (the solid and fluid phases are always at the same temperature) and allows for property variation.

### 3.1.2 Non-dimensionalization of governing equations

The above equations are non-dimensionalized using the following relations:

$$\bar{x}={}^{x}\!/_{H}, \tag{30}$$

$$\bar{y}={}^{y}\!/_{H}, \tag{31}$$

$$\bar{u}={}^{u}\!/_{U_0}, \tag{32}$$

$$\bar{v}={}^{v}\!/_{U_0}, \tag{33}$$

$$Ra=\frac{g\beta H^3(T_h-T_0)}{\alpha_f\nu}, \tag{34}$$

$$Pe={}^{U_0H}\!/_{\alpha_f}, \tag{35}$$

$$\theta=\frac{T-T_0}{T_h-T_0}, \tag{36}$$

$$Pr={}^{\nu}\!/_{\alpha_f}, \tag{37}$$

$$\lambda={}^{\alpha_e}\!/_{\alpha_f}, \tag{38}$$

$$\tau={}^{t\alpha_f}\!/_{H^2}, \tag{39}$$

$$\overline{P} = \frac{PH^2}{\rho_0 \alpha_f^2}, \tag{40}$$

$$\hat{\mu} = \frac{\tilde{\mu}}{\mu}, \tag{41}$$

where $T_0$ is the inlet and the top surface temperature and $U_0$ is the average forced flow across the entire channel,

$$U_0 = \frac{\text{Volumetric flowrate}}{\text{Area}}. \tag{42}$$

To non-dimensionalize the flow equations, both sides are multiplied by $\frac{H^3}{\alpha_f^2 \rho_0}$ and the above substitutions are made. The resulting non-dimensional equations are,

$$\phi^{-1} Pe \frac{\partial \bar{u}}{\partial \tau} + \phi^{-2} Pe^2 \left( \bar{u} \frac{\partial \bar{u}}{\partial \bar{x}} + \bar{v} \frac{\partial \bar{u}}{\partial \bar{y}} \right) = -\frac{\partial \overline{P}}{\partial \bar{x}} - \frac{PrPe}{Da} \bar{u} + \hat{\mu} PrPe \left( \frac{\partial^2 \bar{u}}{\partial \bar{x}^2} + \frac{\partial^2 \bar{u}}{\partial \bar{y}^2} \right) - \frac{c_F Pe^2}{\sqrt{Da}} |\overline{\mathbf{V}}| \bar{u}, \tag{43}$$

$$\phi^{-1} Pe \frac{\partial \bar{v}}{\partial \tau} + \phi^{-2} Pe^2 \left( \bar{u} \frac{\partial \bar{v}}{\partial \bar{x}} + \bar{v} \frac{\partial \bar{v}}{\partial \bar{y}} \right) = -\frac{\partial \overline{P}}{\partial \bar{y}} - \frac{PrPe}{Da} \bar{v} + \hat{\mu} PrPe \left( \frac{\partial^2 \bar{v}}{\partial \bar{x}^2} + \frac{\partial^2 \bar{v}}{\partial \bar{y}^2} \right) - \frac{c_F Pe^2}{\sqrt{Da}} |\overline{\mathbf{V}}| \bar{v} + \frac{gH^3}{\alpha_f^2} + PrRa\theta. \tag{44}$$

The first term on the LHS is the transient term, the second and third terms on the LHS are the convective terms. The RHS contains four or five terms, the first being the pressure gradient, which is the driving force for any forced flow, such as in mixed or forced convection. The second term is the Darcy term and is generally the dominant term in most natural convection or mixed convection applications due to the typical low values of the Darcy number. The third term is the Brinkman term and captures the viscous effects due to boundaries within the porous domain (solid or free). The fourth term is the Forchheimer term and can become the dominant term at large flow velocities, and the transition from the Darcy regime to the Forchheimer regime will vary depending on the

Darcy number and the flow velocity. The sixth term in Eqn. (44) captures the effects of buoyancy, causing flow to accelerate upward when the temperature is elevated above that of the free-stream.

To non-dimensionalize the energy equation, both sides are multiplied by $^{H^2}/_{\alpha_f}$ and the above substitutions are made. The resulting non-dimensional energy equation is,

$$\sigma\frac{\partial\theta}{\partial\tau}+\mathrm{Pe}\bar{u}\frac{\partial\theta}{\partial\bar{x}}+\mathrm{Pe}\bar{v}\frac{\partial\theta}{\partial\bar{y}}=\frac{\partial}{\partial\bar{x}}\left(\lambda\frac{\partial\theta}{\partial\bar{x}}\right)+\frac{\partial}{\partial\bar{y}}\left(\lambda\frac{\partial\theta}{\partial\bar{y}}\right). \tag{45}$$

This equation neglects viscous dissipation and does not include any energy generation. The first term on the LHS is the transient term, the second and third terms on the LHS are the convective terms, and the RHS contains the conduction terms.

3.1.3 Stream function-vorticity form of governing equations

It is often convenient in two-dimensional problems to use the stream function-vorticity form of the governing equations. The main advantage of this method is that it eliminates the pressure term from the resulting equations. The stream function and vorticity are,

$$\bar{u}=-\frac{\partial\Psi}{\partial\bar{y}}, \tag{46}$$

$$\bar{v}=\frac{\partial\Psi}{\partial\bar{x}}, \tag{47}$$

$$\omega=\frac{\partial\bar{v}}{\partial\bar{x}}-\frac{\partial\bar{u}}{\partial\bar{y}}. \tag{48}$$

Combining the preceding equations results in the well-known stream-vorticity equation,

$$\omega=\frac{\partial^2\Psi}{\partial\bar{x}^2}+\frac{\partial^2\Psi}{\partial\bar{y}^2}. \tag{49}$$

To start, the partial derivative of Eqn. (43) with respect to y is taken, resulting in Eqn. (52). This is a key step in deriving the variable porosity form of the equations. The

Darcy number is a function of the porosity (Eqn. (50) [1]) and is therefore allowed to vary in the y-direction. This generates additional terms in the resulting stream-vorticity form of the flow equation,

$$\mathrm{Da} = \frac{\left(\frac{\mathrm{d_p}}{\mathrm{H}}\right)^2 \phi^3}{180(1-\phi)^2}. \tag{50}$$

Although the Forchheimer constant is written as a function of porosity by some authors [1], the more widely accepted form is not a function of porosity, but rather the bead diameter and the hydraulic diameter of the channel [2],

$$\mathrm{c_f} = 0.55\left(1 - 5.5\frac{\mathrm{d_p}}{\mathrm{D_H}}\right). \tag{51}$$

Partial derivatives are now denoted as subscripts, for example, $\frac{\partial \bar{\mathrm{u}}}{\partial \bar{\mathrm{x}}}$ is now written as $\bar{\mathrm{u}}_\mathrm{x}$,

$$\begin{aligned}\phi^{-1}\mathrm{Pe}\frac{\partial \bar{\mathrm{u}}_\mathrm{y}}{\partial \tau} + \phi^{-2}\mathrm{Pe}^2\left(\bar{\mathrm{u}}\bar{\mathrm{u}}_{\mathrm{xy}} + \bar{\mathrm{u}}_\mathrm{y}\bar{\mathrm{u}}_\mathrm{x} + \bar{\mathrm{v}}\bar{\mathrm{u}}_{\mathrm{yy}} + \bar{\mathrm{v}}_\mathrm{y}\bar{\mathrm{u}}_\mathrm{y}\right) \\ = -\bar{\mathrm{P}}_{\mathrm{xy}} - \mathrm{PrPe}\frac{\mathrm{Da}\bar{\mathrm{u}}_\mathrm{y} - \bar{\mathrm{u}}\mathrm{Da}_\mathrm{y}}{\mathrm{Da}^2} + \hat{\mu}\mathrm{PrPe}\left(\bar{\mathrm{u}}_{\mathrm{xxy}} + \bar{\mathrm{u}}_{\mathrm{yyy}}\right) \\ - \mathrm{c_F}\mathrm{Pe}^2\frac{\sqrt{\mathrm{Da}}\left(|\bar{\mathbf{V}}|\bar{\mathrm{u}}_\mathrm{y} + |\bar{\mathbf{V}}|_\mathrm{y}\bar{\mathrm{u}}\right) - |\bar{\mathbf{V}}|\bar{\mathrm{u}}\frac{1}{2}\mathrm{Da}^{-\frac{1}{2}}\mathrm{Da}_\mathrm{y}}{\mathrm{Da}}.\end{aligned} \tag{52}$$

Next, the partial derivative of Eqn. (44) with respect to x is taken,

$$\begin{aligned}\phi^{-1}\mathrm{Pe}\frac{\partial \bar{\mathrm{v}}_\mathrm{x}}{\partial \tau} + \phi^{-2}\mathrm{Pe}^2\left(\bar{\mathrm{u}}\bar{\mathrm{v}}_{\mathrm{xx}} + \bar{\mathrm{u}}_\mathrm{x}\bar{\mathrm{v}}_\mathrm{x} + \bar{\mathrm{v}}\bar{\mathrm{v}}_{\mathrm{xy}} + \bar{\mathrm{v}}_\mathrm{x}\bar{\mathrm{v}}_\mathrm{y}\right) \\ = -\bar{\mathrm{P}}_{\mathrm{xy}} - \frac{\mathrm{PrPe}}{\mathrm{Da}}\bar{\mathrm{v}}_\mathrm{x} + \hat{\mu}\mathrm{PrPe}\left(\bar{\mathrm{v}}_{\mathrm{xxx}} + \bar{\mathrm{v}}_{\mathrm{xyy}}\right) \\ - \frac{\mathrm{c_F}\mathrm{Pe}^2}{\sqrt{\mathrm{Da}}}\left(|\bar{\mathbf{V}}|\bar{\mathrm{v}}_\mathrm{x} + |\bar{\mathbf{V}}|_\mathrm{x}\bar{\mathrm{v}}\right) + \mathrm{PrRa}\theta_\mathrm{x}.\end{aligned} \tag{53}$$

Subtracting Eqn. (52) from Eqn. (53) and substituting the vorticity, Eqn. (48), results in the following form of the governing equation in the porous layer,

$$\phi^{-1}\mathrm{Pe}\frac{\partial\omega}{\partial\tau}+\phi^{-2}\mathrm{Pe}^2\left[(\bar{u}\omega)_x+(\bar{v}\omega)_y\right]$$
$$=\hat{\mu}\mathrm{PrPe}\left(\omega_{xx}+\omega_{yy}\right)+\left(-\frac{\mathrm{PrPe}}{\mathrm{Da}}-\frac{c_F\mathrm{Pe}^2}{\sqrt{\mathrm{Da}}}|\bar{\mathbf{V}}|\right)\omega$$
$$+\left(\mathrm{PrRa}\theta_x+c_F\mathrm{Pe}^2\frac{|\bar{\mathbf{V}}|_y\bar{u}-|\bar{\mathbf{V}}|_x\bar{v}}{\sqrt{\mathrm{Da}}}\right) \tag{54}$$
$$+\left(-\bar{u}\frac{\mathrm{Da}_y}{\mathrm{Da}^2}\left(\mathrm{PrPe}+\frac{c_F\mathrm{Pe}^2\sqrt{\mathrm{Da}}|\bar{\mathbf{V}}|}{2}\right)\right).$$

Eqns. (45) and (54) govern the temperature and flow in the porous layer.

The Navier-Stokes equations govern the flow in the fluid layer. The dimensionless stream-vorticity version of the Navier-Stokes equations and the energy equation follows:

$$\mathrm{Pe}\frac{\partial\omega}{\partial\tau}+\mathrm{Pe}^2\left[(\bar{u}\omega)_x+(\bar{v}\omega)_y\right]=\mathrm{PrPe}\left(\omega_{xx}+\omega_{yy}\right)+\mathrm{PrRa}\theta_x \tag{55}$$

$$\sigma\frac{\partial\theta}{\partial\tau}+\mathrm{Pe}\bar{u}\frac{\partial\theta}{\partial\bar{x}}+\mathrm{Pe}\bar{v}\frac{\partial\theta}{\partial\bar{y}}=\frac{\partial}{\partial\bar{x}}\left(\frac{\partial\theta}{\partial\bar{x}}\right)+\frac{\partial}{\partial\bar{y}}\left(\frac{\partial\theta}{\partial\bar{y}}\right). \tag{56}$$

However, in the next section it is shown that separate equations for the two layers are not necessary, provided that the porosity goes to unity in the fluid layer.

### 3.1.4 One-domain formulation

To allow for a straightforward implementation of well-established numerical schemes, a single set of governing equations is preferred. If the porosity is allowed to vary, ranging from $\phi=\phi_\infty$ to $\phi=1$, where $\phi=1$ in the fluid region, then $\mathrm{Da}\to\infty$, $\lambda\to1$, $\hat{\mu}\to1$, and $\mathrm{Da}_y\to0$. Using these values, it can clearly be seen that the governing equations in the porous region reduce to the governing equations in the fluid region. This is a simple concept, but the sophistication of the method lies in the variation of the porosity and the additional terms in the governing equations that result.

Several authors assume a porosity variation of the following form [2,51],

$$\phi = \phi_\infty \left[1 + C\exp\left(-A\frac{y}{d_p}\right)\right], \tag{57}$$

where C = 1.4, A ranges from 5 to 6 for a porosity of approximately $\phi_\infty = 0.40$, and y is the distance from the boundary. This equation can be used to allow for the channeling effect near a solid boundary or as is done in the present case, to allow for porosity variation at the interface between the porous and fluid layers. In the present study, C = 1.4 and A = 5 have been used.

To summarize, the porous region is governed by the Darcy-Brinkman-Forchheimer equation with the addition of the buoyancy term and the transient and convective terms, while the fluid region is governed by the Navier-Stokes equations. However, the single set of equations developed is suitable for both regions, provided that the porosity is varied, resulting in a single problem domain. This set of governing equations for the combined porous and fluid regions was developed in the stream function-vorticity format and non-dimensionalized. The resulting equation contains additional terms, where the effects of the porosity variation are realized in the Darcy number variation for the flow equation and the conductivity variation for the energy equation. Specifics regarding implementation are found in the numerical methods section.

## 3.2 Numerical Methods

Suitable methods must be used in obtaining a numerical solution for any problem of study. There are a wide range of options, including (but not limited to) finite volume equations verses finite difference equations, implicit verses explicit methods, central differencing verses upwind differencing, constant grid verses variable grid, first order verses second order, and a variety of boundary conditions as well. The goal is to solve the governing equations to an acceptable degree of accuracy over a range of dimensionless parameters. The grid must be fine enough to obtain a grid-independent solution, but not so fine as to make the computation time unacceptably high.

In the present study, finite volume methods were chosen over finite difference methods. Although both methods are widely used and for many problems selection

comes down to personal preference, in the present study, finite volume methods provide better conservation of energy and mass across the entire grid. In many of the derivative terms, central differencing was employed, however, for the convective terms, upwind differencing was employed. Although quadratic upwind differencing was used by a recent author [1], standard upwind differencing proved less problematic in the current study due to inherent instabilities in regions of sharp gradients. A variable grid was chosen over a constant grid. This allowed for a coarser overall grid with a focus of points in the desired regions, thus achieving a grid-independent solution with fewer total grid points [52]. Second order differencing equations were used for most equations with the exception of a few boundary conditions where the grid points were clustered very close, thus, achieving second order accuracy with first order equations.

### 3.2.1 Variable grid control volume method

The variable grid used in the present study uses non-overlapping control volumes, where point P corresponds to the current control volume, N corresponds to the control volume above the current volume in the y-direction, S corresponds to the control volume below (in the negative y-direction), E corresponds to the volume to the right (positive x-direction), and W corresponds to the volume to the left (negative x-direction). The points do not necessarily fall in the center of the control volume, but the control volume faces do fall in the center of the distance between corresponding grid points (Figure 25). The control volume faces (not the grid points) were chosen to align with the boundaries of the problem domain, therefore, additional grid points were defined for the boundary values (Figure 26). The matrix indices are defined as [i,j], with i corresponding to the x-direction, starting with $i = 1$ at the inlet and $i = N_x$ at the outlet, and j corresponding to the y-direction, starting with $j = 1$ at the lower surface and $j = N_y$ at the upper surface.

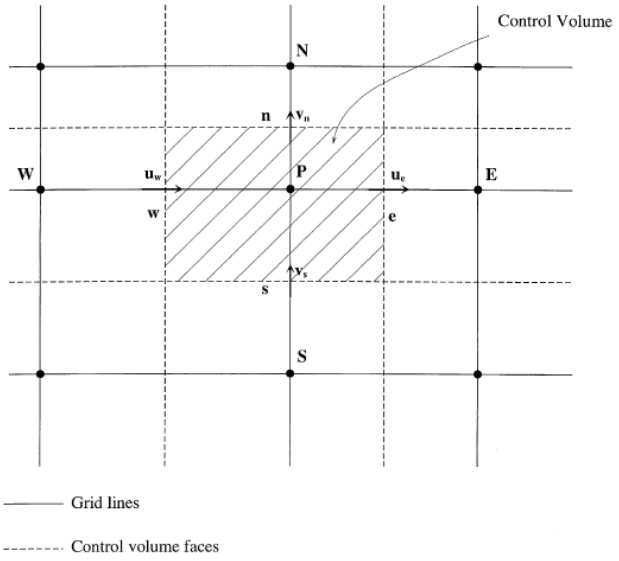


Figure 25. Variable grid control volume schematic [53].

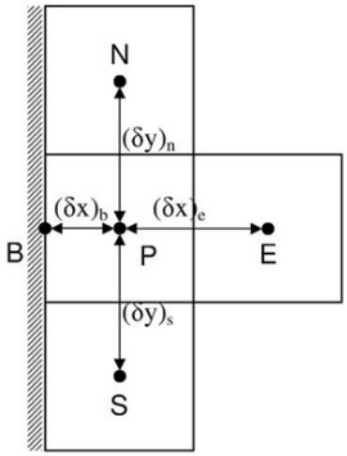


Figure 26. Example of boundary grid point at edge of control volume [1].

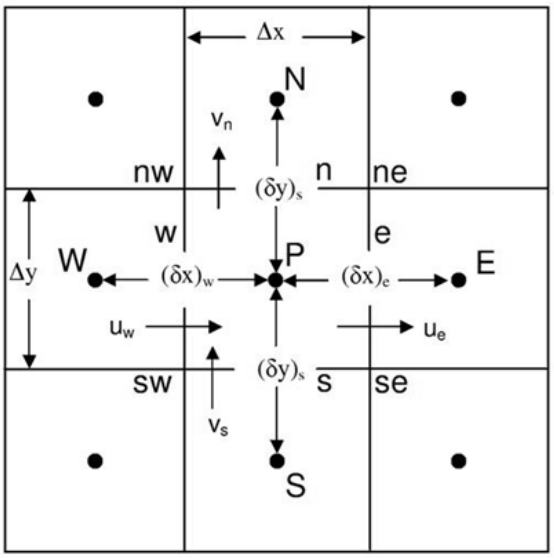


Figure 27. Grid spacing [1].

It can clearly be seen that the distance between P and E is not necessarily equal to the distance between points P and W, therefore separate $\delta x_e$, $\delta x_w$, $\delta y_n$, and $\delta y_s$ values are defined for each grid point, as well as $\Delta x$ and $\Delta y$, which define the width and height of each control volume (Figure 27).

For the present case, it is desired that grid points to be focused near the solid boundaries and near the interface between the fluid and porous layers. Also, sharp gradients are found near the edges of the heater, so grid points were focused in the x-direction in the vicinity of the heater. Several examples are shown in Figure 28 - Figure 30 where it can clearly be seen that the grid points are focused around the interface between the porous and fluid layers and around the heater edges. As previously stated, this allows for a grid-independent solution to be achieved with significantly fewer grid points.

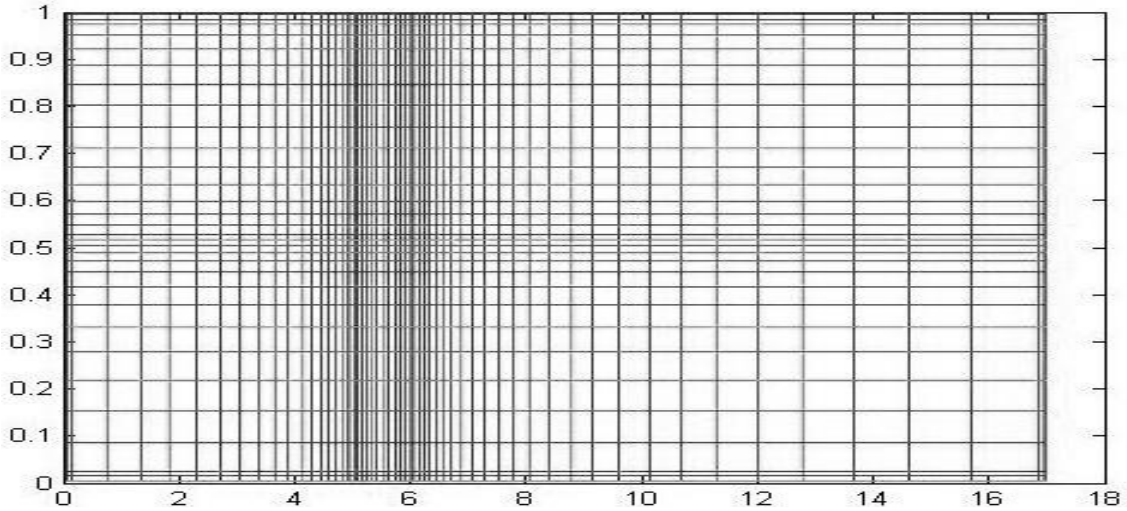

Figure 28. Grid lines for $\eta = 0.5$, $\delta = 1$.

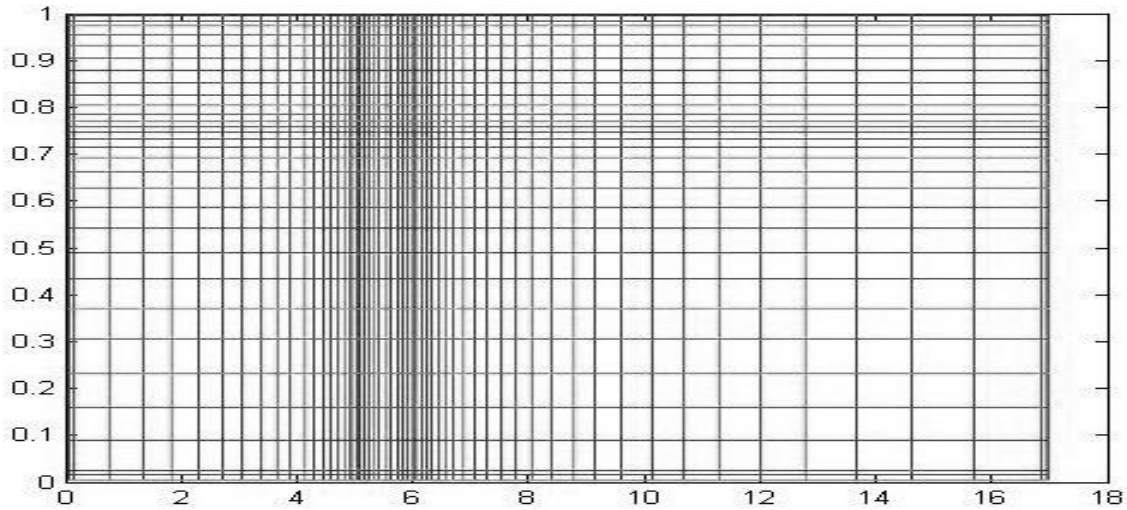

Figure 29. Grid lines for $\eta = 0.75$, $\delta = 1$.

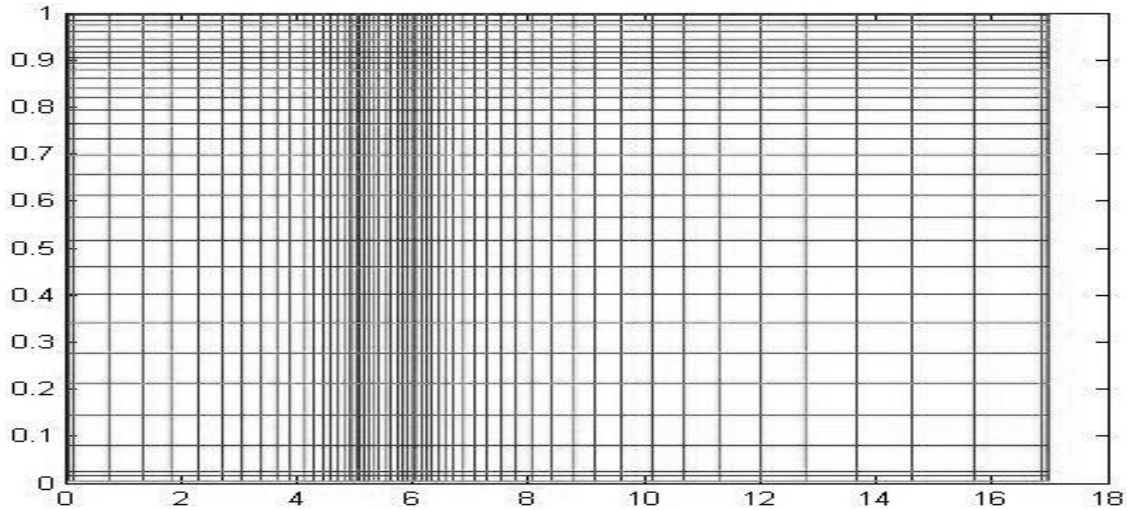

Figure 30. Grid lines for $\eta = 0.9$, $\delta = 1$.

### 3.2.2 Discretization of the stream-vorticity equation

First, the stream-vorticity equation is considered. Using well-established control volume techniques, Eqn. (49) is integrated across a control volume from the south to the north face in the y-direction and from the west to the east face in the x-direction. The remaining derivative terms are discretized using a central difference at the control volume face, incorporating the surrounding points with the current grid point. For example, the derivative of the stream function at the east face of the control volume is given by,

$$\left(\frac{\partial \Psi}{\partial x}\right)_{\text{east face}} = \frac{\Psi_E - \Psi_P}{\delta x_e}. \tag{58}$$

Many steps are omitted from the present work and a step by step process can be found in the recent work of Bagchi [1]. The resulting discretized equation is given below, where all quantities are dimensionless and the over-bars have been dropped for convenience. The constants in the above equation are,

$$\Psi_P = C_E\Psi_E + C_W\Psi_W + C_N\Psi_N + C_S\Psi_S + C_P\omega_P, \tag{59}$$

$$C = \frac{1}{\Delta x \delta x_e} + \frac{1}{\Delta x \delta x_w} + \frac{1}{\Delta y \delta y_n} + \frac{1}{\Delta y \delta y_s}, \tag{60}$$

$$C_E = \frac{1}{C\Delta x \delta x_e}, \tag{61}$$

$$C_W = \frac{1}{C\Delta x \delta x_w}, \tag{62}$$

$$C_N = \frac{1}{C\Delta y \delta y_n}, \tag{63}$$

$$C_S = \frac{1}{C\Delta y \delta y_s}, \tag{64}$$

$$C_P = \frac{-1}{C}. \tag{65}$$

Due to the variable grid, $\Delta x, \Delta y, \delta x_e, \delta x_w, \delta y_n,$ and $\delta y_s$ are uniquely defined at each grid point, so the above constants are also defined at each grid point. The vorticity of the previous iteration is used at each grid point for the value of $\omega_P$.

The discretized form of the stream function can be written at each grid point, resulting in $N_x \times N_y$ simultaneous linear equations. This set of linear equations, when solved, provides the stream function value at every grid point in the computational domain. However, special care must be taken at the grid points corresponding to the outer layer of control volumes. These points must take the boundary conditions into account. Details on implementing the boundary conditions are found in Section 3.2.5 Initial/Boundary conditions of the present work.

Although the governing equations for the current problem are written in the stream function-vorticity form, velocity values are still required. Once the stream function values have been determined, it then becomes possible to calculate the velocity. Values are calculated at each control volume face, thus defining the convection into/out of the control volume across that face. Defining the velocity at each control volume face also allows for the flow into one volume to be exactly equal to the flow out of another control volume, since the eastern face velocity of one control volume is equal to the western face velocity of an adjacent control volume. This ensures conservation of mass within the entire computational domain. However, to calculate the face velocities, stream function values at the corners of the control volumes must be determined. In a fixed grid, simple averages of the surrounding four control volumes can be used, but with a variable grid, weighted averages must be used. Equations for calculating the stream function values in the control volume corners are,

$$\Psi_{ne} = \frac{1}{\Delta x_P + \Delta x_E}\left[\Delta x_E\left(\frac{\Psi_N \Delta y_P + \Psi_P \Delta y_N}{\Delta y_P + \Delta y_N}\right) + \Delta x_P\left(\frac{\Psi_{NE} \Delta y_P + \Psi_E \Delta y_N}{\Delta y_P + \Delta y_N}\right)\right], \tag{66}$$

$$\Psi_{nw} = \frac{1}{\Delta x_P + \Delta x_W}\left[\Delta x_W\left(\frac{\Psi_N \Delta y_P + \Psi_P \Delta y_N}{\Delta y_P + \Delta y_N}\right) + \Delta x_P\left(\frac{\Psi_{NW} \Delta y_P + \Psi_W \Delta y_N}{\Delta y_P + \Delta y_N}\right)\right], \tag{67}$$

$$\Psi_{se} = \frac{1}{\Delta x_P + \Delta x_E}\left[\Delta x_E\left(\frac{\Psi_S \Delta y_P + \Psi_P \Delta y_S}{\Delta y_P + \Delta y_S}\right) + \Delta x_P\left(\frac{\Psi_{SE} \Delta y_P + \Psi_E \Delta y_S}{\Delta y_P + \Delta y_S}\right)\right], \tag{68}$$

$$\Psi_{sw} = \frac{1}{\Delta x_P + \Delta x_W}\left[\Delta x_W\left(\frac{\Psi_S \Delta y_P + \Psi_P \Delta y_S}{\Delta y_P + \Delta y_S}\right) + \Delta x_P\left(\frac{\Psi_{SW} \Delta y_P + \Psi_W \Delta y_S}{\Delta y_P + \Delta y_S}\right)\right]. \tag{69}$$

With the stream function values at the control volume faces defined, the control volume velocities can then be determined by integrating Eqns. (46) and (47) across the corresponding control volume face, resulting in,

$$u_e = -\frac{\Psi_{ne} - \Psi_{se}}{\Delta y_P}, \tag{70}$$

$$u_w = -\frac{\Psi_{nw} - \Psi_{sw}}{\Delta y_P}, \tag{71}$$

$$v_n = \frac{\Psi_{ne} - \Psi_{nw}}{\Delta x_P}, \tag{72}$$

$$v_s = \frac{\Psi_{se} - \Psi_{sw}}{\Delta x_P}. \tag{73}$$

In addition, some terms require the velocity in the control volume itself. For these values, an appropriate average is taken,

$$u_P = \frac{u_e + u_w}{2}, \tag{74}$$

$$v_P = \frac{v_n + v_s}{2}, \tag{75}$$

where a velocity magnitude is required, the following definition is used,

$$|\mathbf{V}|_P = \sqrt{u_P^2 + v_P^2}. \tag{76}$$

To review, the discretized stream-vorticity equation has been determined. This equation is written at each grid point, resulting in a set of linear equations that must be solved. Once solved, the resulting stream function values at each point are used to determine the stream function values in the corners of the control volume. With the corner values, the control volume face velocities are determined and average control volume velocities are also determined. These values are used in the vorticity transport and energy equations.

### 3.2.3 Discretization of the vorticity transport equation

Next, the vorticity transport equation will be discretized. Similar to the process for the stream-vorticity equation, the resulting discretized form of the vorticity transport

equation can be written at each grid point, resulting in a set of linear equations that can then be solved. Although the solution method for the vorticity transport is different than that of the stream function-vorticity equation, the discretization process is similar. The vorticity transport equation, Eqn. (54), can be rearranged and put into the standard form of the advection-diffusion equation,

$$\frac{\partial \Sigma}{\partial t} + (\mathbf{u} \cdot \nabla)\Sigma = \gamma \nabla^2 \Sigma + S, \tag{77}$$

where $\Sigma$ represents the transport term (vorticity or temperature), $\gamma$ represents the diffusion coefficient, and S represents the source term. In the present case of the vorticity transport, the source term includes the Darcy term, the Forchheimer term, the buoyancy term, and the variable porosity term. The vorticity transport equation then becomes the following, with the over-bars omitted,

$$\frac{\phi}{Pe}\frac{\partial \omega}{\partial \tau} + (\mathbf{u} \cdot \nabla)\omega = \gamma \nabla^2 \omega + S, \tag{78}$$

where the source term, S, is broken up into two parts, where $S = S_P \omega_P + S_C$ and the following definitions are made,

$$\gamma = \frac{\hat{\mu}\phi^2}{Re}, \tag{79}$$

$$S_P = \phi^2 \left( -\frac{1}{ReDa} - \frac{c_F}{\sqrt{Da}} |\mathbf{V}| \right), \tag{80}$$

$$S_C = \phi^2 \left( Ri\theta_x + c_F \frac{|\mathbf{V}|_x v - |\mathbf{V}|_y u}{\sqrt{Da}} \right) + \phi^2 \left( -u \frac{Da_y}{Da^2} \left( \frac{1}{Re} + \frac{c_F \sqrt{Da} |\mathbf{V}|}{2} \right) \right), \tag{81}$$

where two new dimensionless numbers have been introduced, the Reynolds number and the Richardson number,

$$Re = \frac{Pe}{Pr} = \frac{U_0 H}{\upsilon}, \tag{82}$$

$$\mathrm{Ri} = \frac{\mathrm{RaPr}}{\mathrm{Pe}^2}. \tag{83}$$

Similar to the stream function-vorticity equation, the advection-diffusion equation is integrated in the x and y-directions, but is also integrated with respect to time. Implicit methods are used, but are not explained until later in this chapter. Intermediate steps have been omitted, and the final discretized form of the equation is,

$$\omega_P A_P + \omega_E A_E + \omega_W A_W + \omega_N A_N + \omega_S A_S = A_0. \tag{84}$$

The coefficients of the above equation are defined for each grid point, resulting in the following equations:

$$A_P = \frac{\phi_P}{\mathrm{Pe}\Delta\tau} + \frac{\Gamma_e u_e}{\Delta x} - \frac{\Gamma_w u_w}{\Delta x} + \frac{\Gamma_n v_n}{\Delta y} - \frac{\Gamma_s v_s}{\Delta y} - \phi_P^2\left(-\frac{1}{\mathrm{ReDa_P}} - \frac{c_F}{\sqrt{\mathrm{Da_P}}}|\mathbf{V}|_P\right) + \frac{\gamma_e}{\Delta x\delta x_e} + \frac{\gamma_w}{\Delta x\delta x_w} + \frac{\gamma_n}{\Delta y\delta y_n} + \frac{\gamma_s}{\Delta y\delta y_s}, \tag{85}$$

$$A_E = (1-\Gamma_e)\frac{u_e}{\Delta x} - \frac{\gamma_e}{\Delta x\delta x_e}, \tag{86}$$

$$A_W = -(1-\Gamma_w)\frac{u_w}{\Delta x} - \frac{\gamma_w}{\Delta x\delta x_w}, \tag{87}$$

$$A_N = (1-\Gamma_n)\frac{v_n}{\Delta y} - \frac{\gamma_n}{\Delta y\delta y_n}, \tag{88}$$

$$A_S = -(1-\Gamma_s)\frac{v_s}{\Delta y} - \frac{\gamma_s}{\Delta y\delta y_s}, \tag{89}$$

$$A_0 = \frac{\phi_P}{\mathrm{Pe}\Delta\tau}\omega_P^0 + \phi_P^2\left(\mathrm{Ri}\frac{\theta_E - \theta_W}{2\Delta x_P} + \frac{c_F}{\sqrt{\mathrm{Da_P}}}\left(v_P\frac{|\mathbf{V}|_E - |\mathbf{V}|_W}{2\Delta x_P} - u_P\frac{|\mathbf{V}|_N - |\mathbf{V}|_S}{2\Delta y_P}\right) - u_P\frac{\mathrm{Da_P} - \mathrm{Da_S}}{\mathrm{Da_P^2}\delta y_s}\left(\frac{1}{\mathrm{Re}} + \frac{c_F\sqrt{\mathrm{Da_P}}|\mathbf{V}|_P}{2}\right)\right). \tag{90}$$

Central differencing has been used for most derivatives, and property variation is accounted for by defining the $\gamma$ terms at the control volume faces using suitable averages. For example,

$$\gamma_e = \frac{1}{\mathrm{Re}}\left(\frac{(\hat{\mu}\phi^2)_P + (\hat{\mu}\phi^2)_E}{2}\right), \tag{91}$$

for the eastern control volume face.

As previously stated, upwind differencing was used for the convective terms instead of central differencing. Upwind differencing uses the direction of the velocity to determine which term is used in the differencing equation. For example, if $u_e > 0$ then the vorticity transport at the east face of the control volume is out of the control volume at a rate of $u_e\omega_P$ because it is flowing out of the P control volume, but if $u_e < 0$ then the vorticity transport at the east face of the control volume is into the control volume at a rate of $u_e\omega_E$ because it is flowing in from the east control volume. To account for this, the Γ coefficients were used in the above equations, where,

$$\text{if } u_e > 0, \text{ then } \Gamma_e = 1, \tag{92}$$

$$\text{if } u_w > 0, \text{ then } \Gamma_w = 0, \tag{93}$$

$$\text{if } v_n > 0, \text{ then } \Gamma_n = 1, \tag{94}$$

$$\text{if } v_s > 0, \text{ then } \Gamma_s = 0. \tag{95}$$

The Γ terms act as a switching parameter, putting the convective terms with the correct corresponding vorticity in Eqn. (84).

### 3.2.4 Discretization of the energy equation

Finally, the energy equation, Eqn. (45), is discretized. The procedure is similar to that of the vorticity transport equation, but much simpler. Once again, the control volume is integrated in the x and y-directions and with respect to time. Many intermediate steps were omitted for conciseness and further explanation can be found in [1]. The energy equation is also of the form of the advection-diffusion equation as previously discussed. In the case of the energy equation, the source term is zero, the Σ terms are now θ, and the γ terms are defined as the conductivity ratio, λ. The resulting discretized form of the energy equation is,

$$\theta_P B_P + \theta_E B_E + \theta_W B_W + \theta_N B_N + \theta_S B_S = B_0, \tag{96}$$

where the coefficients are,

$$B_P = \frac{\sigma}{\Delta\tau} + Pe\left(\frac{\Gamma_e u_e}{\Delta x} - \frac{\Gamma_w u_w}{\Delta x} + \frac{\Gamma_n v_n}{\Delta y} - \frac{\Gamma_s v_s}{\Delta y}\right) + \frac{\lambda_e}{\Delta x \delta x_e} + \frac{\lambda_w}{\Delta x \delta x_w} + \frac{\lambda_n}{\Delta y \delta y_n} + \frac{\lambda_s}{\Delta y \delta y_s}, \tag{97}$$

$$B_E = (1-\Gamma_e)Pe\frac{u_e}{\Delta x} - \frac{\lambda_e}{\Delta x \delta x_e}, \tag{98}$$

$$B_W = -(1-\Gamma_w)Pe\frac{u_w}{\Delta x} - \frac{\lambda_w}{\Delta x \delta x_w}, \tag{99}$$

$$B_N = (1-\Gamma_n)Pe\frac{v_n}{\Delta y} - \frac{\lambda_n}{\Delta y \delta y_n}, \tag{100}$$

$$B_S = -(1-\Gamma_s)Pe\frac{v_s}{\Delta y} - \frac{\lambda_s}{\Delta y \delta y_s}, \tag{101}$$

$$B_0 = \frac{\sigma}{\Delta\tau}\theta_P^0. \tag{102}$$

Property variation is accounted for by defining the $\lambda$ values at the control volume faces using appropriate averages. For example,

$$\lambda_e = \frac{\lambda_P + \lambda_E}{2}. \tag{103}$$

In the present work, the conductivity ratio is a function of porosity and of the local Peclet number, so therefore it can vary in both the x and y-directions even though the porosity only varies in the y-direction.

To review, the vorticity and energy transport equations have been discretized and put into a standard form. The coefficients for each discretized equation have been defined and explained. The solution algorithm updates the coefficients for each iteration because they depend on many changing parameters, such as velocity and temperature. The discretized equations are written for each grid point, resulting in $N_x \times N_y$ simultaneous linear equations that, when solved, provide the vorticity and temperature at

each grid point. Further details of the solution algorithm are provided later in this chapter.

### 3.2.5 Initial/Boundary conditions

To solve a set of differential equations that vary in time and space, boundary conditions and initial conditions are both required. For the present study, no-slip velocity boundary conditions are applied at all solid surfaces, constant temperature boundary conditions are applied at the heater surface and at the upper surface, and adiabatic boundary conditions are applied at all other surfaces.

Two cases were considered for the present study. Initially, the problem of natural convection was solved in order to validate the code against prior work and classical solutions. Once the code was shown to be working, the problem of mixed convection was solved. In the case of natural convection, the left and right boundaries were also treated as adiabatic and a no-slip velocity was applied. In the case of mixed convection, a fixed velocity profile was enforced at the inlet and outlet corresponding to the fully-developed velocity profile for the given conditions, and adiabatic conditions were also applied. However, no-slip velocity conditions are easy to implement for velocity, but are not quite as straightforward for stream function and vorticity values.

In the present case, all values have been non-dimensionalized. The over-bars have been omitted for convenience. Temperature is non-dimensionalized, with the boundary conditions given in Table 1.

Table 1. Temperature boundary conditions of the present study.

| Case | Boundary condition | Boundary surface(s) |
|---|---|---|
| Natural and Mixed Convection | $\theta = 1$ | Heater surface |
| Natural and Mixed Convection | $\theta = 0$ | Upper surface |
| Natural and Mixed Convection | $\partial\theta/\partial y = 0$ | Non-heated lower surface |
| Natural and Mixed Convection | $\partial\theta/\partial x = 0$ | Inlet and outlet |

The velocity boundary conditions are given in Table 2.

Table 2. Velocity boundary conditions of the present study.

| Case | Boundary condition | Boundary surface(s) |
|---|---|---|
| Natural and Mixed Convection | $u = v = 0$ | Upper and lower surfaces |
| Natural Convection | $u = v = 0$ | Inlet and outlet |
| Mixed Convection | $v = 0$ | Inlet and outlet |
| Mixed Convection | $u(y) \rightarrow$ fully developed profile | Inlet and outlet |

The stream function boundary conditions (Table 3) are derived from the velocity boundary conditions. Eqns. (46) and (47) are integrated, with the stream function arbitrarily set at zero at a given surface. For mixed convection, there is a bulk flow through the channel, therefore the stream function values at the upper surface and the lower surface are fixed different values. The velocity is non-dimensionalized by the average, or bulk-velocity of the channel, and y is non-dimensionalized by the height, such that y ranges from zero to one, so integrating the dimensionless velocity from y = 0 to y = 1 results in $\Psi = 0$ at the upper surface (arbitrarily chosen) and $\Psi = 1$ at the lower surface. The stream function values at the inlet and outlet depend on the velocity profile at the inlet and outlet, and are different for each value of $\eta$. Although holding the velocity profile constant (assuming fully-developed flow) at the inlet and outlet is not necessarily correct, the problem domain is large enough, such that the inlet and outlet are sufficiently far from the heat source, thereby minimizing the error due to the forced boundary conditions. For natural convection, there is no bulk flow, therefore, the stream function is a constant of zero for all surfaces.

The boundary conditions for vorticity are the most complicated to implement. Unfortunately, a no-slip velocity does not correspond to a vorticity boundary condition of zero. The vorticity boundary conditions are derived from the stream-vorticity equation.

Table 3. Stream function boundary conditions of the present study.

| Case | Boundary condition | Boundary surface(s) |
|---|---|---|
| Natural and Mixed Convection | $\Psi = 0$ | Upper surface |
| Natural Convection | $\Psi = 0$ | Inlet, outlet, and lower surface |
| Mixed Convection | $\Psi = 1$ | Lower surface |
| Mixed Convection | $\Psi(y) = -\int_{y=0}^{y} u(y)dy$ | Inlet and outlet |

At the top and bottom surfaces, the velocity is zero and the stream function is constant in the x-direction. Therefore, the stream-vorticity equation reduces to $\omega_B = \partial^2\Psi/\partial y^2$. At the inlet and outlet, for natural convection, the stream function is constant in the y-direction, with the stream-vorticity equation taking the form of $\omega_B = \partial^2\Psi/\partial x^2$, but for mixed convection, the stream function is allowed to change in both directions, therefore the full equation is required, $\omega_B = \partial^2\Psi/\partial x^2 + \partial^2\Psi/\partial y^2$. Implementing these equations to determine the boundary vorticity values is tricky and must be done with care because the boundary point is actually only a half-step from the first grid point. To accomplish this, a second order forward (or backward) difference equation was used for the first derivative, resulting in the following equation for the inlet,

$$\omega_{B,in} = \frac{\partial}{\partial x}\left(\frac{-\Psi_{2.5} + 4\Psi_{1.5} - 3\Psi_B}{2\Delta x}\right). \tag{104}$$

A central difference is then taken for the remaining derivative, looking forward and backward a half-step. Since the y-velocity is equal to zero at the inlet, then $\partial\Psi_B/\partial x = 0$ and the above equation becomes,

$$\omega_{B,i} = \frac{1}{2\Delta x^2}(-\Psi_3 + 5\Psi_2 - 4\Psi_1). \tag{105}$$

Table 4. Vorticity boundary conditions of the present study.

| Case | Boundary condition | Boundary surface(s) |
|---|---|---|
| Natural and Mixed Convection | $\omega_{B,L,i} = \frac{1}{2\Delta y^2}\left(-\Psi_{i,3} + 5\Psi_{i,2} - 4\Psi_{i,1}\right)$ | Lower surface |
| Natural and Mixed Convection | $\omega_{B,U,i} = \frac{1}{2\Delta y^2}\left(-\Psi_{i,NY-2} + 5\Psi_{i,NY-1} - 4\Psi_{i,NY}\right)$ | Upper surface |
| Natural Convection | $\omega_{B,in,j} = \frac{1}{2\Delta x^2}\left(-\Psi_{3,j} + 5\Psi_{2,j} - 4\Psi_{1,j}\right)$ | Inlet |
| Natural Convection | $\omega_{B,out,j} = \frac{1}{2\Delta x^2}\left(-\Psi_{NX-2,j} + 5\Psi_{NX-1,j} - 4\Psi_{NX,j}\right)$ | Outlet |
| Mixed Convection | $\omega_{B,in,j} = \frac{1}{2\Delta x^2}\left(-\Psi_{3,j} + 5\Psi_{2,j} - 4\Psi_{1,j}\right) + \frac{1}{\Delta y}\left(\frac{\Psi_{in,j+1} - \Psi_{in,j}}{\delta y_n} - \frac{\Psi_{in,j} - \Psi_{in,j-1}}{\delta y_s}\right)$ | Inlet |
| Mixed Convection | $\omega_{B,out,j} = \frac{1}{2\Delta x^2}\left(-\Psi_{NX-2,j} + 5\Psi_{NX-1,j} - 4\Psi_{NX,j}\right) + \frac{1}{\Delta y}\left(\frac{\Psi_{out,j+1} - \Psi_{out,j}}{\delta y_n} - \frac{\Psi_{out,j} - \Psi_{out,j-1}}{\delta y_s}\right)$ | Outlet |

A similar procedure is done for each boundary and the results are displayed in Table 4. It is important to mention that the grid spacing was held constant for the first 3 control volumes from the boundary to avoid the need for variable grid equations in the boundary conditions.

Next, the initial conditions must be defined, and are listed in Table 5. Natural convection assumes stagnation at the start of the problem, and mixed convection assumes fully developed flow, with the heater turned on at t = 0 in both cases.

Table 5. Initial conditions of the present study.

| Case | Initial condition |
|---|---|
| Natural Convection | $u_{i,j} = 0$<br>$\omega_{i,j} = 0$<br>$\Psi_{i,j} = 0$ |
| Natural and Mixed Convection | $v = 0$<br>$\theta = 0$ |
| Mixed Convection | $u_{i,j} = u_{B,in,j}$<br>$\omega_{i,j} = \omega_{B,in,j}$<br>$\Psi_{i,j} = \Psi_{B,in,j}$ |

In conclusion, boundary conditions have been derived and presented for temperature, velocity, stream function, and vorticity. The results have been organized into tables shown above. Next, the solution algorithm and details of the numerical scheme will be discussed.

### 3.2.6 Numerical solution method for discretized equations

There are many numerical schemes that can be used to solve the discretized equations that were derived in the previous sections, each with advantages and disadvantages. Explicit methods have only one unknown for each discretized equation, using old values for the N, S, E, and W values and updating the P value. This method is easy to implement but comes with a high computational cost. With simple problems on coarse grids, the ease of implementation might outweigh this increased computational cost. Implicit methods, on the other hand, have multiple unknowns in each discretized equation (N, S, E, W, and P for the present case). Because of this, the entire set of linear equations must be solved simultaneously, which is more difficult to implement. With complex problems (such as that in the present study), the additional up front work of implementing the implicit method is well worth the effort due to a greatly reduced computational cost. Also, explicit methods inherently limit the rate at which changes permeate through the problem domain, but implicit methods do not, leading to more accurate time-resolved results.

Implicit methods result in a penta-diagonal matrix, M, of $N \times N$ size, where N is the total number of grid points, such that $N = N_x \times N_y$. This matrix is very sparse and proper programming allows for a greatly reduced computational cost to obtain a solution. For the case of temperature, the matrix equation has the form,

$$[M][\theta] = [B], \tag{106}$$

where M contains the coefficients $B_P, B_E, B_W, B_N,$ and $B_S$, and matrix B contains the $B_0$ terms. First, matrixes M and B are populated based on the discretized energy equation, then the following algorithm is used to obtain a solution, with the goal being to algebraically turn matrix M into the identity matrix, therefore, making vector B the solution for $\theta$.

1. Divide each non-zero term in the first row of M and B by the value that falls on the primary diagonal of the first row (the value in location [1,1] of matrix M). This results in a value of one in the first row along the main diagonal.
2. Subtract $(\text{row } 1) \times [2,1]$ from row 2. This results in a value of zero for [2,1].
    a. Repeat for each row below row 2 that starts with a non-zero leading term (should only be 3 more rows): $\text{row N} = \text{row N} - (\text{row } 1) \times [N, 1]$. This results in a value of zero for the entire first column below the first row.
3. Divide each non-zero term in the second row of M and B by the value that falls on the primary diagonal of the second row (the value in location [2,2] of matrix M). This results in a value of one in the second row along the main diagonal.
4. Subtract $(\text{row } 2) \times [3,2]$ from row 3. This results in a value of zero for [3,2].
    a. Repeat for each row below the current row that has a non-zero value in the second column (should only be 5 rows): $\text{row N} = \text{row N} - (\text{row } 2) \times [N, 2]$. This results in a value of zero for the entire second column below the second row.
5. Repeat steps 3 and 4 for the 3rd through Nth row. This results in a matrix, M, that has all zero values below the main diagonal and values of one along the main diagonal. Once matrix M is turned into the identity matrix then vector B will be the solution to $\theta$.

6. Subtract $(\text{row N}) \times [\text{N}-1, \text{N}]$ from row (N-1).
    a. Repeat for all rows with a non-zero value in column N, subtracting $(\text{row N}) \times [\text{N}-2, \text{N}]$ from row (N-2), and so on. This results in a value of zero for all of column N above row N.
7. Subtract $(\text{row } (\text{N}-1)) \times [\text{N}-2, \text{N}-1]$ from row (N-2).
    a. Repeat for all rows with a non-zero value in column N-1, subtracting $(\text{row N}-1) \times [\text{N}-3, \text{N}-1]$ from row (N-2), and so on. This results in a value of zero for all of column N-1 above row N-1.
8. Repeat step 7 for all rows above row N-2. This results in zero values for all matrix locations above the main diagonal. Therefore, [M] = [I] and the final solution has been obtained for the current time step.
9. Assign $[\theta] = [\text{B}]$ as final solution.

This method is used for both the vorticity transport equation and the energy equation. Initially, an explicit solution method was attempted, but the computational time was unacceptably high. Implementing the above implicit method proved to me much more efficient.

For the stream-vorticity equation, an explicit forward time, central space (FTCS) algorithm was employed. The stream-vorticity equation is an elliptical equation and was solved accordingly. The solution algorithm is:

1. Starting with the first grid point in the x and y-directions, solve directly for $\Psi_{1,1}$ using the discretized form of the stream-vorticity equation. All values for $\Psi_{\text{N}}, \Psi_{\text{S}}, \Psi_{\text{E}}, \text{and } \Psi_{\text{W}}$ use the initial condition values.
2. Step through the indices, solving next for $\Psi_{2,1}$. All values except for $\Psi_{1,1} = \Psi_{\text{S}}$ in this case are still equal to the initial condition values, but $\Psi_{1,1}$ is equal to the new value assigned from step 1 according to Simpson's rule.
3. Directly solve for all other $\Psi$ values using the discretized equation.
4. Calculate the residual error for each grid point by,

$$\text{Res} = |\Psi_{\text{P}} - (\text{C}_{\text{E}}\Psi_{\text{E}} + \text{C}_{\text{W}}\Psi_{\text{W}} + \text{C}_{\text{N}}\Psi_{\text{N}} + \text{C}_{\text{S}}\Psi_{\text{S}} + \text{C}_{\text{P}}\omega_{\text{P}})|. \tag{107}$$

5. Sum up the residual values for all grid points.

a. If total residual is greater than $10^{-6}$ then repeat steps 1 through 4.
b. If total residual is less than $10^{-6}$ then solution for stream function values has been obtained and no further iterations are required.

This algorithm has the advantage of being an explicit method, which is easy to implement. The computational time for this step was found to be acceptable, as the stream function values were not found to dramatically change from one time step to the next.

3.2.7 Solution algorithm for mixed convection problem

The discretized equations have been developed, and the implicit and explicit methods of solving those equations have been explained. With forced convection (where buoyancy effects are neglected), the vorticity equation is first solved, then, the energy equation can be solved. The results of the energy equation do not impact the momentum equation. However, in natural and mixed convection problems, the energy equation and the vorticity equation are not independent due to the buoyancy term in the vorticity transport equation. Therefore, the vorticity transport equation must be solved in parallel with the energy equation. The overall solution algorithm is:

1. Initial setup phase
    a. Define dimensionless parameters for current numerical run.
    b. Define grid spacing for current $\eta$ and $\delta$ values.
    c. Calculate $\phi, \hat{\mu}, \text{and } Da$, values at each grid point, where the porosity varies and goes to unity in the fluid layer.
    d. Set the boundary conditions and the initial conditions.
    e. Calculate face velocities and average velocities of the control volumes and calculate the velocity magnitude for each grid point.
    f. Calculate the effective conductivity ratio, $\lambda$, using the updated velocity values.
    g. Calculate coefficients for the discretized stream-vorticity equation from Eqns. (60-(65). These coefficients do not change with each iteration.
2. Main code loop - repeated until the desired time is reached or until the solution reaches steady-state.
    a. Calculate new vorticity values:

i. Calculate the coefficients for the discretized vorticity transport equation (Eqn. (84) from Eqns. (85-(95)). These coefficients change with each iteration.
ii. Generate matrices M and B of Eqn. (106).
iii. Use the penta-diagonal matrix solver described in the previous section to obtain the solution for the vorticity at the next time step.

b. Calculate new stream function and velocity values:
i. Calculate new stream function values from Eqn. (59) using the explicit method described in the previous section. Repeat until the residual is below the desired level.
ii. Calculate new stream function values at the control volume corners using the averaging Eqns. (66-(69).
iii. Calculate new velocity values at the control volume faces, calculate new average velocity values in the control volumes, and calculate new velocity magnitude values (Eqns. (70-(76).

c. Calculate new boundary conditions for the vorticity based on the new stream function values from Table 4.

d. Calculate new temperature values:
i. Calculate the coefficients for the discretized energy equation (Eqn. (96) from Eqns. (97-(103)). These coefficients change with each iteration
ii. Generate matrices M and B of Eqn. (106).
iii. Use the penta-diagonal matrix solver described in the previous section to obtain the solution for the temperature at the next time step.
iv. Calculate new temperature boundary conditions using Table 1.

e. Check for convergence:
i. Calculate the Nusselt number and the percentage change of the Nusselt number since the last iteration.
ii. Conduct the energy balance on the overall system.

iii. If the energy balance and Nusselt number criteria are met (described in the next section), then the solution is considered to have reached steady-state. Otherwise, continue iterations until solution converges or until solution reaches steady oscillations that are not dampening out (Figure 10).

3. Write data to file and terminate code.

### 3.2.8 Nusselt number, energy balance, and convergence criteria

The Nusselt number represents the dimensionless heat transfer coefficient of the system and needs to be calculated accurately. The method is outlined by Bagchi [1], who shows that using a first-order finite difference equation to calculate the Nusselt number achieves a grid independent solution at a significantly coarser grid. For the present problem the following equations result:

$$\mathrm{Nu} = \frac{1}{\delta}\sum\nolimits_{\mathrm{heater}} \lambda_{\mathrm{i},1}\left(\frac{1-\theta_{\mathrm{i},1}}{0.5\Delta \mathrm{y}_1}\right)\Delta \mathrm{x}_{\mathrm{i}}, \tag{108}$$

$$\Delta \mathrm{E} = \frac{\mathrm{Q}_{\mathrm{top}} + \mathrm{Q}_{\mathrm{exit}} - \mathrm{Q}_{\mathrm{in}}}{\mathrm{Q}_{\mathrm{in}}}, \tag{109}$$

$$\mathrm{Q}_{\mathrm{top}} = \sum\nolimits_{\mathrm{top}} \lambda_{\mathrm{i,NY}}\left(\frac{\theta_{\mathrm{i,NY}} - 0}{0.5\Delta \mathrm{y}_{\mathrm{NY}}}\right)\Delta \mathrm{x}_{\mathrm{i}}, \tag{110}$$

$$\mathrm{Q}_{\mathrm{in}} = \sum\nolimits_{\mathrm{heater}} \lambda_{\mathrm{i},1}\left(\frac{1-\theta_{\mathrm{i},1}}{0.5\Delta \mathrm{y}_1}\right)\Delta \mathrm{x}_{\mathrm{i}}, \tag{111}$$

$$\mathrm{Q}_{\mathrm{exit}} = \sum\nolimits_{\mathrm{exit}} \mathrm{u}_{\mathrm{NX,j}}\mathrm{Pe}\theta_{\mathrm{NX,j}}\,\Delta \mathrm{y}_{\mathrm{j}}. \tag{112}$$

The solution was considered to have converged when the change in the Nusselt number from one iteration to the next was consistently below 0.001% and the energy balance was consistently below three percent. In most cases, the energy balance reached a value on the order of $10^{-6}$. These values were chosen based on experience after showing that once the change with each iteration dropped below these thresholds, no significant change would occur even when thousands of additional iterations were run.

In some cases, the Nusselt number continued to oscillate indefinitely as seen in Figure 10. In these cases, the code was allowed to run for significantly longer until the

oscillations became repeatable and consistent. In these cases, an average Nusselt number was calculated from the results over several steady state cycles.

In order to accelerate the solution convergence, the code was modified to allow the user to vary the time step with each batch of iterations. This greatly reduced the amount of time required to reach the convergence criteria, allowing the user to increase the time step until the solution began to go unstable, then slightly backing off the time step. In addition, it was observed that the Nusselt number stabilized much faster than the energy balance due to the significant amount of time required for the changing temperature profile effects to physically reach the outlet of the problem domain. It was also observed that the time step for the temperature could be much higher than the time step for the vorticity equation without causing instability. Therefore, the code was modified again to allow for the temperature time step to be set independently from the vorticity time step. This modification greatly reduced the number of iterations required for the energy balance to converge. However, during the final iterations of each run, both time steps were always set equal to ensure a physically accurate final solution, though not necessarily a time accurate solution.

In conclusion, the governing equations have been derived and discretized for the control volumes, the numerical methods have been explained, the boundary conditions and initial conditions have been outlined, and the convergence criteria has been established.

# Chapter 4. Numerical Results

To present the numerical results of the present problem several items must be first addressed. First, the grid spacing must be shown to be sufficiently fine to produce grid-independent solutions, second, the solution must converge and reach steady, repeatable results, and third, the code must be able to reproduce existing numerical/experimental results and classical solutions.

## 4.1 Grid independence, stability, and convergence

As discussed in previous sections, a variable grid was used in the present problem, enabling grid independent solutions at a much coarser mesh. As the number of grid points increases, the time for each iteration increases exponentially (Figure 31). Due to the large number of time steps necessary to reach steady-state, the length of each iteration must be kept to a reasonable level. The variable grid was shown to achieve the same degree of accuracy in approximately $1/10^{th}$ the computational time.

Stability concerns also arise when generating numerical results. In some cases, particularly in the transition region between the natural convection regime and the forced convection regime, the solution would converge to a certain Nusselt number when given a small, less-aggressive time step, but would converge to a different Nusselt number when perturbed. In these cases, the solution would be intentionally perturbed to produce consistent results.

In conclusion, the variable grid used in the present problem has been shown to generate grid-independent solutions and the code is capable of producing consistent and stable numerical results.

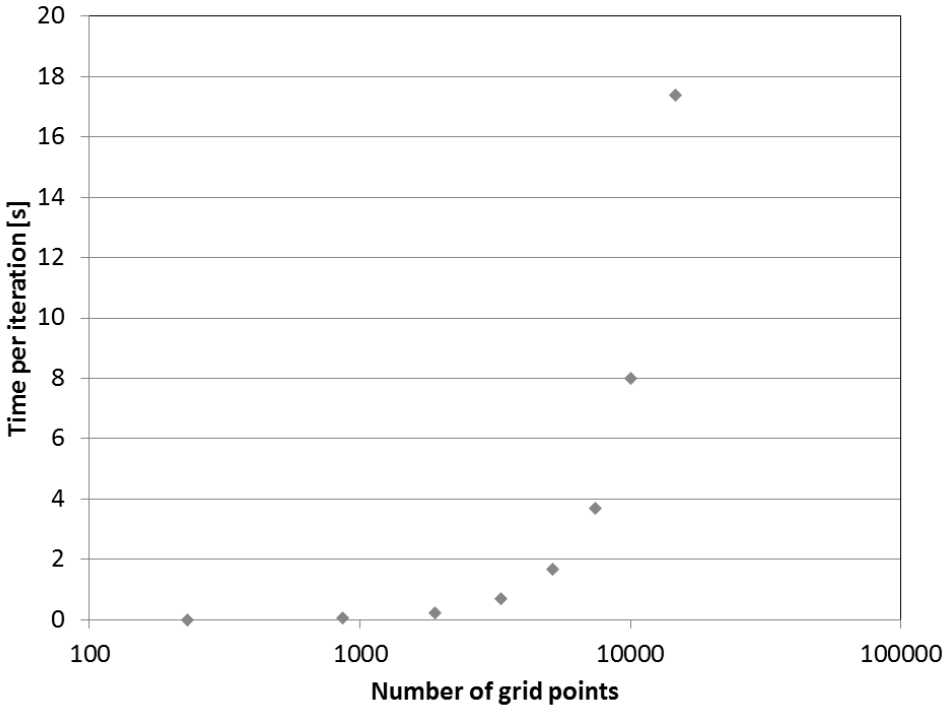


Figure 31. Iteration time verses number of grid points.

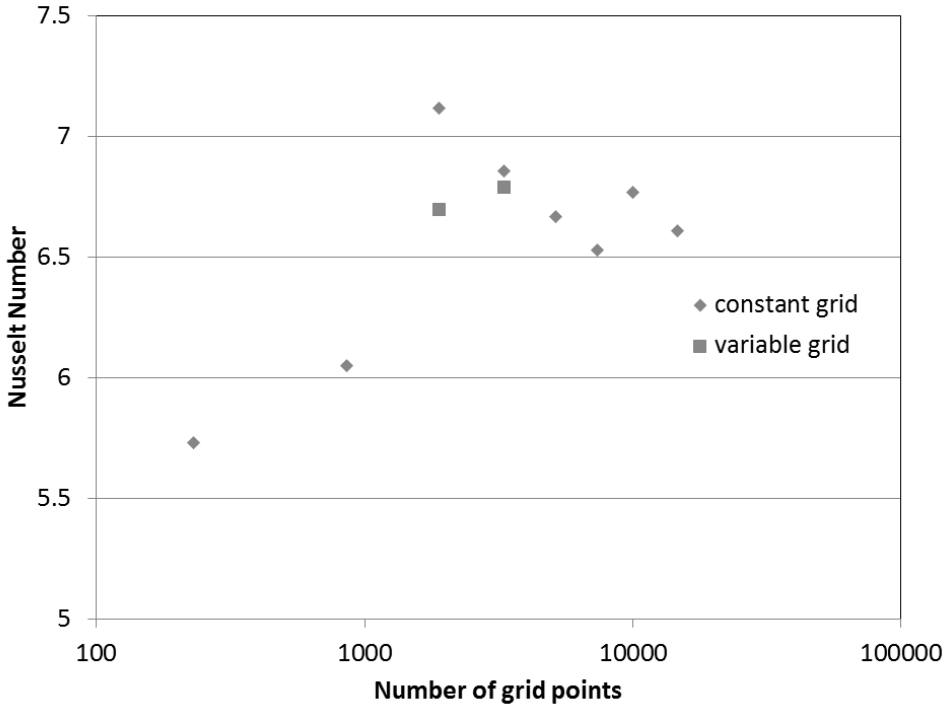


Figure 32. Comparison of constant grid to variable grid convergence ($\eta = 0.9$, RaDa = 100, Pe = 30).

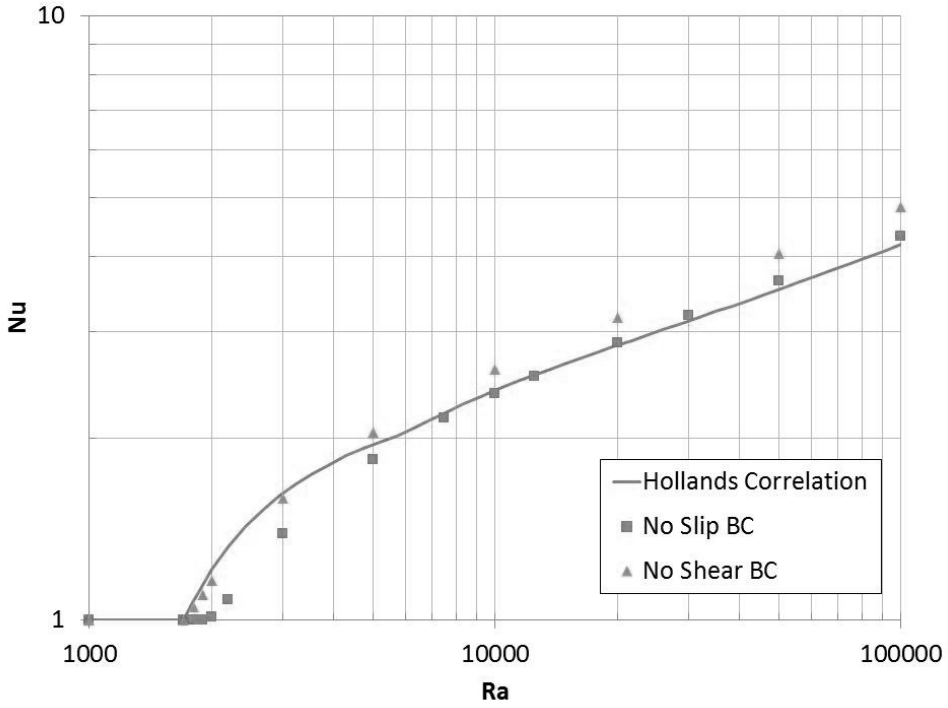


Figure 33. Comparison of existing to current results for Rayleigh-Bénard convection problem.

## 4.2 Comparison to existing numerical solutions and experimental data

In order to confirm that the code produces reliable numerical results, the boundary conditions and parameters were modified to reproduce existing classical, numerical, and experimental results.

### 4.2.1 Rayleigh-Bénard convection

The problem of Rayleigh-Bénard convection considers a two-dimensional domain of fluid with a fully heated bottom and looks at a range of Rayleigh number values. No-slip boundary conditions are applied at all surfaces, constant temperature at the top and bottom are applied and adiabatic conditions are applied at the side walls. Hollands [54] gathered experimental data from a wide range of studies and developed a suitable correlation equation to fit to the data. Numerical results from the present problem are compared to this correlation equation for two boundary conditions, showing good agreement (Figure 33).

The no shear boundary condition accurately captures the critical Rayleigh number at the onset of convection, but over predicts the Nusselt number slightly at higher

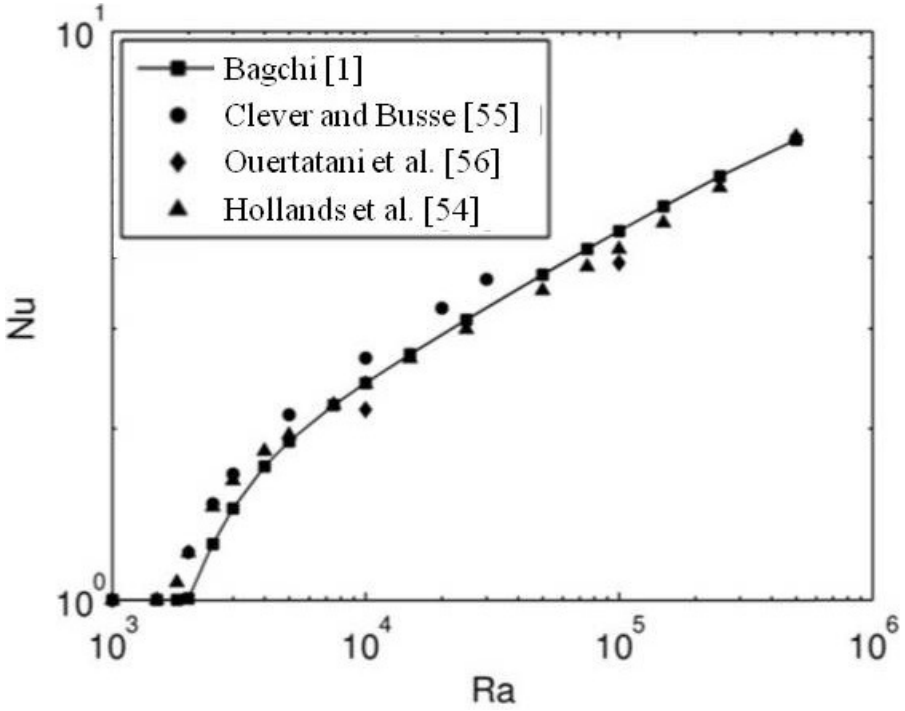


Figure 34. Over prediction of critical Rayleigh number from Bagchi numerical results [1].

Rayleigh numbers. The no shear boundary condition more accurately tracks the experimental results at higher Rayleigh numbers, but over predicts the critical Rayleigh number. Prior numerical work also over predicts the critical Rayleigh number (Figure 34).

### 4.2.2 Horton-Rogers-Lapwood problem

The Horton-Rogers-Lapwood problem is similar to the Rayleigh-Benard problem, considering a 2D domain containing now a full porous layer saturated with fluid, with a fully heated bottom and looks at a range of Rayleigh number values. No-slip boundary conditions are applied at all surfaces, constant temperature at the top and bottom are applied and adiabatic conditions are applied at the side walls.

Bagchi [1] compared his numerical results to several existing numerical and experimental results [33,48,54-58], showing good agreement (Figure 35-Figure 36). For the sake of simplicity, the numerical results from the present study are compared to Bagchi's results, showing excellent agreement (Figure 37).

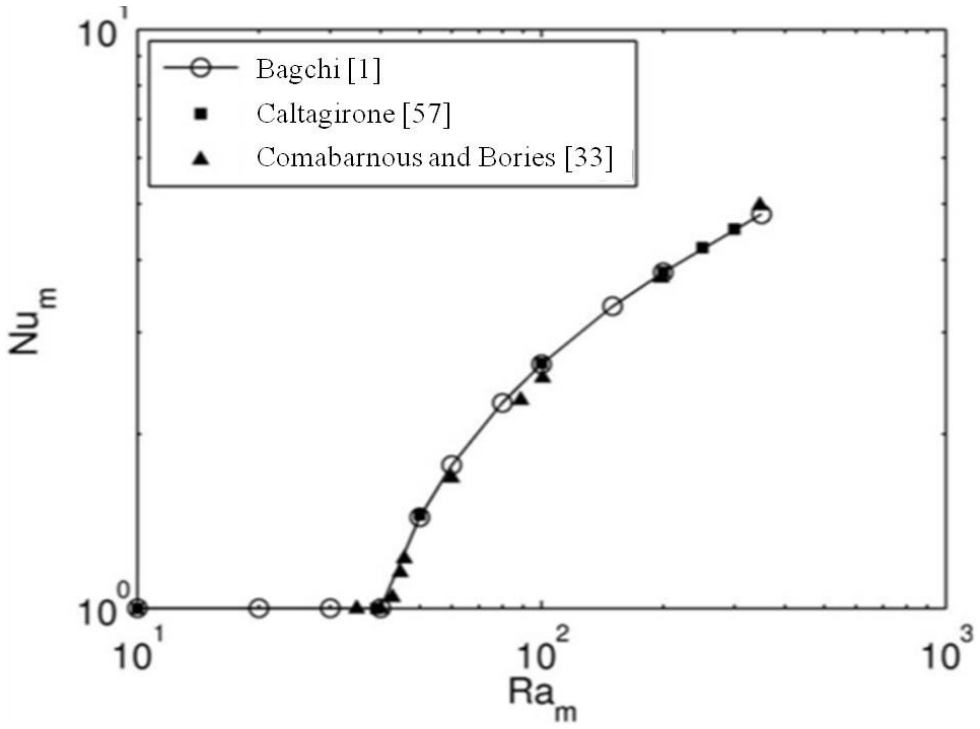


Figure 35. Bagchi results compared to existing numerical results [1].

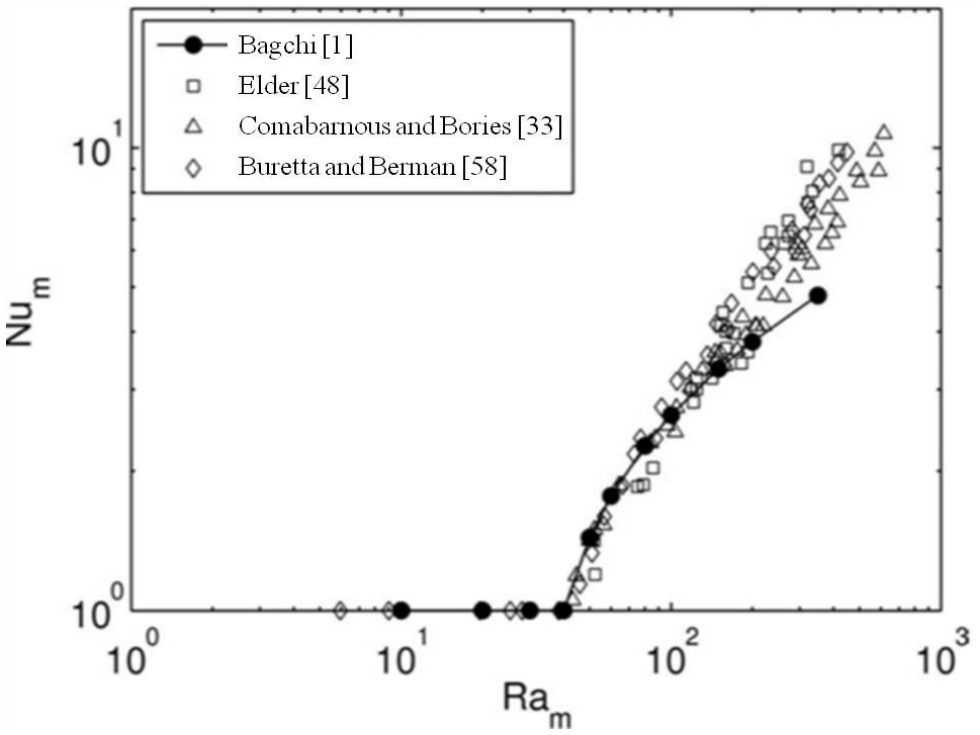


Figure 36. Bagchi results compared to existing experimental results [1].

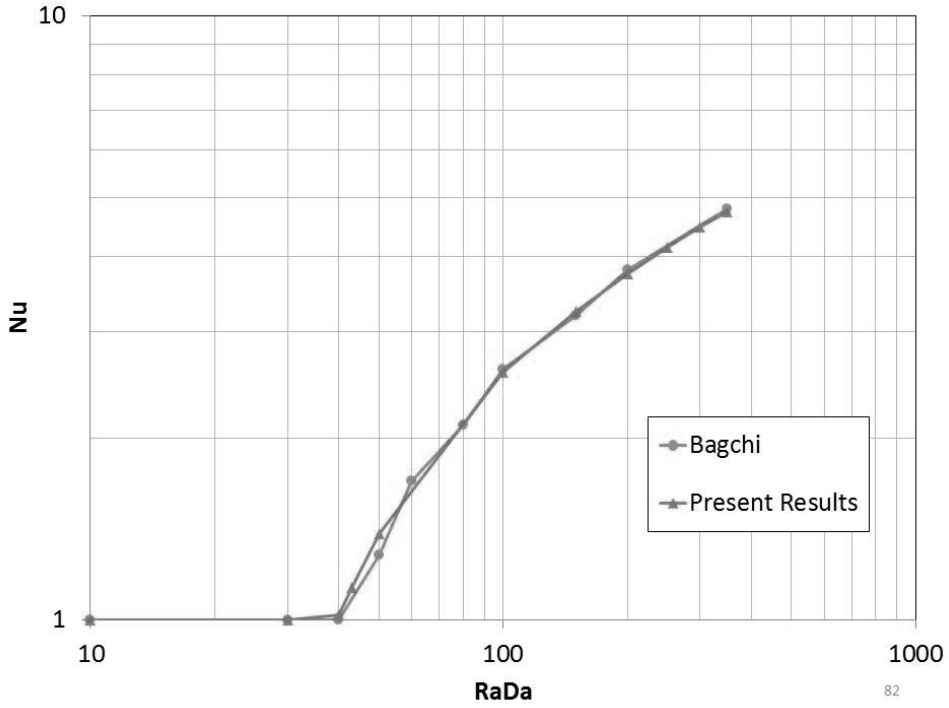


Figure 37. Comparison of current numerical results to existing results for Horton-Rogers-Lapwood problem.

The code from the present problem clearly is able to reproduce existing natural convection numerical results, further demonstrating the legitimacy and accuracy of the code.

### 4.2.3 Natural convection in fluid-superposed porous layers

Comparisons up to this point have not considered the interface between the fluid and porous layers. Bagchi [1] reconsidered the Horton-Rogers-Lapwood problem but allowed the height of the porous layer to vary, only filling a fraction of the total chamber with porous material, thus bringing interfacial concerns into the picture. In addition, the size of the heater on the base was varied. No-slip boundary conditions are applied at all surfaces, constant temperature at the top and heater surfaces are applied and adiabatic conditions are applied at the side walls and the non-heated bottom surface. The porous height ratio and heater size were varied, along with a range of other parameters.

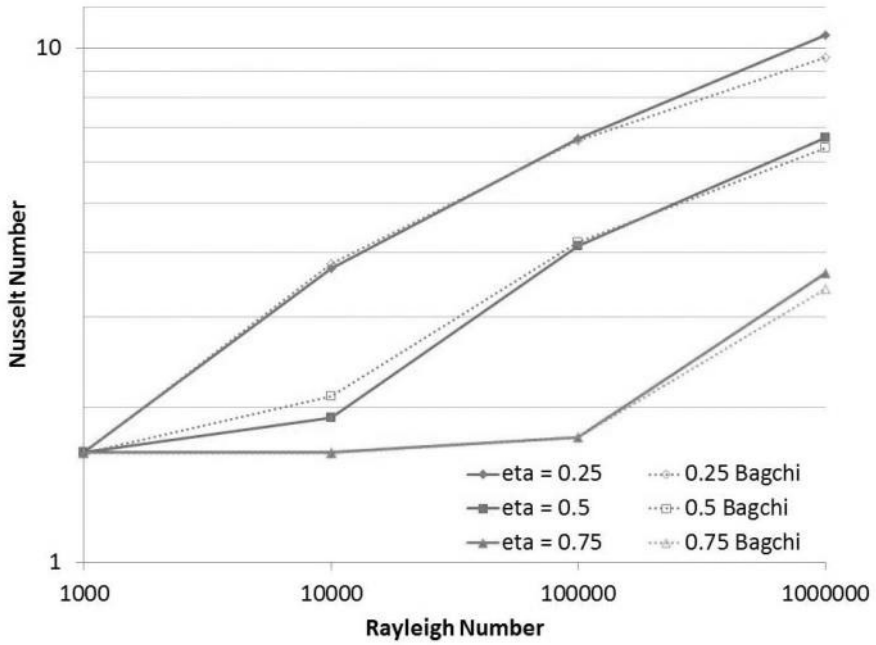


Figure 38. Comparison of current numerical results to Bagchi results for natural convection in fluid-superposed porous layers heated locally from below ($\delta = 0.5$, $Da = 10^{-6}$, $Pr = 7$, $\kappa = 1$).

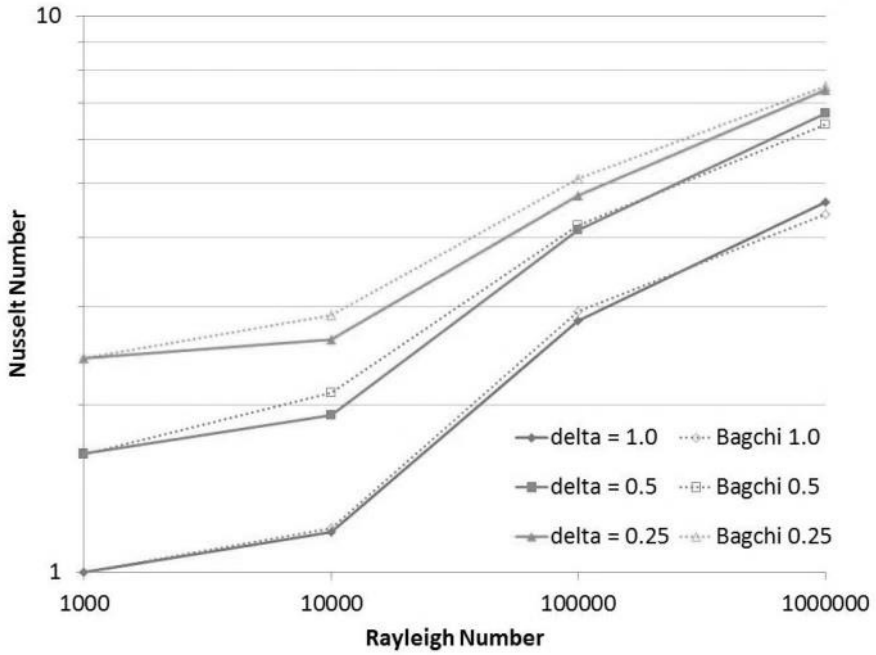


Figure 39. Comparison of current numerical results to Bagchi results for natural convection in fluid-superposed porous layers heated locally from below ($\eta = 0.5$, $Da = 10^{-6}$, $Pr = 7$, $\kappa = 1$).

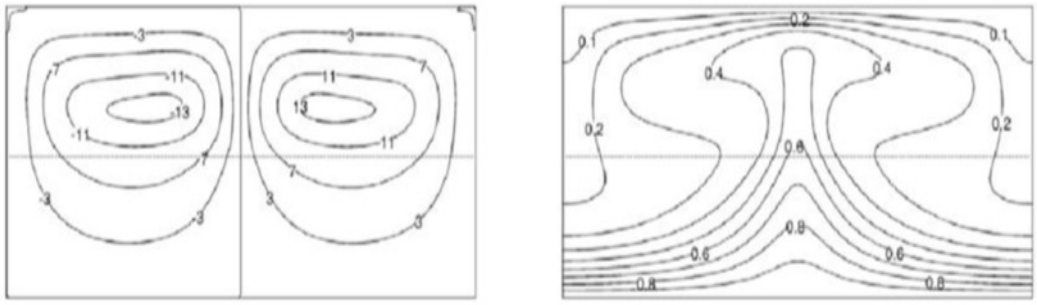

Figure 40. Natural convection streamlines and isotherms from Bagchi results [1] ($\eta = 0.5$, $\delta = 1.0$, $Ra = 10^5$).

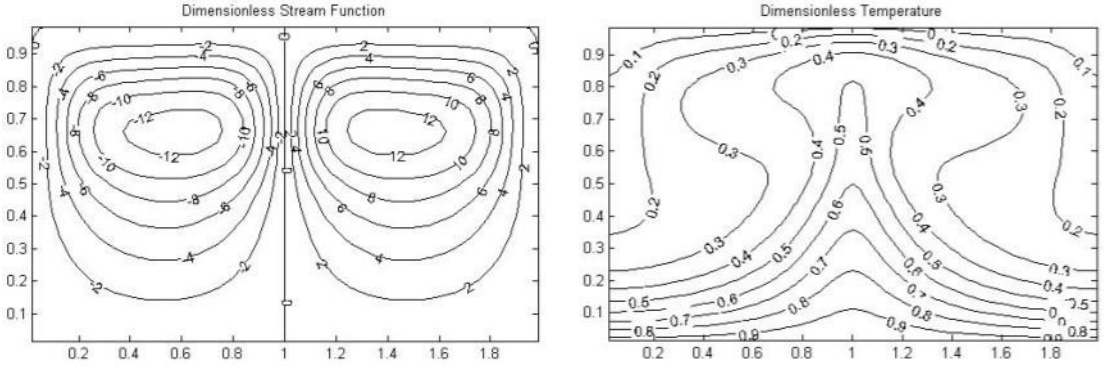


Figure 41. Natural convection streamlines and isotherms from present results [1] ($\eta = 0.5$, $\delta = 1.0$, $Ra = 10^5$).

Current results show good agreement with Bagchi's results when varying the dimensionless height ratio and when varying the dimensionless heater size. The trends are quite similar, but there are discrepancies at several points. This could be due to more stringent convergence criteria in the present study.

Streamlines and isotherms are also compared to Bagchi's results, showing excellent agreement. An example of the results is presented in Figure 40 and Figure 41.

### 4.2.4 Mixed convection in a porous domain

More importantly, the code for the present work must be compared to existing mixed convection studies. Although mixed convection in porous media data is less plentiful, the work of Lai and Kulacki [40] provides an excellent numerical and experimental comparison for the present work.

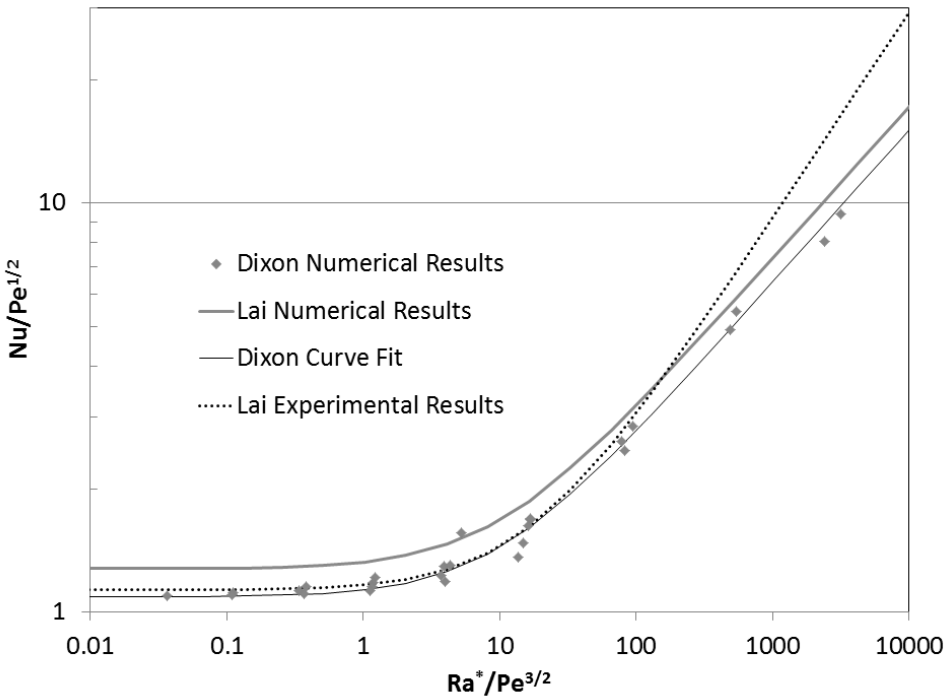


Figure 42. Comparison of mixed convection numerical results between the present study and the work of Lai and Kulacki [40] for a full porous layer ($\eta = 1$, $\delta = 1$).

All values on Figure 42 were calculated using the heater length and the stagnant thermal conductivity. The Rayleigh number is based on the heat flux rather than the temperature difference.

As can be seen in Figure 42, the numerical results from the present study show excellent agreement with Lai's experimental results in the forced convection and transition regimes and show good agreement with Lai's numerical results in the free convection regime. The reason for the discrepancy could be due to the inclusion of the Forchheimer and Brinkman terms in the present study, coupled with a higher range of Peclet number and Rayleigh number, or could be due to the constant flux verses constant temperature boundary condition discrepancy. It also could be an oversimplification to attempt to collapse all the data onto one curve. In any case, the results show fairly good agreement.

The numerical results of Prasad, Lai, and Kulacki [59] also provide an excellent comparison. These results capture the critical Peclet number phenomenon. Results from the present study show excellent agreement across the entire range of parameters,

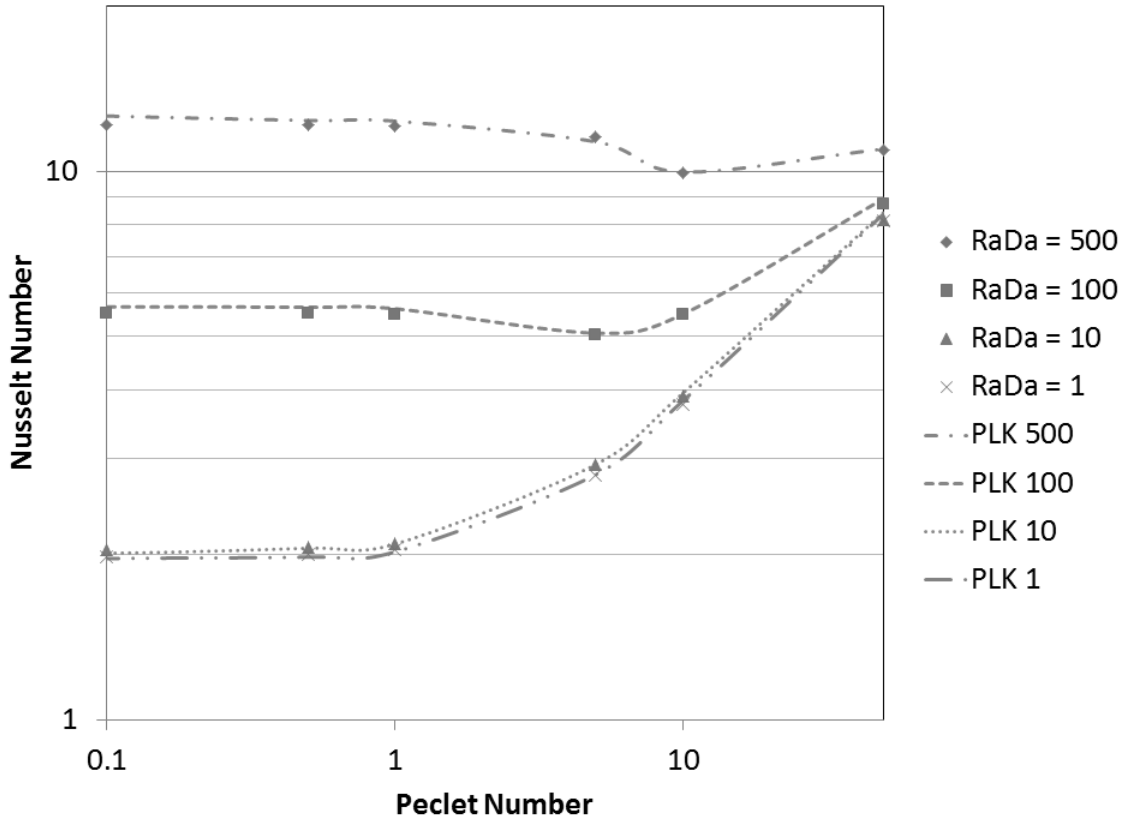


Figure 43. Comparison of numerical results to those of Prasad, Lai, and Kulacki [59] results for mixed convection in a full porous layer.

showing the same critical Peclet number for all cases. In this case, the Rayleigh-Darcy number is based on the temperature difference and the porous layer height. The Nusselt number and Peclet number are also based on the porous layer height.

In conclusion, the code for the present study has been compared to a range of natural convection and mixed convection results, showing good agreement in all cases. This suggests that the code is properly working and is capable of producing reliable results. The next step is to numerically solve the problem of mixed convection with a varying porous layer height.

## 4.3 New Results

Now that the code has been shown to be capable of reproducing existing, well established numerical and experimental results, new results can now be presented. First, the effect of thermal conductivity variation on the overall Nusselt number, including both

the conductivity ratio between solid and fluid phases and the effects of dispersion, are presented. Next, the impact of including various terms in Darcy's law is explored, and the effects of variation of Prandtl number and Darcy number are also presented. Results showing the critical Peclet number are then presented. Finally, the effects of variation of the porous layer height ratio on the overall Nusselt number are presented in great detail. For all results presented, the Rayleigh number and Peclet number are varied. In most cases, the Rayleigh-Darcy number is used, but when the Darcy number is being varied, then the Rayleigh number is used.

### 4.3.1 Thermal Conductivity Variation

As shown in previous studies [1,40], varying the conductivity ratio can have a large effect on the overall Nusselt number results. To explore this, the conductivity ratio was varied from a value of 1 to 8 (Figure 44). In addition, the correction for the effects of dispersion was turned off and on to provide comparison.

When the Nusselt number is based on the fluid thermal conductivity, there is a dramatic difference between the Nusselt number results using various conductivity ratios. When the Nusselt number is based on the stagnant thermal conductivity of the porous medium, there is less variation, although it is still significant at lower Rayleigh number where the heat transfer by conduction is more substantial. Therefore, accurately determining the conductivity ratio is important in order to properly match experimental and numerical results.

The unsteady behavior seen in previous studies [1,35,36,40] was similarly observed in the present study and can be seen in Figure 46, however, the oscillations were only observed in a transition region. At a given Peclet number and conductivity ratio, there is a range of values for the Rayleigh-Darcy number that exhibits oscillatory behavior. When above or below this range, the Nusselt number converges to a steady value. It can also be seen that increasing the conductivity ratio shifts this range upward. In the RaDa = 300, $\kappa = 2$ case, it can be seen that the solution is borderline stable, nearly reaching a steady value before shifting back up and repeating the sequence. This case is considered borderline stable.

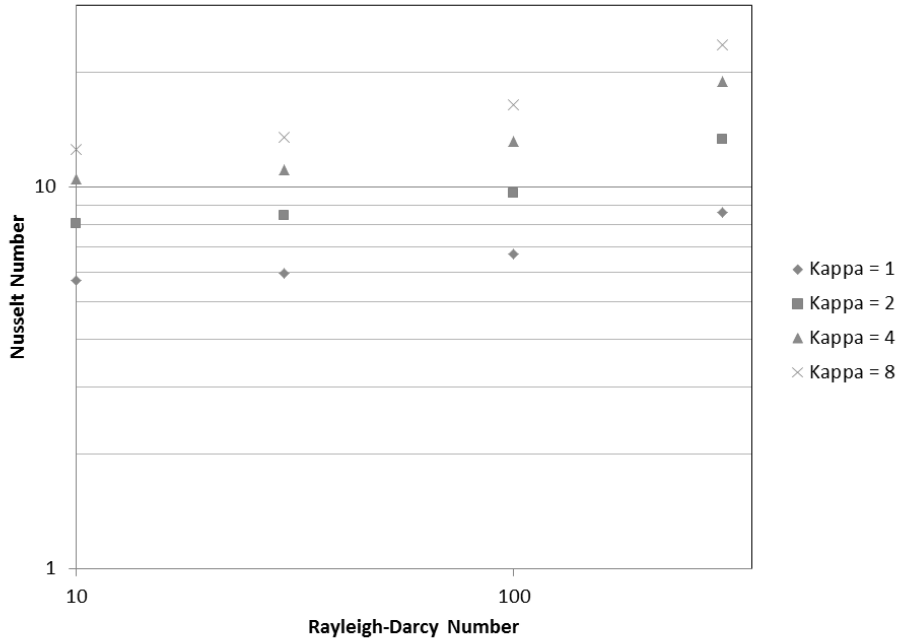


Figure 44. Effect of conductivity ratio variation (Pe = 30, η = 0.9) when Nusselt number is based on the fluid conductivity.

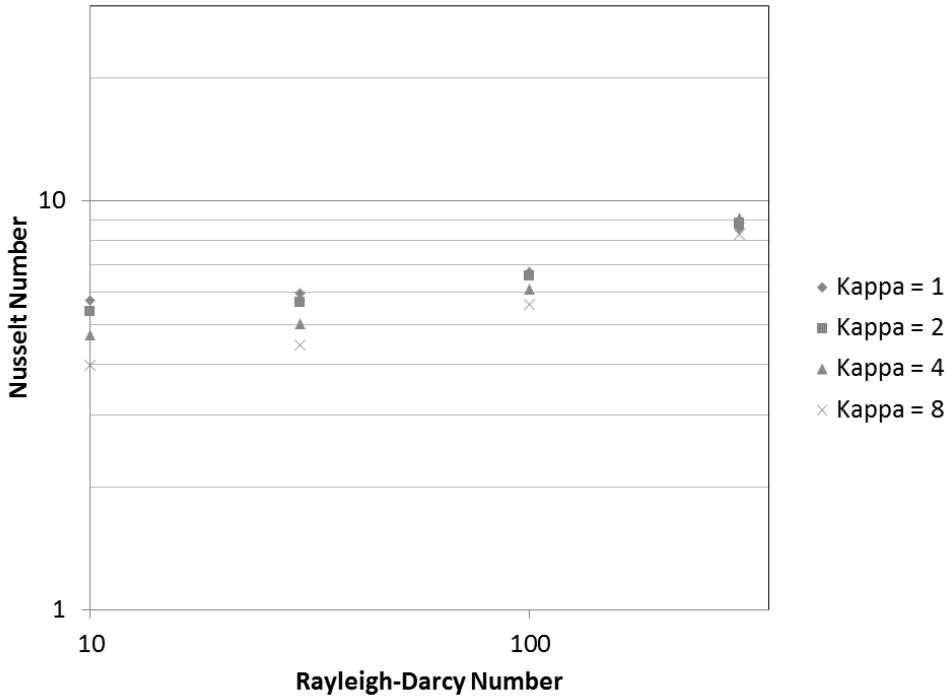


Figure 45. Effect of conductivity ratio variation (Pe = 30, η = 0.9) when Nusselt number is based on the stagnant conductivity.

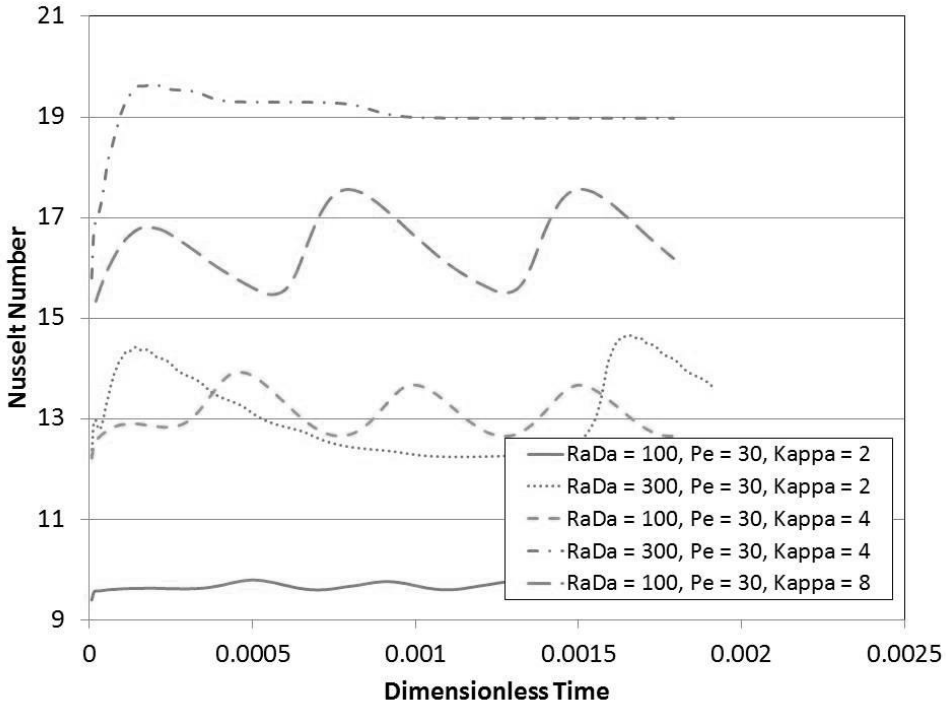


Figure 46. Transience in Nusselt number at various conductivity ratios ($\eta = 0.9$).

Prior work [12] showed the effect of dispersion and the tortuosity on the effective thermal conductivity. Results correlated the effective conductivity ratio to the local Peclet number (Figure 3), and this correlation was implemented into the code, updating the effective conductivity matrix with each iteration based on the updated local velocity at each grid point. The effects were shown to be minor at the range of Peclet number under consideration in the present study when compared to the effects of the conductivity ratio, but not negligible (Figure 47).

In conclusion, the conductivity ratio must be determined accurately, and accounting for the effects of dispersion can be important at some flow rates found in the present study.

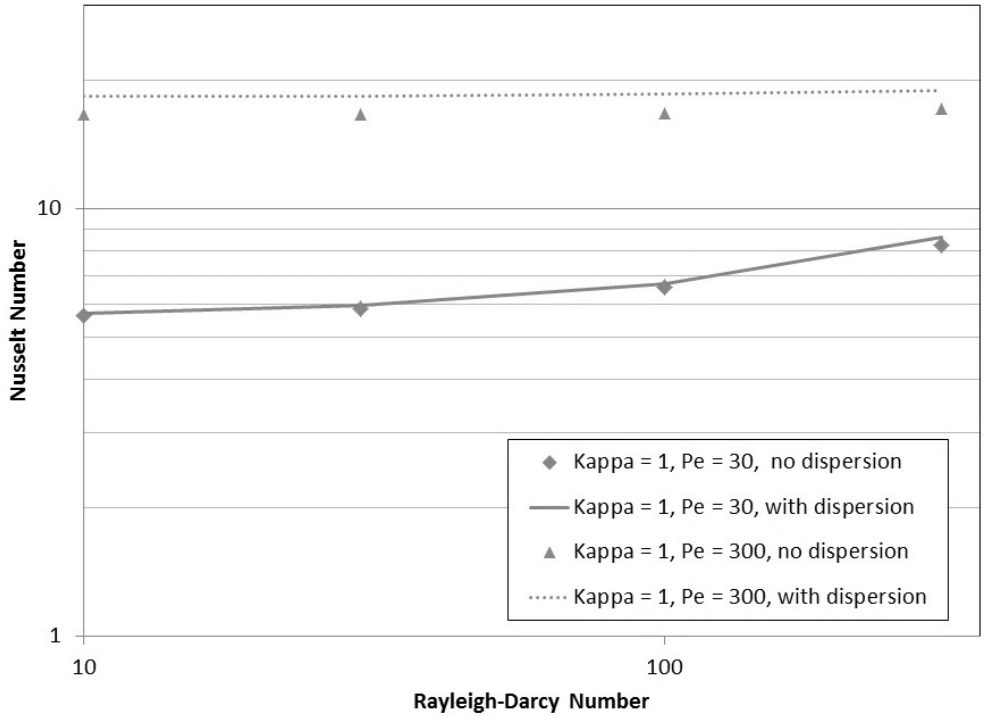


Figure 47. Effects of dispersion on Nusselt number results ($\eta = 0.9$).

4.3.2 Darcy's Law variation

As discussed in the literature review, there is much debate regarding the appropriateness of the various forms of Darcy's law. The form used in the present study contains the Darcy term, the Brinkman term, the Forchheimer term, the buoyancy term, the convective terms, the transient term, and the variable porosity terms. This section explores the impact of the various terms on the numerical results of the present study.

First, the Forchheimer term was turned off and on to determine whether or not it is significant to the present study. As can be clearly seen in Figure 48, the Forchheimer term has negligible effect on the overall Nusselt number of the system below Peclet numbers of roughly 1000. At Pe = 1000, neglecting the Forchheimer term causes an error in the Nusselt number of five percent. Above Pe = 1000, the results are unstable without the Forchheimer term.

Next, the Brinkman term was removed from the porous domain. The results in Figure 49 show negligible difference between the Nusselt number results containing the Brinkman term and those not containing the Brinkman term. The maximum discrepancy was 2.1%.

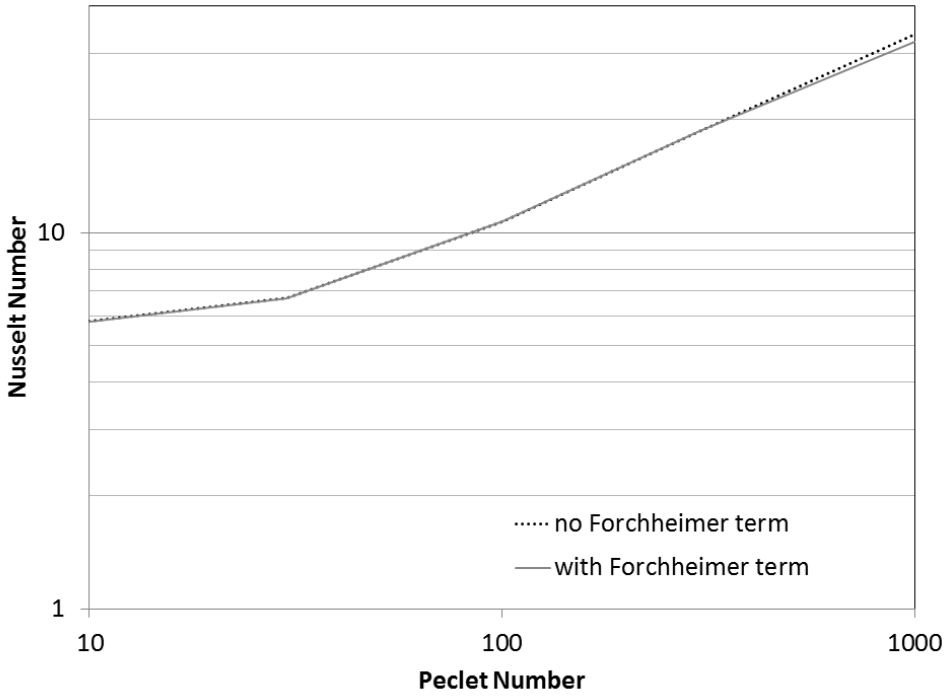


Figure 48. Effect of Forchheimer term on Nusselt number results (η = 0.9, RaDa = 100).

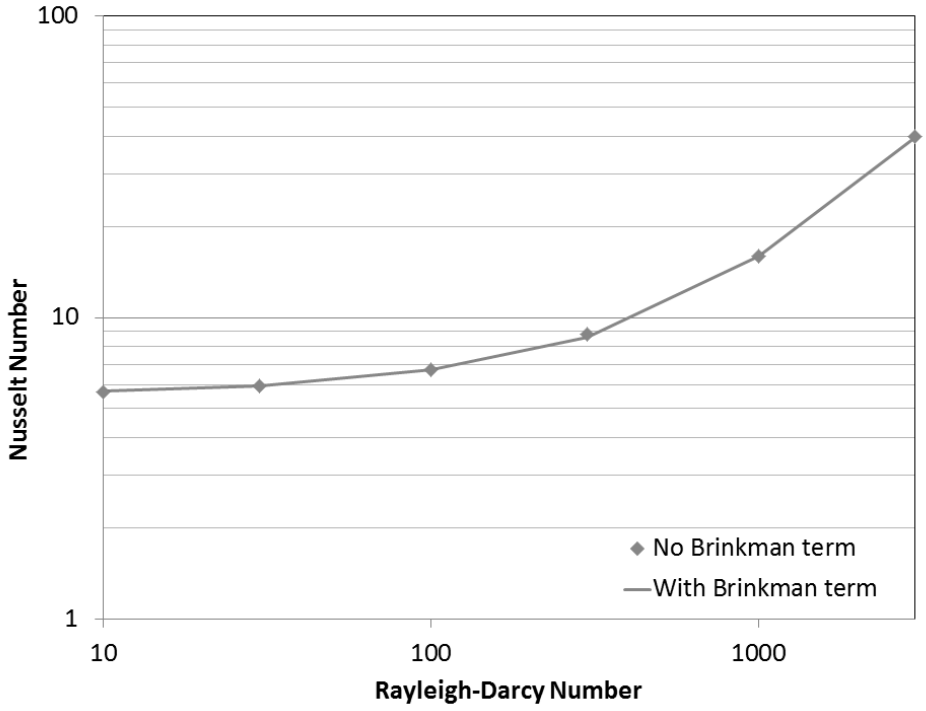


Figure 49. Effect of Brinkman term on Nusselt number results (η = 0.9, Pe = 30).

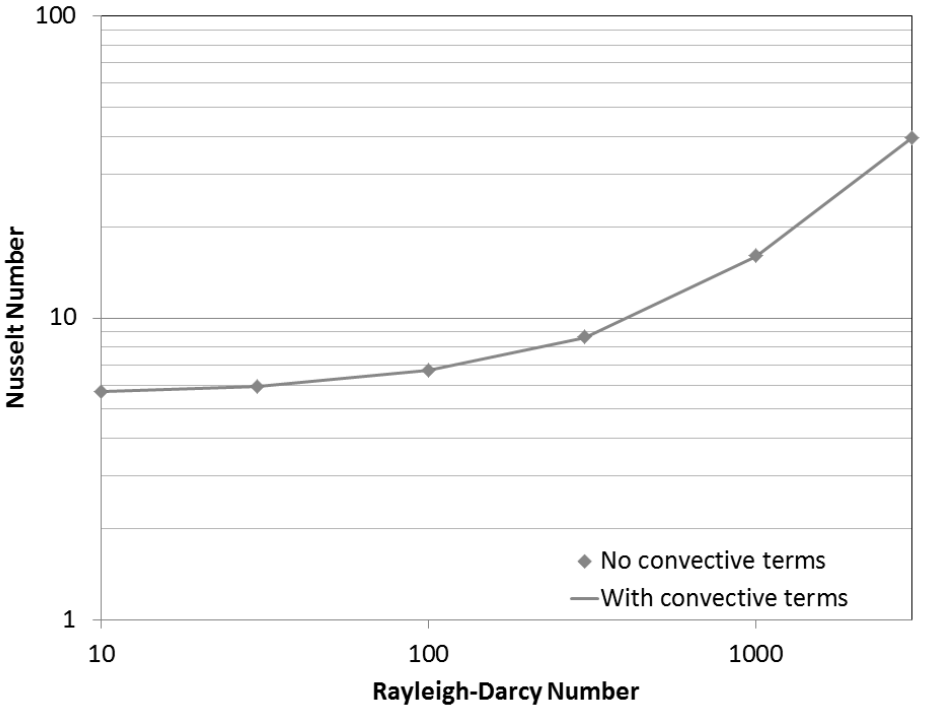


Figure 50. Effect of convective terms on Nusselt number results (η = 0.9, Pe = 30).

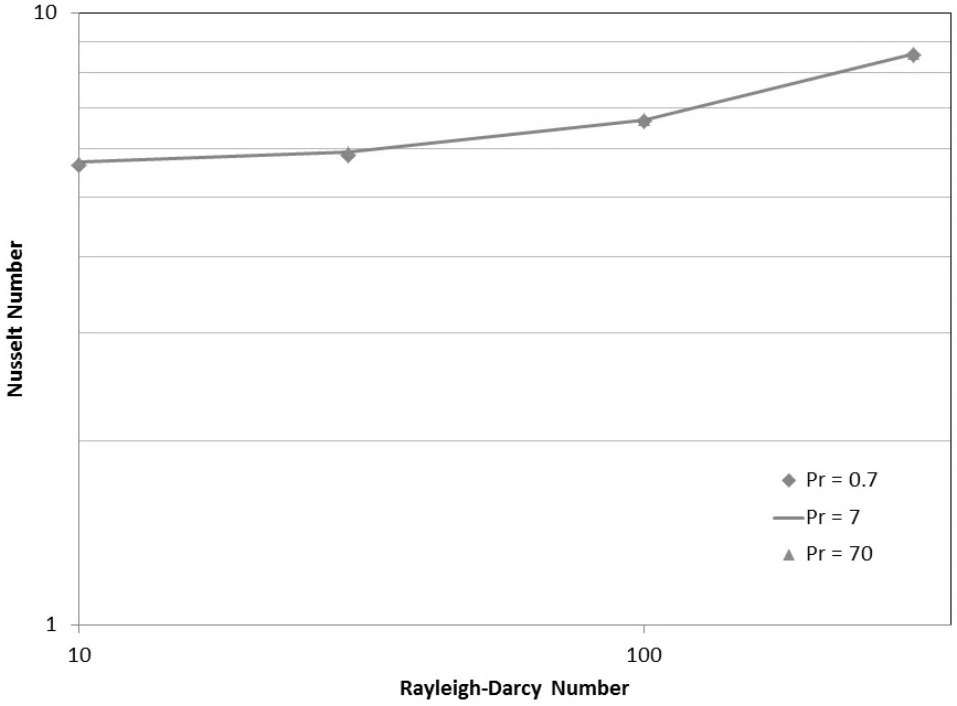


Figure 51. Effect of Prandtl number on overall Nusselt number results (η = 0.9, RaDa = 100).

Finally, the convective terms on the left hand side of Eqns. (27-(28) were omitted from the porous domain. The overall Nusselt number showed negligible difference between the results including the convective terms and the results omitting the convective terms (Figure 50). The maximum difference was found to be 0.37%.

In conclusion, the most basic form of Darcy's law (including the buoyancy term) provides a very good approximation for the present study. For the overall Nusselt number of the system, no significant improvement in accuracy was made by including the Forchheimer, Brinkman, or convective terms.

4.3.3 Prandtl number variation

The Prandtl number was varied, ranging from 0.7 to 70. As shown in a previous study [1], Prandtl number variation produces negligible changes in the overall Nusselt number of the system. This is important to establish, because the Prandtl number varies by approximately a factor of two across the range of temperatures used in the experiments of the present study. Based on Figure 51, this variation does not need to be corrected.

4.3.4 Darcy number variation

Next, the Darcy number was varied. In this case, the Rayleigh number was kept constant, not the Rayleigh-Darcy number as in previous examples. This was done so the temperature difference was effectively held constant for each column of data points.

Clearly, increasing the Darcy number can have a large impact on the overall Nusselt number of the system. The porous layer provides a large resistance to the effects of buoyancy. At low Darcy numbers (below $10^{-6}$) and low Rayleigh number (below $2 \times 10^{8}$), varying the Darcy number by several orders of magnitude has surprisingly little effect on the Nusselt number, but increasing the Darcy number to $10^{-4}$ has a significant effect on the overall heat transfer results. At low Darcy numbers, the heat transfer is conduction-dominated within the porous layer, but at higher Darcy numbers, the fluid is less restricted and the heat transfer becomes convection-dominated, moving towards the solution for a fluid layer. It is also important to notice that the Nusselt number is actually higher for a Da = $10^{-4}$ than for a fluid layer at high Rayleigh numbers (Ra > $2 \times 10^{8}$). This finding agrees with prior results [47] that show a higher Nusselt number at some porous layer height ratio greater than zero.

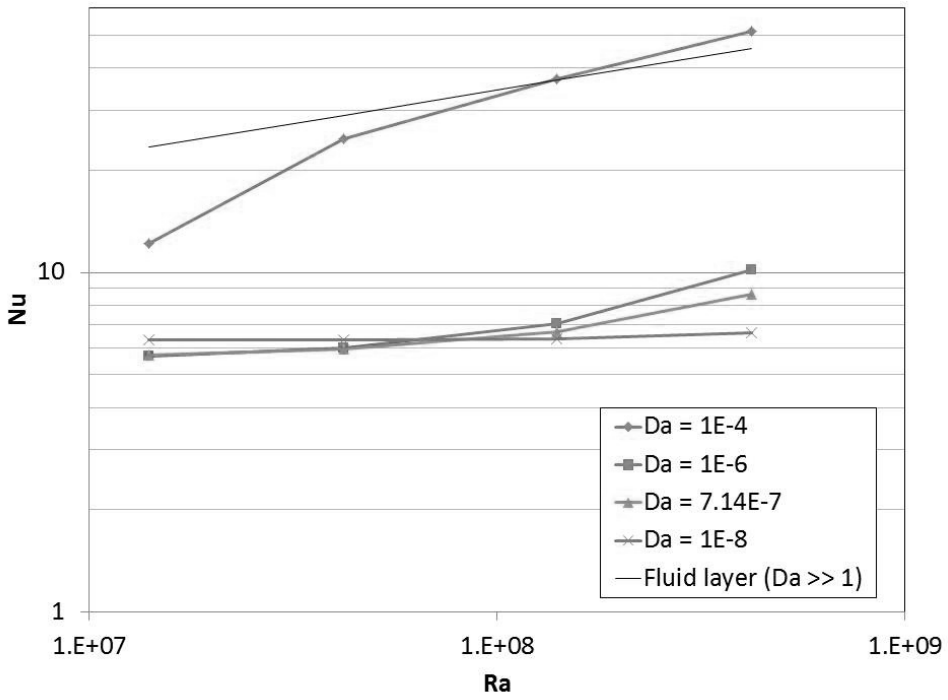


Figure 52. Effect of Darcy number variation on overall Nusselt number results ($\eta = 0.9$, Pe = 30).

### 4.3.5 Porous layer height variation

As previously discussed, mixed convection with a varying porous layer height has not been numerically or experimentally addressed in the literature. The following section explores the effects of varying the porous layer height ratio from $\eta = 0$ to 1. Furthermore, the impact of the porous height ratio on the critical Rayleigh number is explored as well as the impact on the critical Peclet number. A critical porous height ratio is also discovered and explored.

#### 4.3.5.1 Critical Rayleigh number

The critical Rayleigh-Darcy number for a full porous layer was shown to be approximately 40 in the preceding sections. The critical Rayleigh number in a fluid layer is 1708, and with a Darcy number (based on the total height) of $\sim 10^{-6}$, the critical Rayleigh-Darcy number of a fluid layer would be approximately 0.0018, which was exceeded for all runs in the present mixed convection study that contain a pure fluid portion ($\eta < 1$). Although there is a well-established critical Rayleigh number for a full

Table 6. Rayleigh number of individual sub-layers across range of η (Da = 7.14E-7, RaDa = 1).

| Porous height ratio | Rayleigh-Darcy number of the porous layer $\mathrm{RaDa} = \frac{\mathrm{Kg\beta h_p \Delta T}}{\alpha\nu}$ | Rayleigh number of the fluid layer $\mathrm{Ra} = \frac{\mathrm{g\beta\left(H - h_p\right)^3 \Delta T}}{\alpha\nu}$ |
|---|---|---|
| η = 0 | N/A | $1.4 \times 10^6$ |
| η = 0.25 | 0.25 | $5.9 \times 10^5$ |
| η = 0.5 | 0.5 | $1.8 \times 10^5$ |
| η = 0.75 | 0.75 | $2.2 \times 10^4$ |
| η = 0.9 | 0.9 | $1.4 \times 10^3$ |
| η = 1 | 1 | N/A |

porous layer and for a full fluid layer, there is no critical Rayleigh number for a varying porous layer height.

To better understand the conduction in this two-layer system, Rayleigh numbers for each sub-layer were calculated individually, based on the height of that layer. All values were calculated with the same ΔT as for RaDa = 1.

As can be seen in Table 6, the Rayleigh-Darcy number of the porous layer simply scales linearly with the porous height, but the Rayleigh number of the fluid layer scales with the cube of the fluid layer height. Also, with a Darcy number on the order of $10^{-6}$, there is a substantial difference between the Rayleigh-Darcy number of the porous layer and the Rayleigh number of the fluid layer with respect to their critical values. This indicates that the heat transfer regime for each layer will often be substantially different (conduction-dominated, laminar convection, turbulent convection, etc). Interestingly, at a Rayleigh-Darcy number of one, the Rayleigh number for the pure fluid layer at a porous height ratio of 0.9 is less than the critical value. This is the only case where the critical Rayleigh number in the pure fluid region is not exceeded. In addition, the ΔT in the Rayleigh number would need to be updated as well, but the value must be determined by looking at the plots of the isotherms from the numerical results.

Table 7 shows the updated Rayleigh number values.

Table 7. Modified Rayleigh Number for natural convection runs.

| | Rayleigh-Darcy number of the porous layer $\mathrm{RaDa} = \frac{\mathrm{Kg}\beta \mathrm{h_p} \Delta \mathrm{T}}{\alpha \nu}$ | | | | Rayleigh number of the fluid layer $\mathrm{Ra} = \frac{\mathrm{g}\beta \left(\mathrm{H} - \mathrm{h_p}\right)^3 \Delta \mathrm{T_f}}{\alpha \nu}$ | | | |
|---|---|---|---|---|---|---|---|---|
| $\eta$ | RaDa = 1 | 10 | 100 | 1000 | 1 | 10 | 100 | 1000 |
| 0 | | | | | $1.4 \times 10^6$ | $1.4 \times 10^7$ | $1.4 \times 10^8$ | $1.4 \times 10^9$ |
| 0.25 | 0.25 | 2.5 | 25 | 250 | $3.0 \times 10^5$ | $2.4 \times 10^6$ | $1.8 \times 10^7$ | $1.5 \times 10^8$ |
| 0.5 | 0.5 | 5 | 50 | 500 | $7.0 \times 10^4$ | $4.4 \times 10^5$ | $3.5 \times 10^6$ | $3.5 \times 10^7$ |
| 0.75 | 0.75 | 7.5 | 75 | 750 | $6.6 \times 10^3$ | $4.8 \times 10^4$ | $3.9 \times 10^5$ | $3.3 \times 10^6$ |
| 0.9 | 0.9 | 9 | 90 | 900 | $1.4 \times 10^2$ | $3.2 \times 10^3$ | $2.9 \times 10^4$ | $2.5 \times 10^5$ |
| 1 | 1 | 10 | 100 | 1000 | | | | |

These results further confirm that the critical Rayleigh number in the pure fluid layer is exceeded for all porous layer height values below $\eta = 0.9$. At $\eta = 0.9$, the critical Rayleigh number is exceeded somewhere between RaDa = 1 and 10.

As can be seen in Figure 53, the isotherms are those of pure conduction, with no plume formation in the fluid layer at the top. Increasing the temperature so that the Rayleigh number exceeds the critical value in the pure fluid region causes the onset of convection to occur, which can be seen in the narrowing of the plume in Figure 54. The streamlines for these two cases also indicate that more significant recirculation has started. First, the streamline values have increased by nearly a factor of 50, and second, the streamlines are much more narrowly focused.

Based on the above findings, the results indicate that the critical Rayleigh number that predicts the onset of convection is still applicable for a two-layer system, provided that the Rayleigh number is calculated independently for each layer.

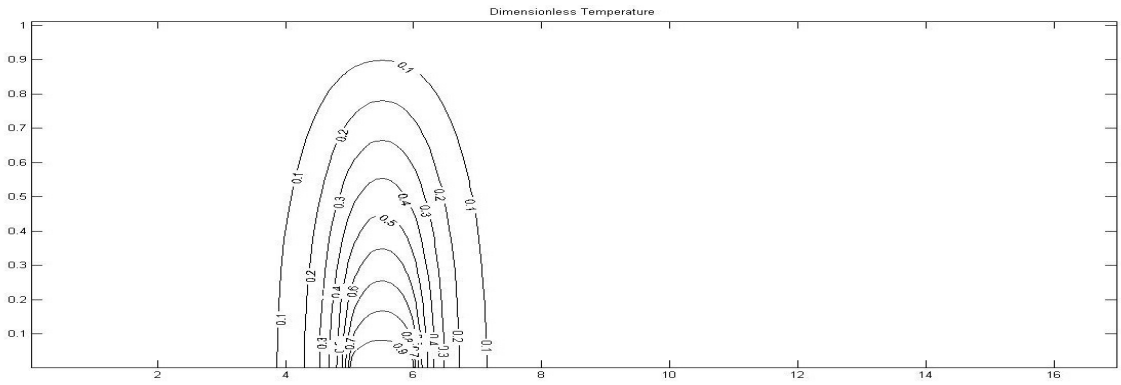


Figure 53. Isotherms for η = 0.9 and RaDa = 1 and Pe = 0.

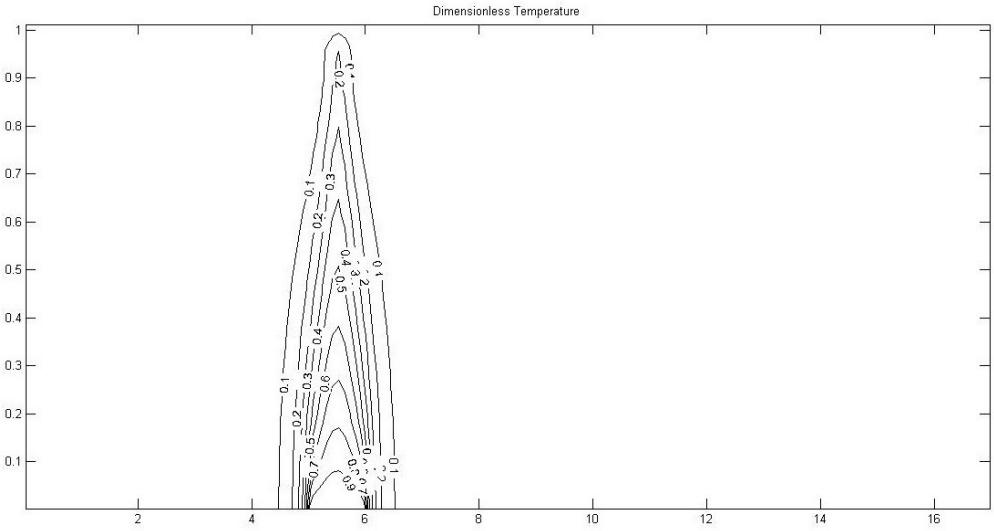


Figure 54. Isotherms for η = 0.9 and RaDa = 10 and Pe = 0.

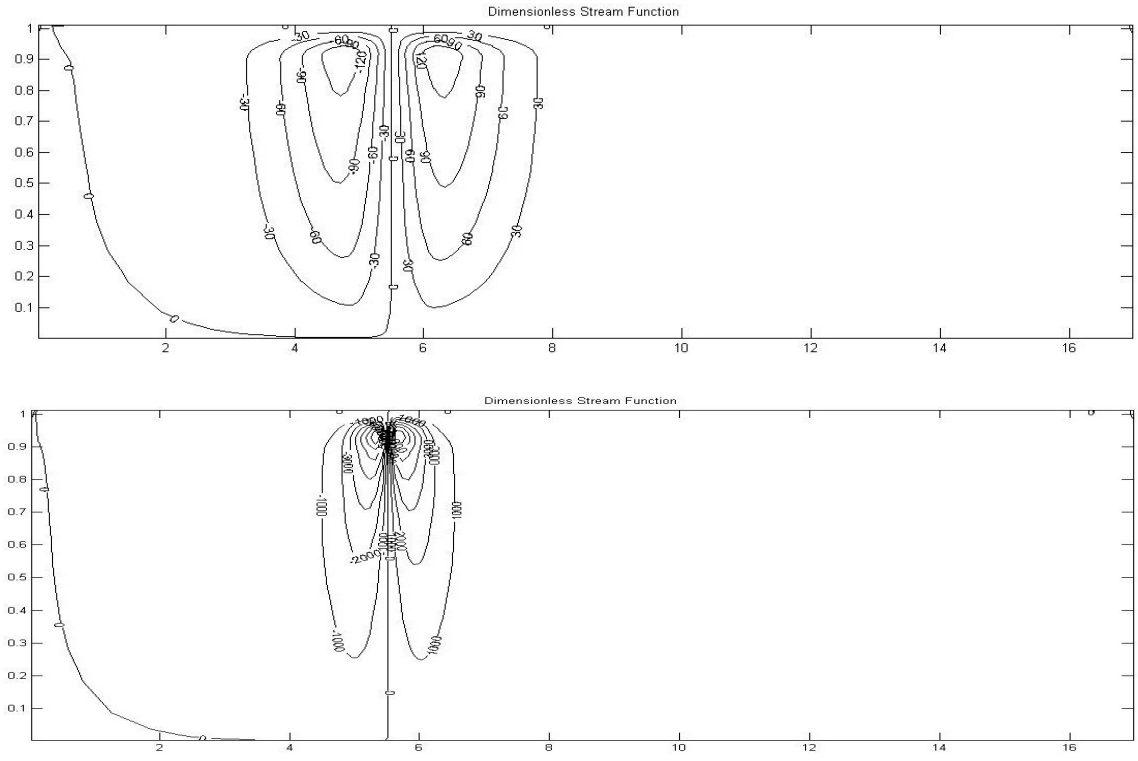


Figure 55. Dimensionless stream lines for η = 0.9, Pe = 0, and a) RaDa = 1 and b) RaDa = 10

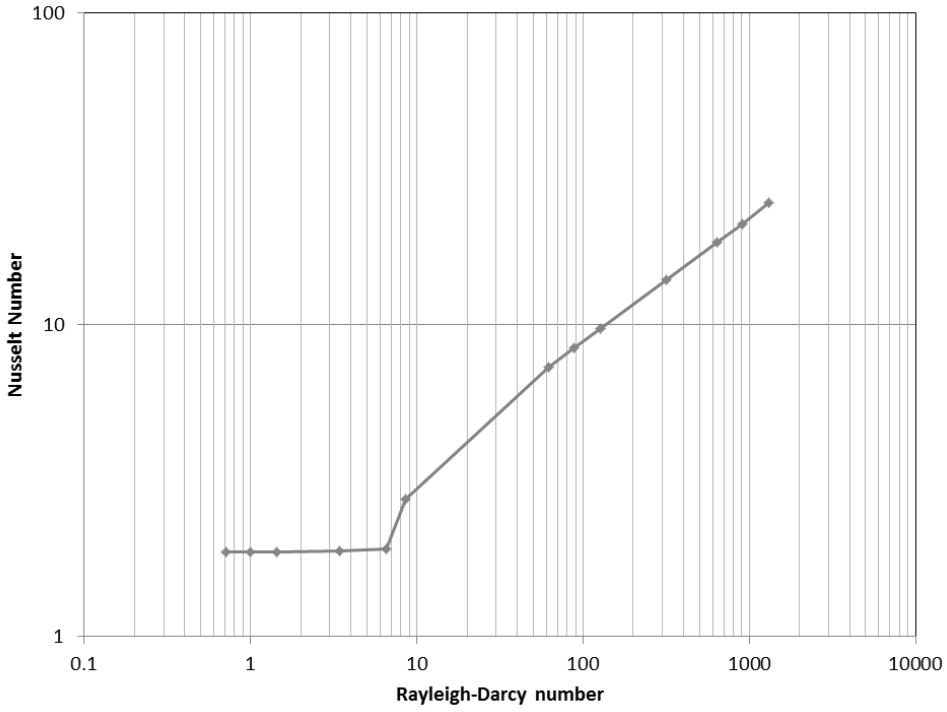


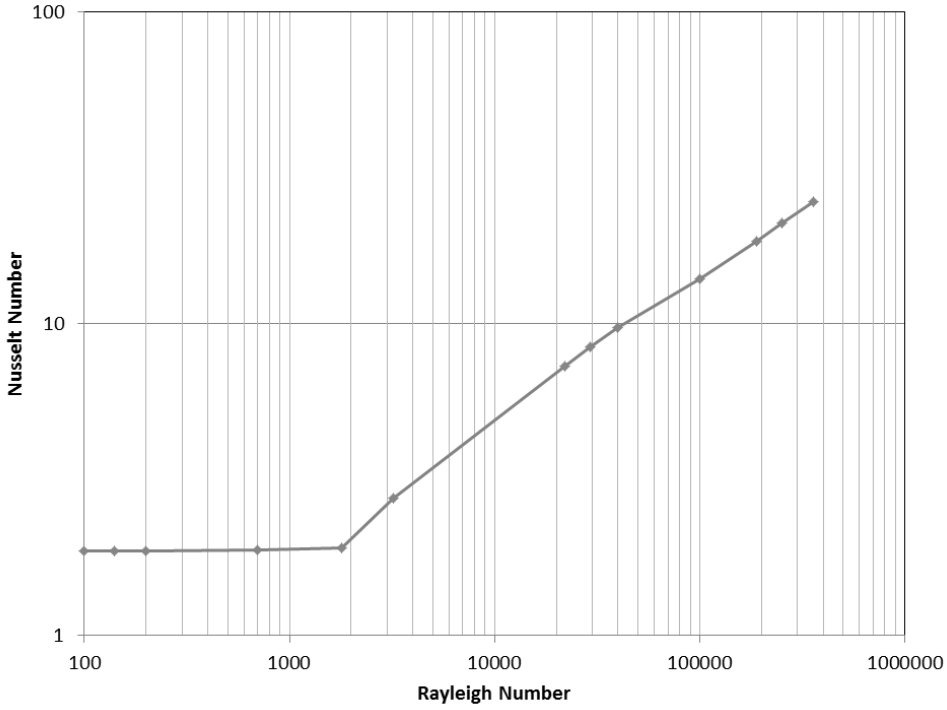


Figure 56. Critical Rayleigh number for natural convection ($\eta = 0.9$, Pe = 0).

Figure 56 shows the Nusselt/Rayleigh number relationship for the two-layer system where $\eta = 0.9$, showing that the onset of convection occurs (for the combined system) when the first critical Rayleigh number is reached. Without the pure fluid layer,

the knee in the Nusselt/Rayleigh-Darcy number curve would not be expected until approximately RaDa = 40, but a Rayleigh-Darcy number of approximately 7 in the porous layer corresponds to a Rayleigh number of approximately 1800 in the fluid layer. Therefore, the onset of convection occurs earlier than expected if looking at the Rayleigh-Darcy number but occurs exactly as expected when looking at the Rayleigh number of the fluid layer.

In conclusion, earlier findings regarding the onset of convection are still valid in a two-layer system, provided that the Rayleigh number is calculated for each layer individually, and the onset of convection for the entire system occurs when the Rayleigh number of any layer exceeds the critical value for that domain.

#### 4.3.5.2 Critical Peclet number

Several prior authors observed the critical Peclet number [40,41,59], where increasing the Peclet number up to the critical value actually decreases the heat transfer, and increasing the Peclet number beyond the critical value then increases the heat transfer as would be expected. This behavior is caused by the forced flow interfering with/disrupting the natural convection plume flow at low levels of cross flow. The critical Peclet number was observed numerically in the present study. The value of the critical Peclet number was shown to increase with the Rayleigh number and was shown to decrease with the porous layer height ratio.

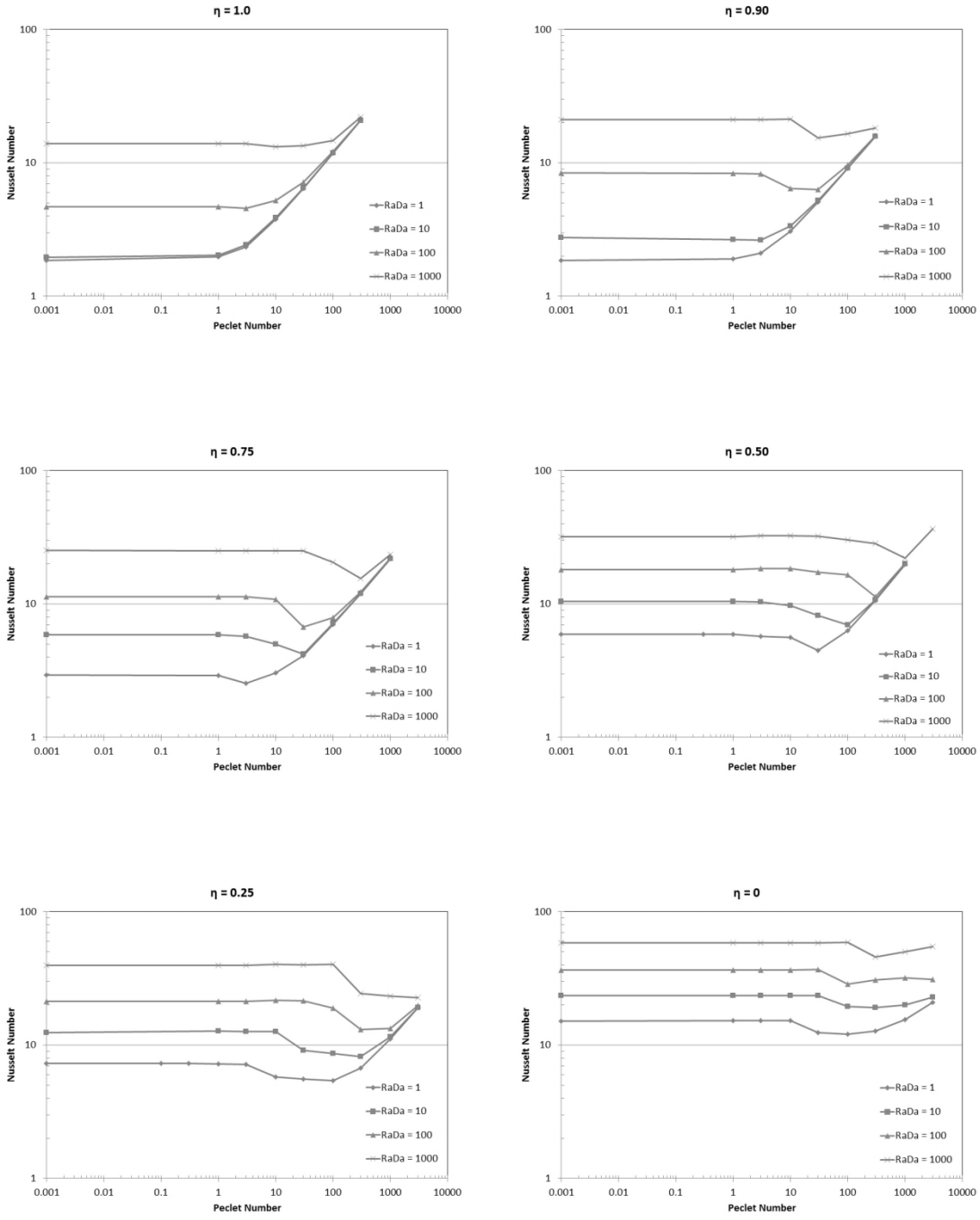


Figure 57. Nusselt/Rayleigh/Peclet relationship across range of porous layer height ratio from η = 0 to 1.

The current results match existing results where existing results are available at η = 1, and the new results for the varying porous layer height follow expected behavior. At low Rayleigh number for a full porous layer, no critical Peclet number was observed.

This is expected, because below the critical Rayleigh number there is no bulk motion of the fluid and heat transfer is due to conduction only, therefore, cross flow cannot disturb any natural convection recirculation because there isn't any recirculation to disturb. The critical Rayleigh-Darcy number of a porous layer is approximately 40, and it can be seen that the curves in Figure 57 for $\eta = 1$ and for Rayleigh-Darcy numbers below 40 do not have a critical Peclet number and the curves for Rayleigh numbers above 40 do show a critical Peclet number.

In addition, for $\eta = 0.9$, there is no observed critical Peclet number when RaDa = 1 but there is a critical Peclet number at RaDa = 10 and above (although it is a very small effect at RaDa = 10). There is also a critical Peclet number at all lower $\eta$ values considered. This also matches the discussion in the preceding section regarding the critical Rayleigh number for a two-layer system – when the Rayleigh number in one of the two layers exceeds the critical Rayleigh number for that domain then there is convective motion in the entire system, and when there is convective motion, that convective motion can be disrupted by cross flow, impeding the heat transfer and resulting in a critical Peclet number.

Two additional observations can be made from Figure 57. First, that the region over which the heat transfer is impeded becomes noticeably wider at lower values of $\eta$. For $\eta$ values ranging from 0.5 to 1, the decrease in heat transfer occurs over 1-2 orders of magnitude, but for $\eta$ values below 0.5, the decrease in heat transfer occurs over 3-4 orders of magnitude. Second, the critical Peclet number increases as the porous layer height decreases. Both of these observations are explained by the same physical mechanism. The Rayleigh number in the fluid layer increases with the cube of the fluid layer height, which produces much stronger convective flows for lower values of $\eta$ at a given $\Delta T$. As would be expected, stronger natural convection flows require stronger forced convection flows to disturb them and even stronger forced convection flows to drown them out.

Curves for all Rayleigh numbers eventually collapse onto the same curve at high enough Peclet numbers, although this happens at higher Peclet numbers as the porous layer height decreases. This transition from natural convection to forced convection is further explored in the following section.

4.3.5.3 Transition from natural to forced convection

Clearly, at very low Peclet number (Pe < 1 for the above cases), the cross flow has no effect on the overall heat transfer of the system. Also, at very high Peclet numbers, the Rayleigh number has no effect on the overall heat transfer of the system. Low Peclet number is considered the natural convection regime and high Peclet number is considered the forced convection regime. The intermediate region is the mixed convection regime.

In the natural convection regime, bulk motion of the fluid is dominated by recirculating natural convection flows. In the forced convection regime, bulk motion of the fluid is dominated by cross flow. In the mixed convection regime there is a combination of both flow patterns. Figures 58-63 show all three flow regimes: natural, mixed, and forced convection.

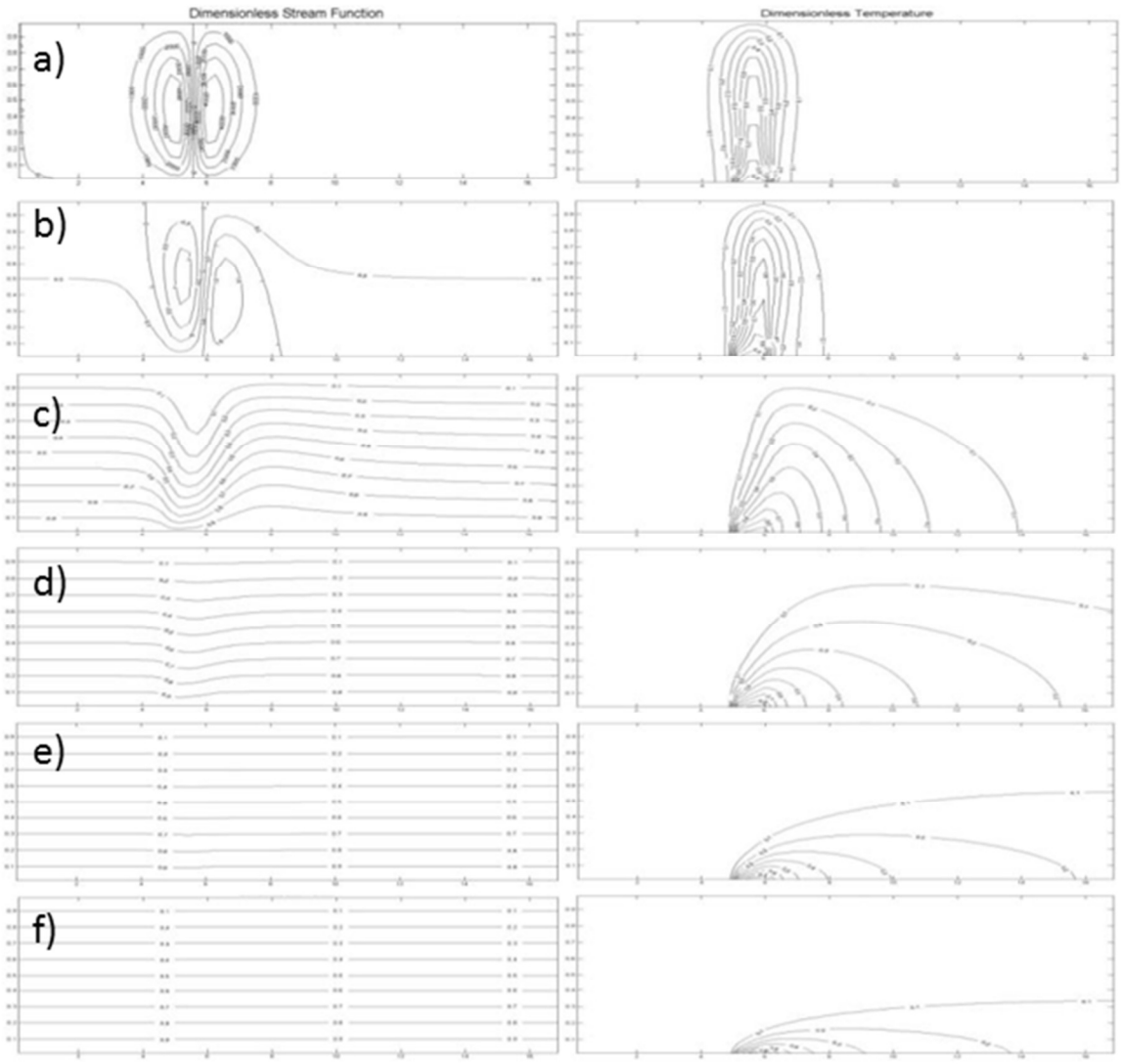


Figure 58. Streamlines and isotherms for $\eta = 1$, Rayleigh-Darcy number of 100, and Peclet number of a) 0, b) 3, c) 10, d) 30, e) 100, and f) 300.

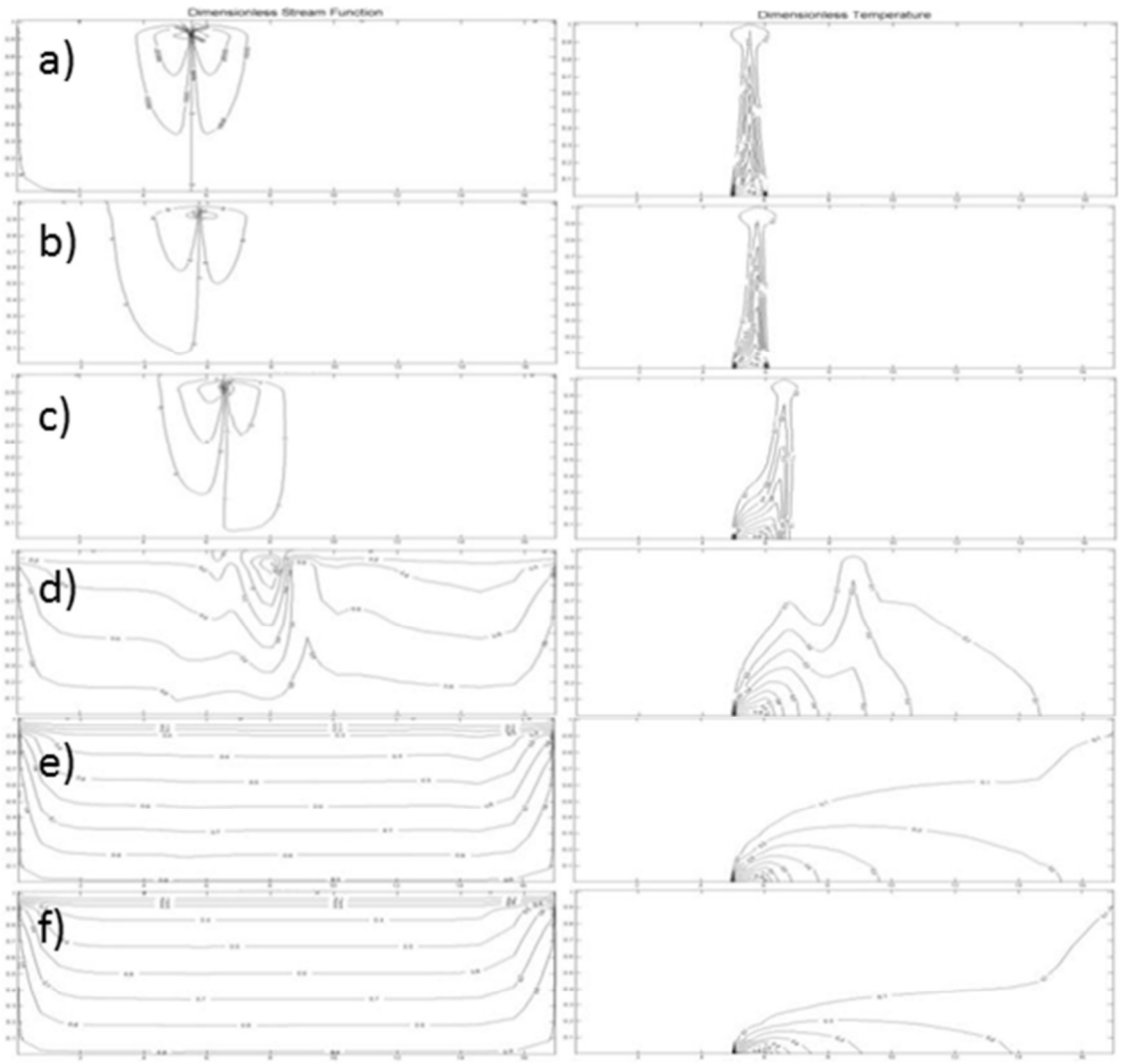


Figure 59. Streamlines and isotherms for $\eta = 0.9$, Rayleigh-Darcy number of 100, and Peclet number of a) 0, b) 3, c) 10, d) 30, e) 100, and f) 300.

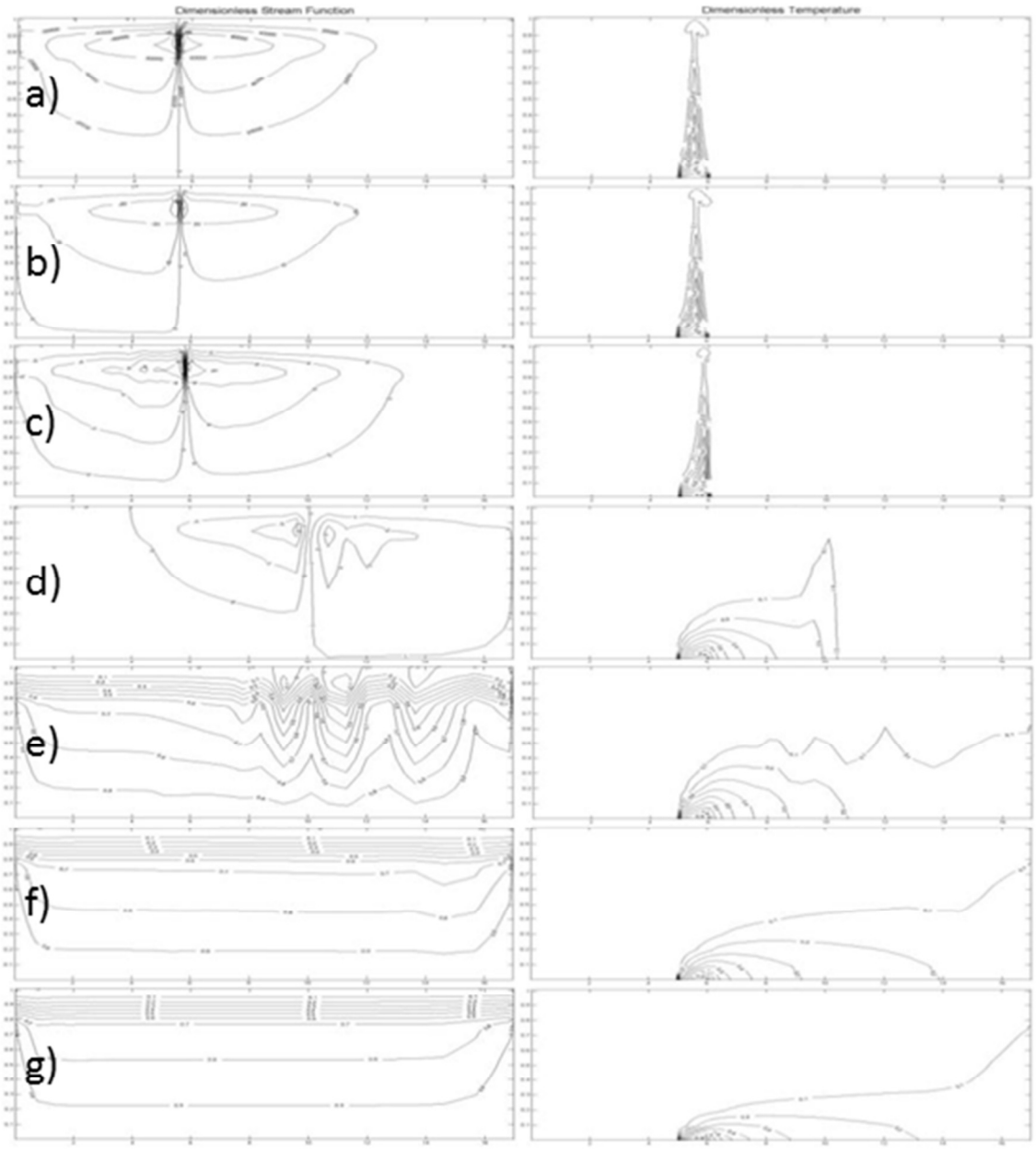


Figure 60. Streamlines and isotherms for $\eta = 0.75$, Rayleigh-Darcy number of 100, and Peclet number of a) 0, b) 3, c) 10, d) 30, e) 100, f) 300, and g) 1000.

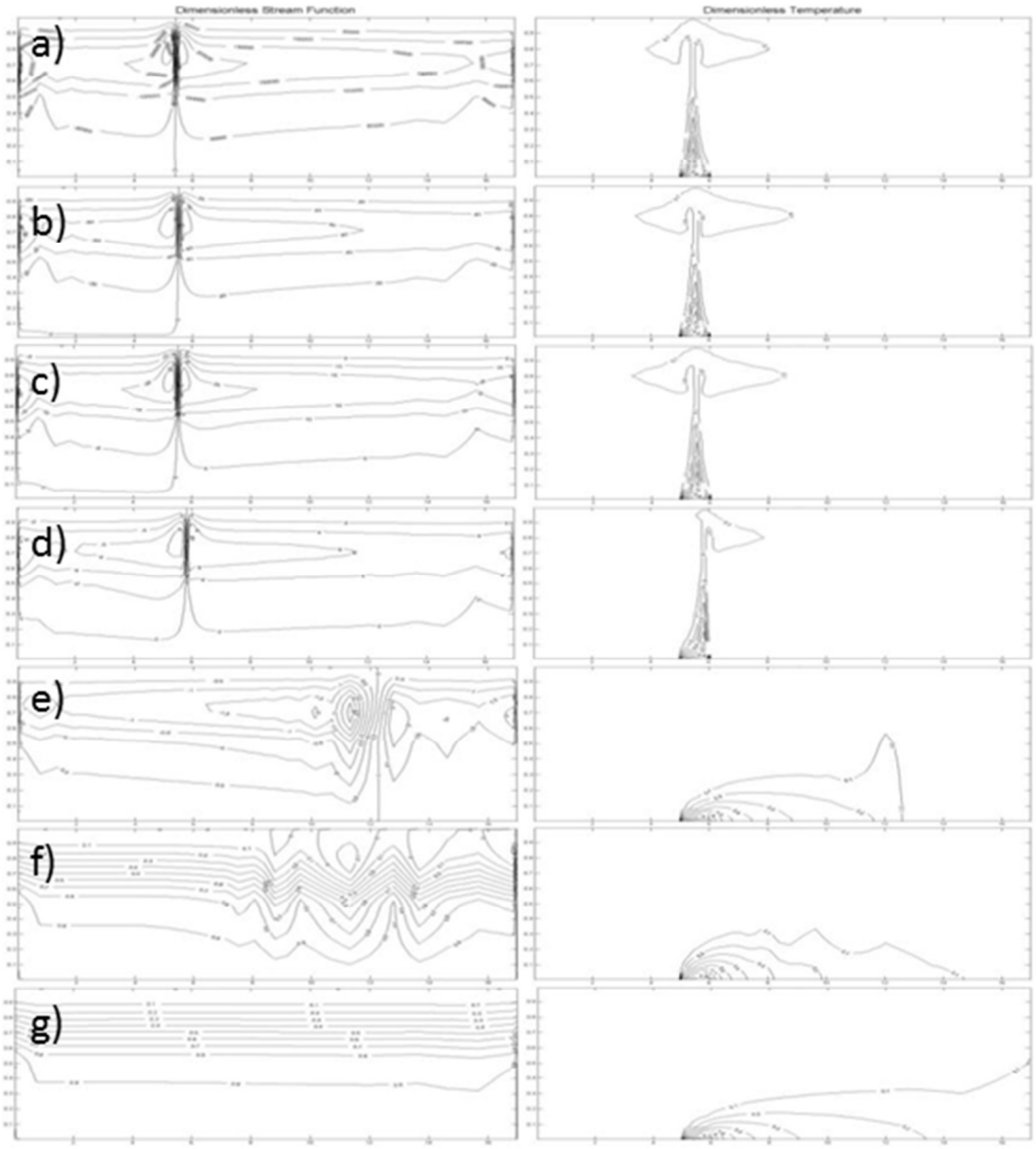


Figure 61. Streamlines and isotherms for $\eta = 0.5$, Rayleigh-Darcy number of 100, and Peclet number of a) 0, b) 3, c) 10, d) 30, e) 100, f) 300, and g) 1000.

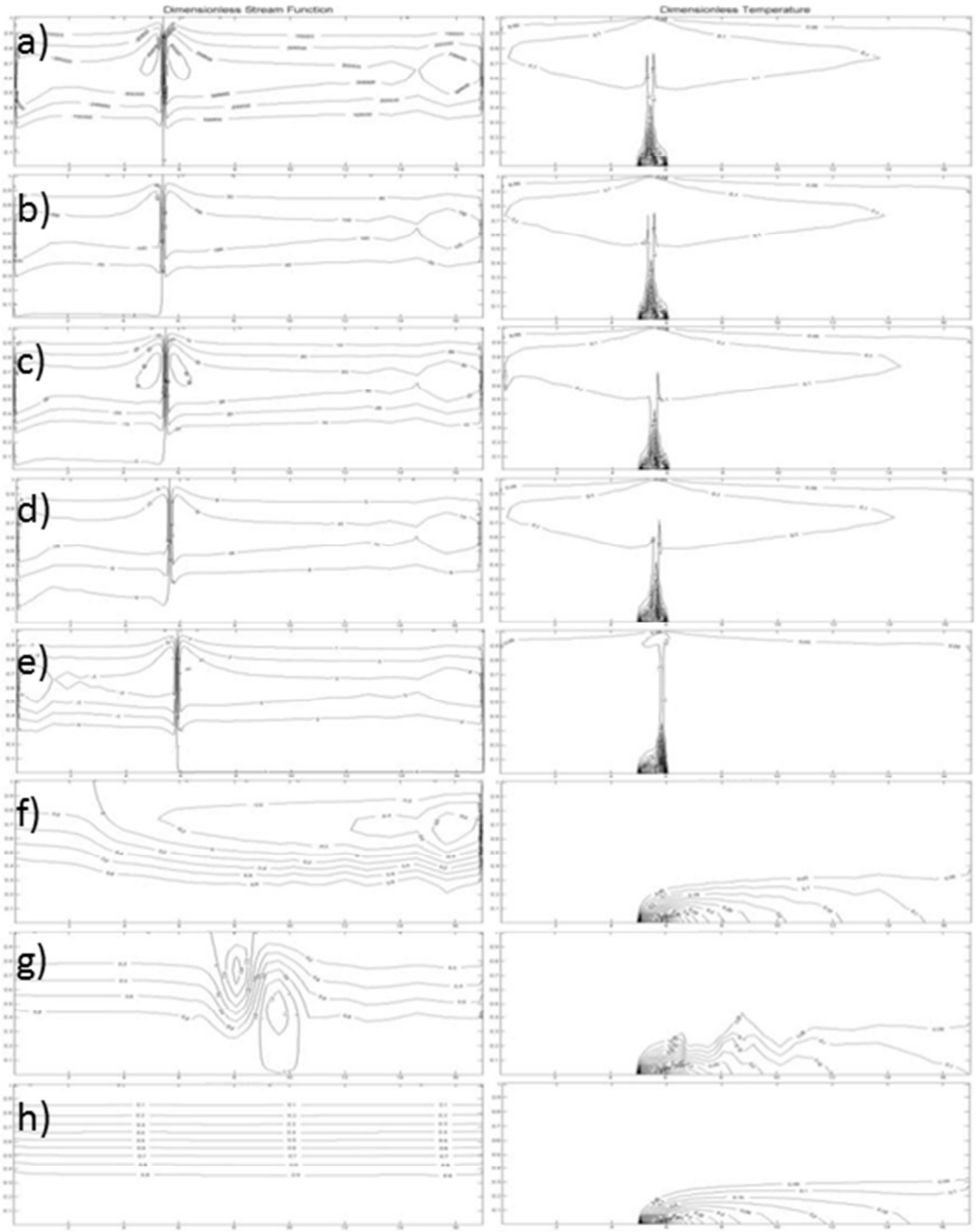


Figure 62. Streamlines and isotherms for $\eta = 0.25$, Rayleigh-Darcy number of 100, and Peclet number of a) 0, b) 3, c) 10, d) 30, e) 100, f) 300, g) 1000, and h) 3000.

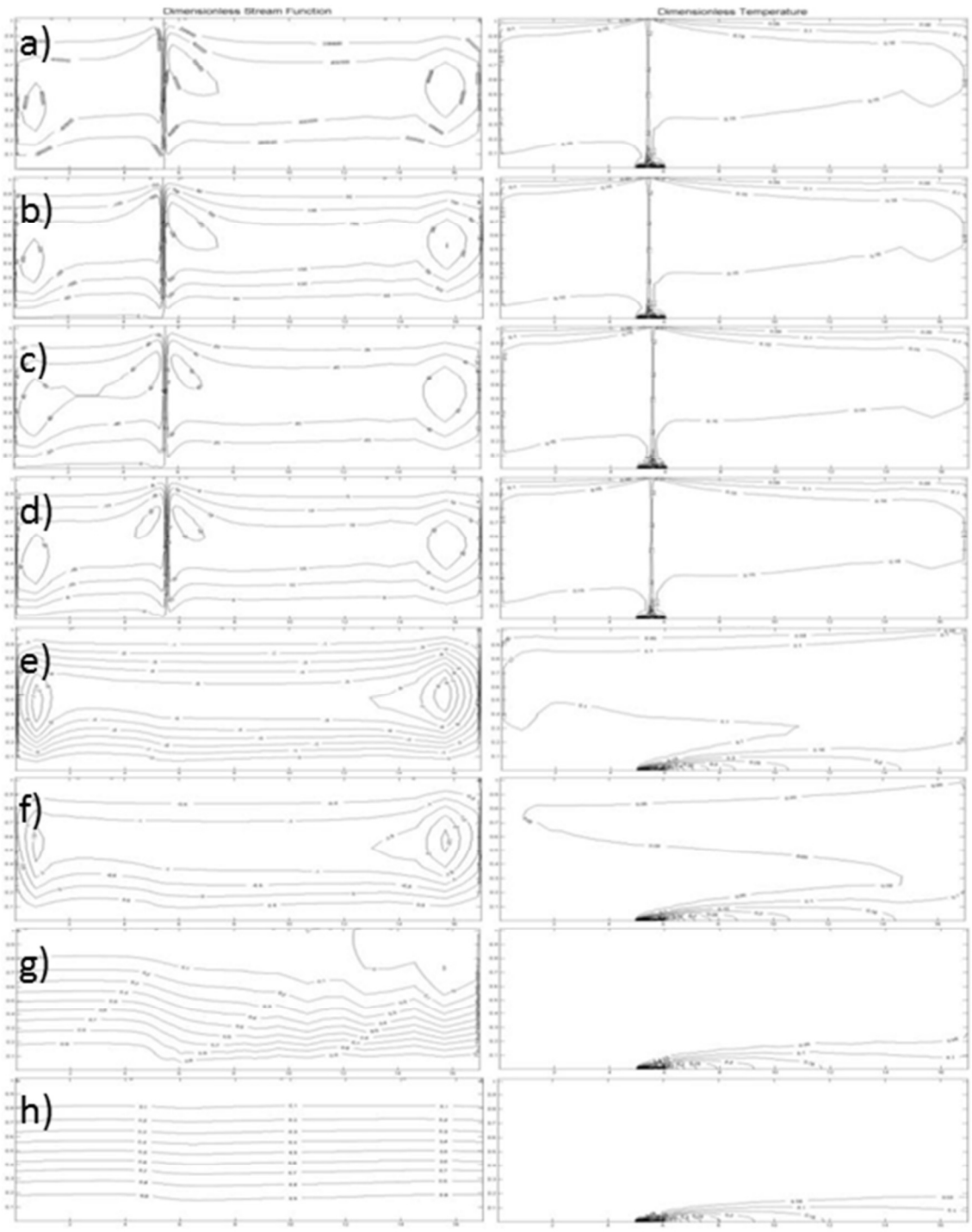


Figure 63. Streamlines and isotherms for $\eta = 0$, Rayleigh-Darcy number of 100, and Peclet number of a) 0, b) 3, c) 10, d) 30, e) 100, f) 300, g) 1000, and h) 3000.

Keep in mind that the aspect ratio is 17:1 for the problem domain of the present study and the above graphs are not to scale.

As can be seen in Figure 58-Figure 63, the streamlines in the natural convection regime follow a standard plume pattern, with the strength/focus of the plume increasing with a decreasing porous layer height. Also, the streamlines in the forced convection regime are essentially horizontal, with no visible effect of the buoyant flow. Interestingly, the mixed convection region shows both characteristics. Figure 58b, Figure 59d, and Figure 62f show this effect quite well, where the recirculation plume still forms, but the cross-flow is clearly visible. Keep in mind that the cross flow is present for all cases, but at low Peclet number, the magnitude of the cross flow is negligible and cannot be seen on the above graphs. This intermediate recirculation pattern occurs for every Rayleigh number and porous layer height, provided there is sufficient resolution in the Peclet number to capture it.

Another interesting result can be seen in the large-scale recirculation flow that can occur in the pure fluid region. At $\eta = 1$, the recirculation occurs throughout the entire domain, but due to the highly viscous, restrictive nature of the porous medium, the flow does not penetrate very far in the x-direction. At $\eta = 0.9$, the recirculation is focused in the small fluid layer and still does not spread very far in the x-direction, but because that fluid layer is still relatively small, significant recirculation flow can be seen penetrating into the fluid layer. By $\eta = 0.75$, the recirculation flow can be seen across much of the length of the chamber in the x-direction. The recirculation flow is still shown to penetrate into the porous layer. At $\eta = 0.5$, 0.25, and 0, the recirculation flow collides with the inlet and outlet of the problem domain, causing large-scale recirculation due to the side walls. At this point, almost all of the recirculation flow occurs in the fluid layer and not in the porous layer.

#### 4.3.5.3 Plume flow

The isotherms also show interesting effects in the thermal plume. With a full porous layer, the plume is fairly wide, but as soon as even a small fluid layer is included above the porous domain the characteristic of the thermal plume drastically changes, becoming significantly narrower and more focused. The plume becomes more and more narrow as the porous layer gets smaller. The acceleration of the flow due to buoyancy is

much stronger in the pure fluid region than it is in the porous region, so as soon as the temperature penetrates into the pure fluid layer, the flow accelerates, drawing flow from the fluid region and from the porous layer. This acts like a heat sink at the upper edge of the porous region, causing the heat to more easily flow upwards, limiting the time to conduct outward in the x-direction.

The effect of cross flow also produces interesting results in the isotherms. As the Peclet number increases, the thermal plume can clearly be seen to shift downstream. This happens only slightly, at first, not changing the character of the plume. Figure 59a-c, Figure 60a-c, Figure 61a-d, Figure 62a-e, and Figure 63a-d all show this effect. However, at higher Peclet number, the point where the thermal plume exits the porous layer is shifted downstream, which allows for the heat to spread out via conduction significantly more so that the strength of the plume is reduced by the time it reaches the interface between the porous and fluid layers. Figure 59d, Figure 60d, and Figure 61e all show this effect. When the Peclet number gets large enough, the thermal plume exits the problem domain before it has a chance to emerge from the porous layer, or for $\eta = 0$, before it has a chance to accelerate upward into a thermal plume. In Figure 63e, f, and g, the thermal plume "takes off" at the rear of the chamber, and by Figure 63h, the thermal energy all exits the chamber before it has time to accelerate upward.

#### 4.3.5.4 Critical η-value

As with the Peclet number, intuitively, the porous media restricts the flow and would therefore be expected to reduce the overall heat transfer of the system. Although this is generally accurate, it is not entirely true for all cases, and a critical η-value is observed where the Nusselt number is a minimum.

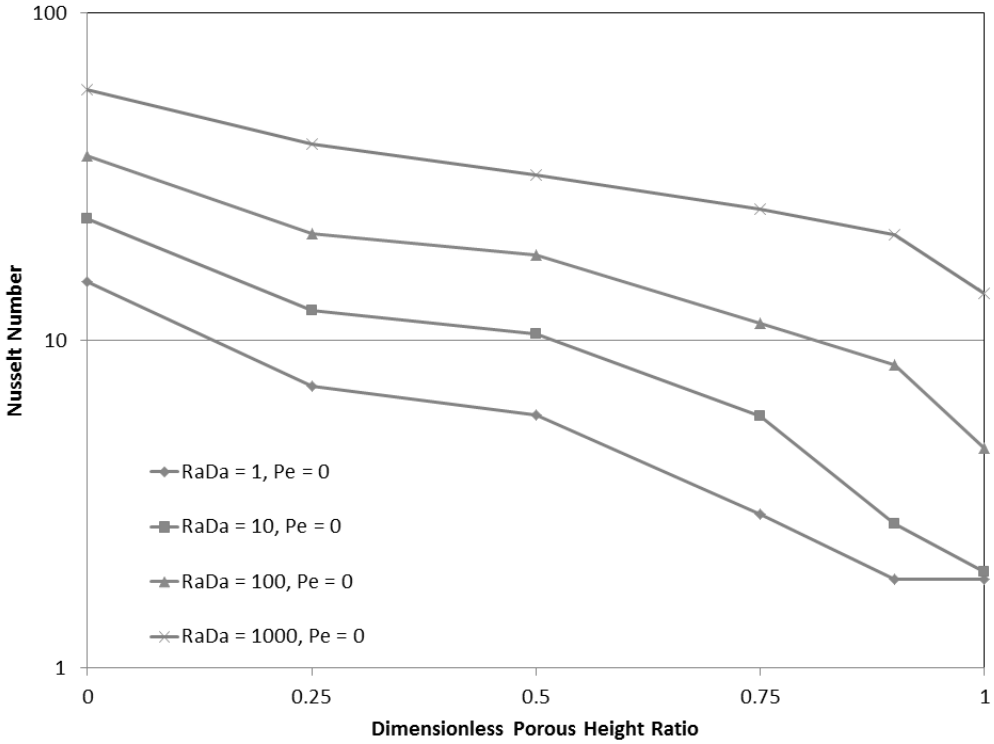


Figure 64. Nusselt number verses η for Pe = 0.

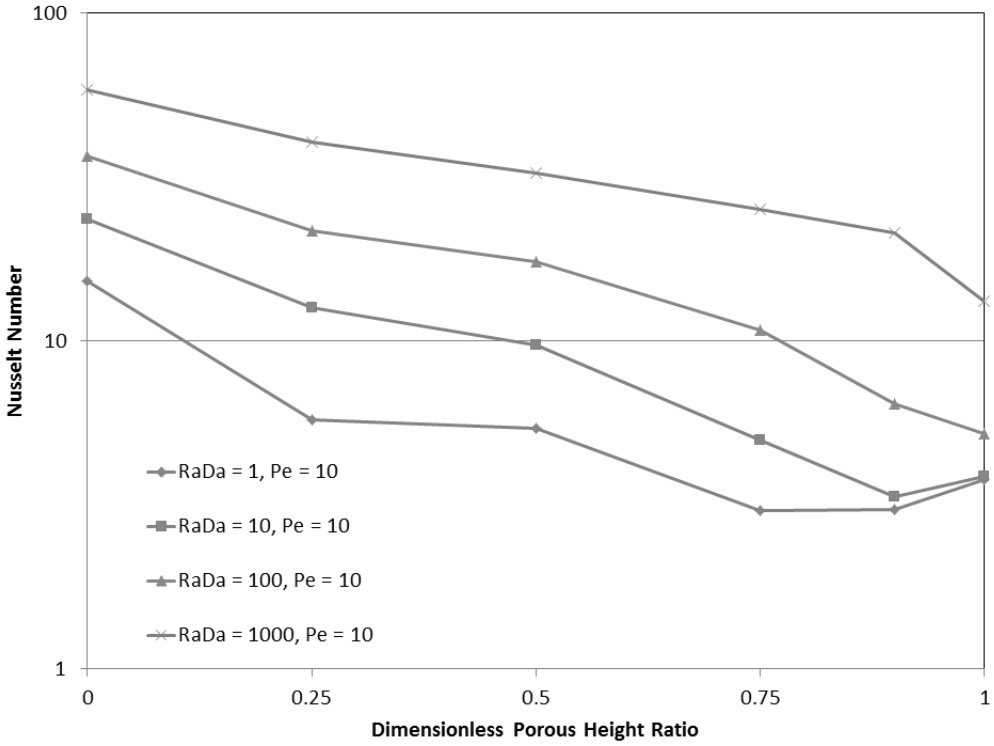


Figure 65. Nusselt number verses η for Pe = 10.

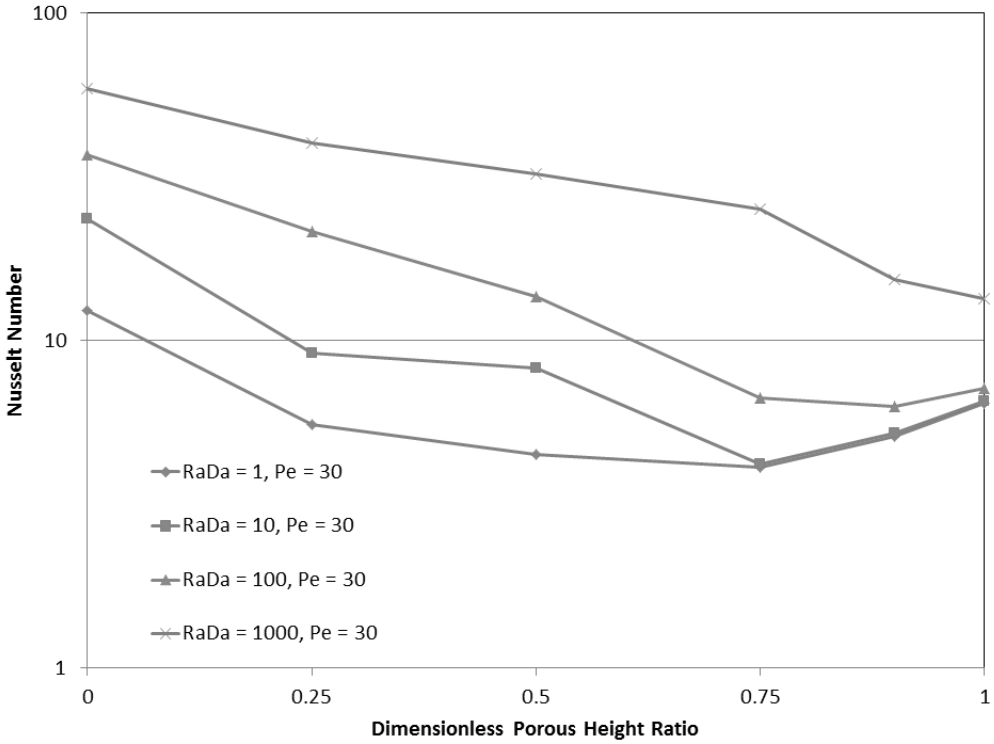


Figure 66. Nusselt number verses η for Pe = 30.

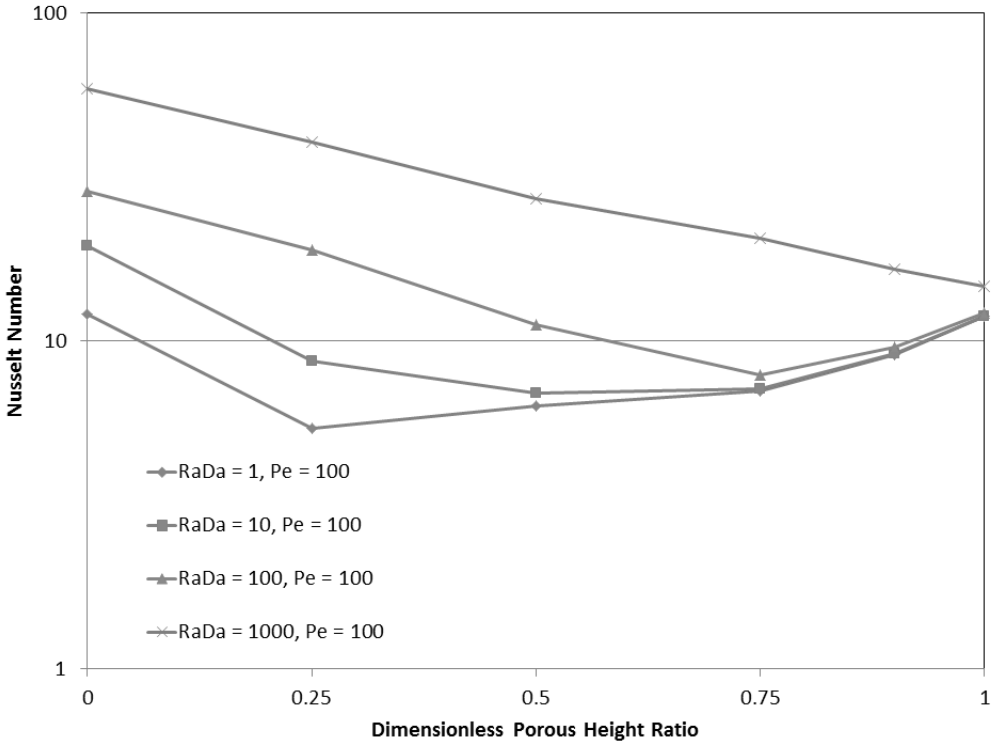


Figure 67. Nusselt number verses η for Pe = 100.

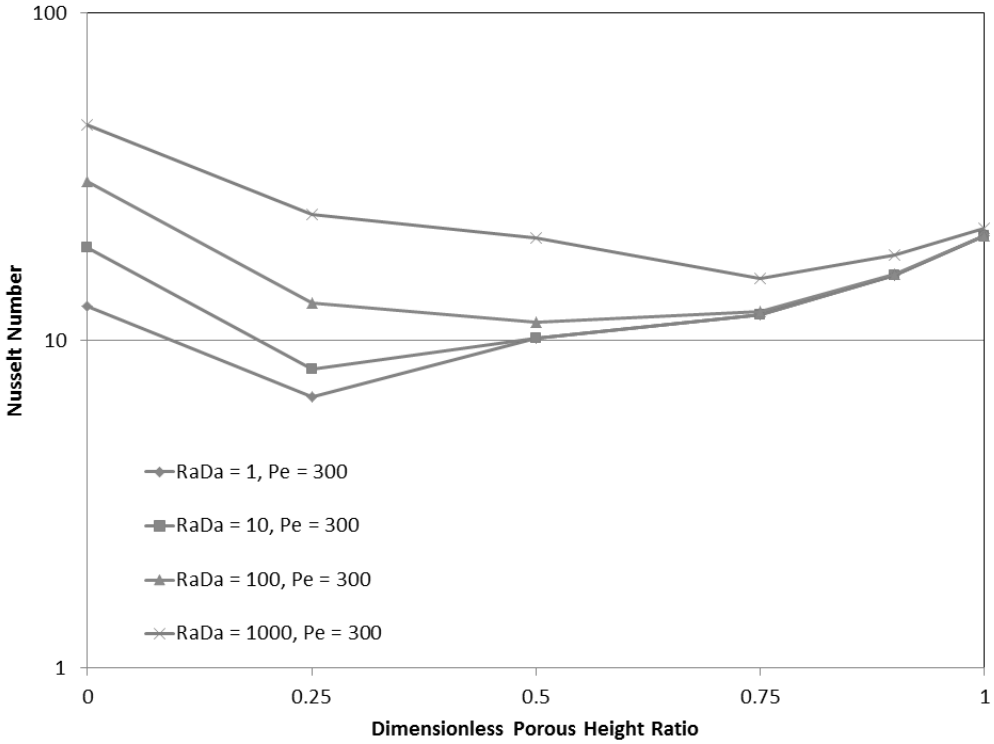


Figure 68. Nusselt number verses η for Pe = 300.

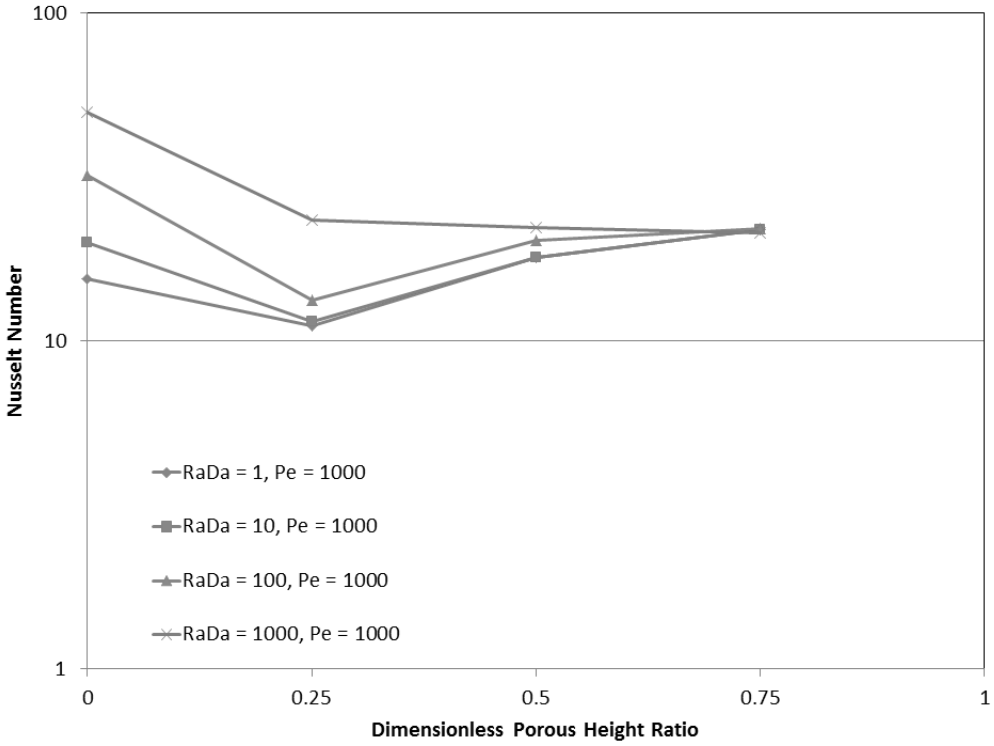


Figure 69. Nusselt number verses η for Pe = 1000.

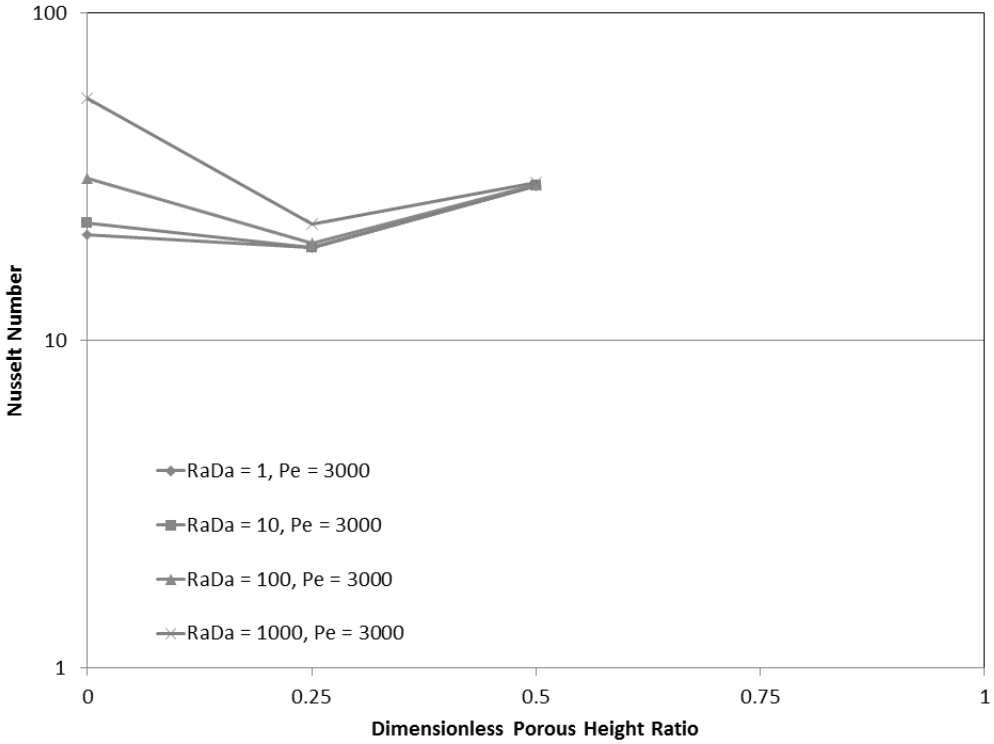


Figure 70. Nusselt number verses η for Pe = 3000.

Figure 64-Figure 70 show some interesting and unexpected behavior. For the natural convection case (Pe = 0), the heat transfer is inversely proportional to the height of the porous layer for all cases. Although this trend is generally true at higher Peclet number, it is not fully true and a critical η value is seen on certain curves where the heat transfer is a minimum at some intermediate value of η. At Pe = 10, it can be seen that at RaDa = 1 and 10, the Nusselt number is a minimum at η = 0.9 rather than η = 1. Although this was unexpected, upon further consideration, this behavior can be explained. The trends in the critical η-value can be seen in Figure 64-Figure 70. As the Peclet number increases, the critical η-value decreases, and as the Rayleigh-Darcy number increases, the critical η-value increases.

At high enough Peclet numbers, it can be seen that all the Rayleigh-Darcy number curves fall onto the same line. However, the Peclet number at which this occurs varies inversely with the porous layer height. At Pe = 300, all the RaDa curves merge at η = 1, at Pe = 1000, this occurs at η = 0.75, and at Pe = 3000, this occurs at η = 0.5. Therefore, the critical η-value occurs during the transition from the natural convection regime to the

forced convection regime. What ultimately increases the Nusselt number of the system is having higher flow velocities in the vicinity of the heater. The flow velocity is determined by the amount of forced flow and by the strength of the thermal plume, both of which need to be discussed.

The Peclet number is based on the average flow rate across the entire domain, but the fraction of the flow in each layer varies widely – with a Darcy number on the order of $10^{-6}$, the flow velocity in the porous layer is several orders of magnitude lower than the flow velocity in non-porous layer. A pressure gradient ultimately drives the flow through the system. When the porous layer is large, the pressure gradient to achieve a given Peclet number must also be large, and when the porous layer is small, the pressure gradient to achieve that same Peclet number is smaller. Although it's not the only factor, the pressure gradient is a large factor in determining the velocity in the porous domain. In the simplest form of Darcy's law, the Darcy velocity is proportional to the pressure gradient. Neglecting the effects of buoyancy for a moment, the local flow velocity at the heater surface is the highest when there is no porous layer, and adding a small porous layer ($\eta = 0.25$) decreases the heat transfer in all cases. Increasing $\eta$ beyond 0.25, as discussed, increases the pressure gradient, which increases the Darcy velocity in the porous domain, which increases the heat transfer at the heater surface, increasing the Nusselt number of the system.

When the effects of buoyancy are added into the mix things get more complicated. The strength of the thermal plume increases as the porous layer height decreases for a given Rayleigh-Darcy number. When the thermal plume emerges from the porous layer it accelerates upward, drawing fluid from the porous layer with it. In addition, with a larger fluid layer the plume has a longer distance over which to accelerate and impacts the ceiling with greater momentum and causes a stronger recirculation flow, penetrating deeper into the porous domain. The flow velocity at the heater surface is increased by both of these factors, both of which increase as the porous layer height decreases. So it is a tradeoff – increasing $\eta$ increases the amount of forced flow at the heater surface but it decreases the amount of recirculating buoyant flow at the heater surface. In the forced convection regime, increasing $\eta$ increases the heat transfer. In the natural convection regime, increasing $\eta$ decreases the heat transfer.

## 4.4 Conclusions

To review, the present numerical code was shown to produce good agreement with existing results from a range of natural convection and mixed convection studies. This was done to confirm that the code is properly working and to provide more confidence in the new numerical results that the code was used to produce. New results were produced for a range of $\eta$ values and those results were analyzed and explained in detail. The critical Peclet number was confirmed and was shown to depend on the Rayleigh number and the porous layer height ratio. The critical Rayleigh number was shown to be valid for a two-layer system, provided that the Rayleigh number is calculated independently for each sub-layer and that the onset of convection occurs as soon as the critical Rayleigh number is exceeded for either layer. In addition, the streamlines and isotherms were plotted across a range of Peclet number for various $\eta$ values.

Transition flow in the mixed convection regime was shown to have characteristics of both the natural convection plume flow and the forced convection flow. The isotherms show interesting behavior as well, as the thermal plume shifts downstream and exits the porous layer in different places. The critical $\eta$ value was explored and explained in detail, showing that increasing the porous layer height increases the heat transfer of the overall system when in the forced flow regime and decreases the heat transfer when in the natural convection regime. The numerical results make sense and provide important closure to the two-layer problem.

# Chapter 5. Experimental Design and Procedure

The design of the experimental apparatus and the data collection procedure are discussed in the following sections. The Rayleigh number, Peclet number, dimensionless height ratio, dimensionless heater length, and Darcy number could all be varied. However, doing so would result in an exceedingly large number of experimental runs that would need to be conducted. Therefore, a selection of the total possible experimental runs has been conducted in order to provide a wide, but not comprehensive comparison to the numerical results produced. This chapter starts with the design of the experiment, a detailed description of the apparatus, and a description of the experimental procedure.

## 5.1 Selection of design parameters

The goal in the design of the experimental apparatus is,

1. Determine the desired range of non-dimensional numbers to test that will allow for comparison with previous studies for validation purposes and will extend the range of the knowledge base for this application
2. Maintain reasonable pumping and heating/cooling requirements
3. Minimize the expected uncertainty/error.

To determine suitable design parameters, two prior studies of mixed convection in a porous medium were considered [40,41]. Each of these studies used a long channel with a relatively small height and significant width, similar to Figure 13. The dimensions of the experimental setup for the present study must allow for a similar range of Rayleigh number, Peclet number, dimensionless heater size, porous layer height ratio, Darcy number, and Nusselt number to be investigated.

There are various parameters that restrict the range of the dimensionless numbers under consideration. The Nusselt number is determined by measuring the power dissipated from the heater and by measuring the temperature difference between the heater and the supply temperature of the fluid and using the heater length for the characteristic length.

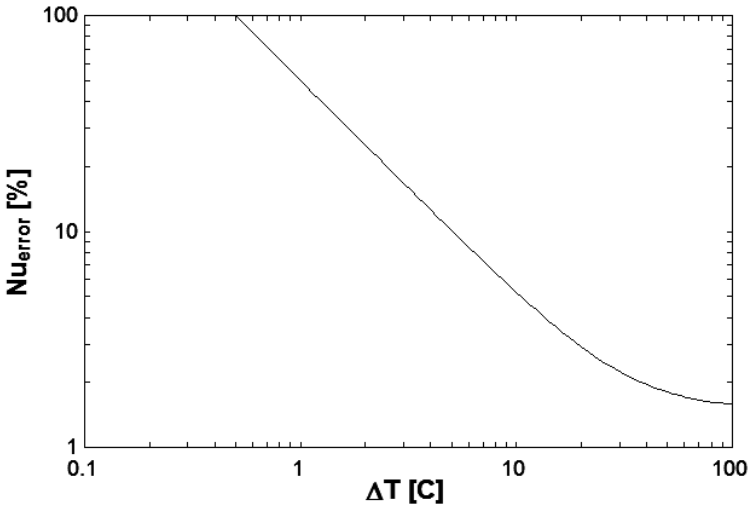


Figure 71. Nusselt Number error.

Using a standard thermocouple error of 0.5 $^{o}$C (and an error on the electrical power of 1.5%), it can be seen in Figure 71 that below about $\Delta T = 2$ $^{o}$C, the error in the Nusselt number rapidly exceeds acceptable levels. On the other end, with distilled water being used as the fluid, and with an inlet temperature of approximately 25 $^{o}$C, a value of $\Delta T = 75$ $^{o}$C will be at risk of boiling. Therefore, $\Delta T$ is bounded between ~2 $^{o}$C and ~70 $^{o}$C.

The Peclet number is essentially a measure of the bulk flow rate of the system and is restricted by total pumping needs. Initially, it was believed that the velocity in the porous layer would be more important than the velocity in the fluid layer, so the Peclet number was defined based on the Darcy velocity. Although numerical results eventually showed this to be untrue, several design decisions had already been made. In order to achieve the same range of Peclet numbers (based on the Darcy velocity), there would be significant flow in the non-porous layer. To maintain reasonable flows, the channel width and the height of the non-porous layer were kept to a minimum. For example, the dimensions of the experimental setup of a prior work [40] required a flow rate for Pe = 120 (based on the Darcy velocity) and $\eta = 1$ (for a full-porous layer) of about 0.1 GPM, but with $\eta = 0.9$, the flow requirement increases to 4.8 GPM, and with $\eta = 0.5$, the value jumps to 2600 GPM. However, if the Peclet number is defined based on the average velocity in the channel, then the flow requirements are quite small (Figure 72), thus eliminating the concern.

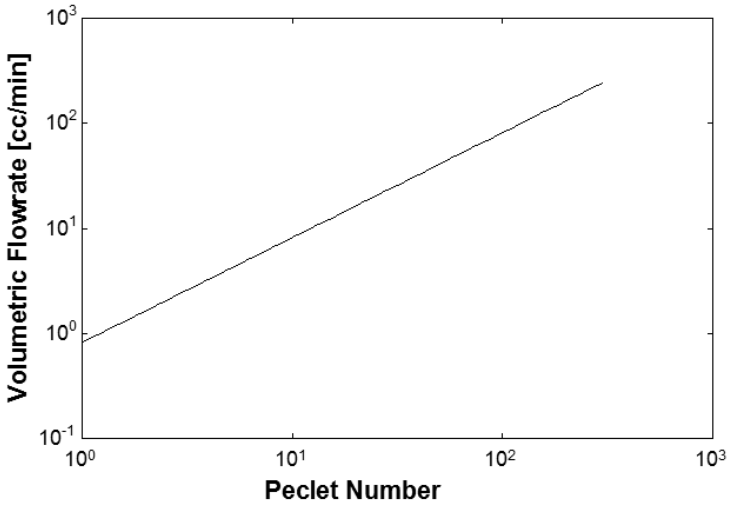


Figure 72. Flow rate verses Peclet number for present study.

The width must be wide enough to allow for two-dimensional flow assumptions to be made and was chosen to be 10 cm, and the height of the porous layer must be large enough to allow for at least six layers of the glass beads in order to neglect edge effects [60]. With 3 mm diameter glass beads being used, the minimum height of the porous layer was restricted to 1.8 cm. With a total height of 10 cm, the minimum dimensionless height ratio is therefore 0.18. Natural convection studies [1,61-63] have a range of $\eta$ values from 0 to 1, and to a resolution in $\eta$ of approximately 0.25, this same range is achieved in the present study as well ($\eta$ = 0, 0.25. 0.5, 0.75, 0.9, and 1.0).

The range of the Rayleigh number is restricted by the error on the low end, and by either flow boiling or by excessive power needs on the high end. The total power needs depend on several factors. First, the Rayleigh number in several existing experimental studies [40-41] is defined based on the heat flux, so with a given range for the Rayleigh number, the heat flux can be determined. Next, the total area is needed. This depends on the heater width, which is fixed, and the heater length ratio, which varies. The range for the dimensionless heater length ratio from prior work ranges from $\delta$ = 1 to $\delta$ = 5 [40,59] and is defined as the length of the heater in the flow direction divided by the total height of the test section.

Using the dimensions of the chamber and the desired range of values for the Rayleigh number, the total power needs can be determined. Figure 73 shows that the power required to reach a high range of Rayleigh number is quite reasonable.

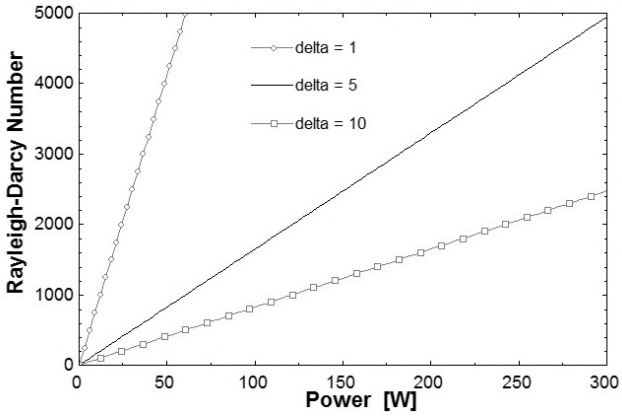


Figure 73. Rayleigh Number verses total power for various heater length ratios.

Although the power can be accurately controlled down to low levels, there is a corresponding ΔT that gets smaller and smaller as the convection coefficient increases. In order to estimate the ΔT corresponding to given Rayleigh numbers, correlations developed from a prior study [40] were used. This correlation is based on the raw data taken during mixed convection experiments with geometry similar to that of the present study and should be a good approximation,

$$\frac{\mathrm{Nu}}{\sqrt{\mathrm{Pe}}} = \left[1.274 + \left(\frac{\mathrm{RaDa}}{\mathrm{Pe}^{3/2}}\right)\right]^{0.506}. \tag{113}$$

With this relation, the Nusselt number can be calculated as a function of the Rayleigh number and Peclet number, ΔT can be calculated from the definition of the Nusselt number, and the expected error in the Nusselt number can be determined (Figure 74). It should also be noted that the dimensionless numbers in Eqn. (113) are based on the heater length, not the height of the test section. Due to the restrictions on ΔT previously discussed, Figure 74 shows that the entire range of Peclet, Rayleigh, and Nusselt number are not simultaneously achievable. For example, at low Peclet numbers, the range of Rayleigh-Darcy numbers goes down to ~5, but at high Peclet numbers, the minimum Rayleigh-Darcy number is ~50. At higher flow rates (higher Peclet number), a larger heat flux is required to maintain the same ΔT. However, the design of the current study provides a larger range of values within the bounds of acceptable error than prior work [40].

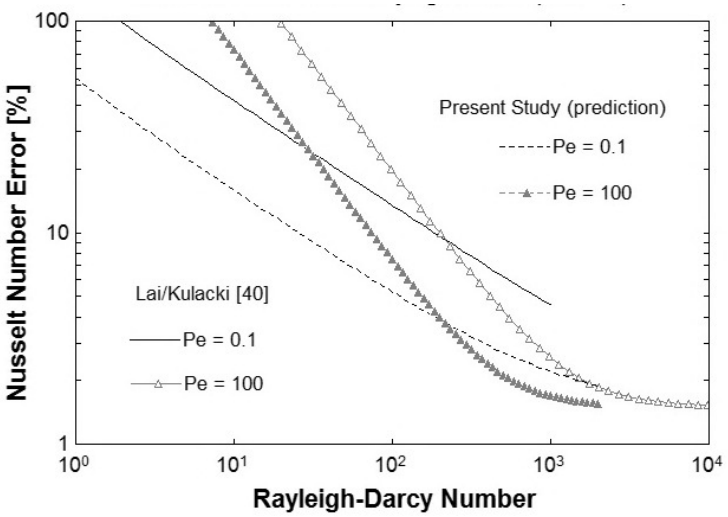


Figure 74. Comparison of uncertainty for current and prior mixed convection studies [40].

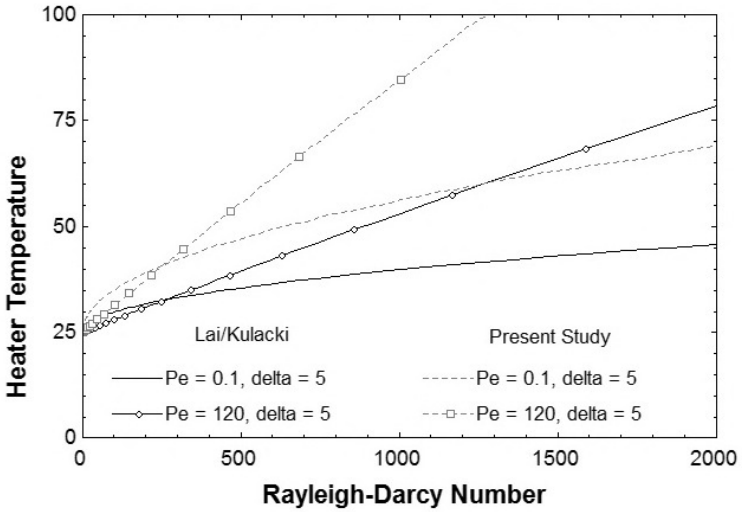


Figure 75. Upper limit on Rayleigh-Darcy number.

In addition, the upper limit of the boiling temperature of water restricts the upper range of the Nusselt number, and through the correlation in Eqn. (113), restricts the upper range of the Rayleigh-Darcy number as well. Figure 75 shows that the dimensions of the present study do not restrict the Rayleigh-Darcy number below the desired maximum value of 1000.

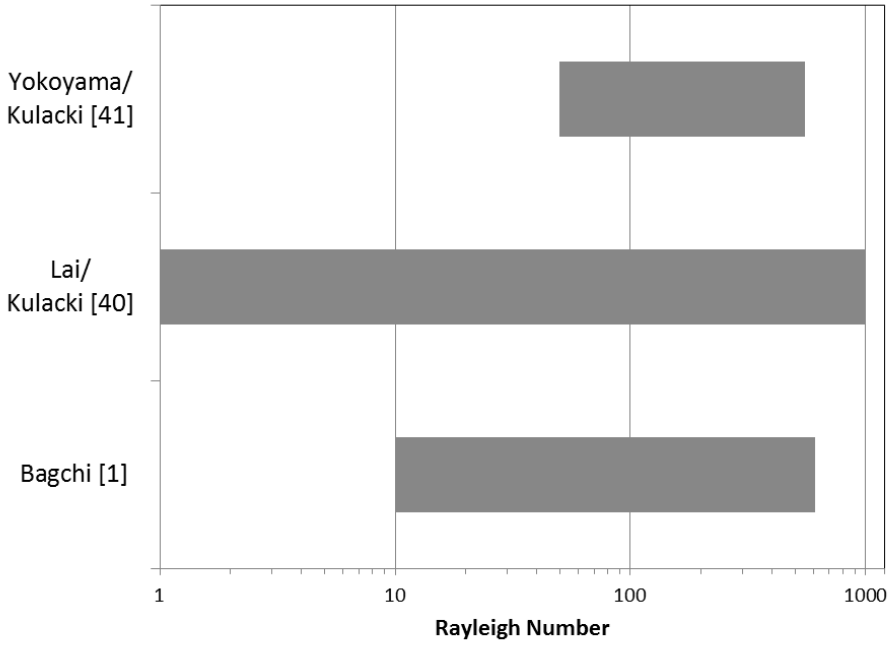


Figure 76. Rayleigh-Darcy number range of various studies.

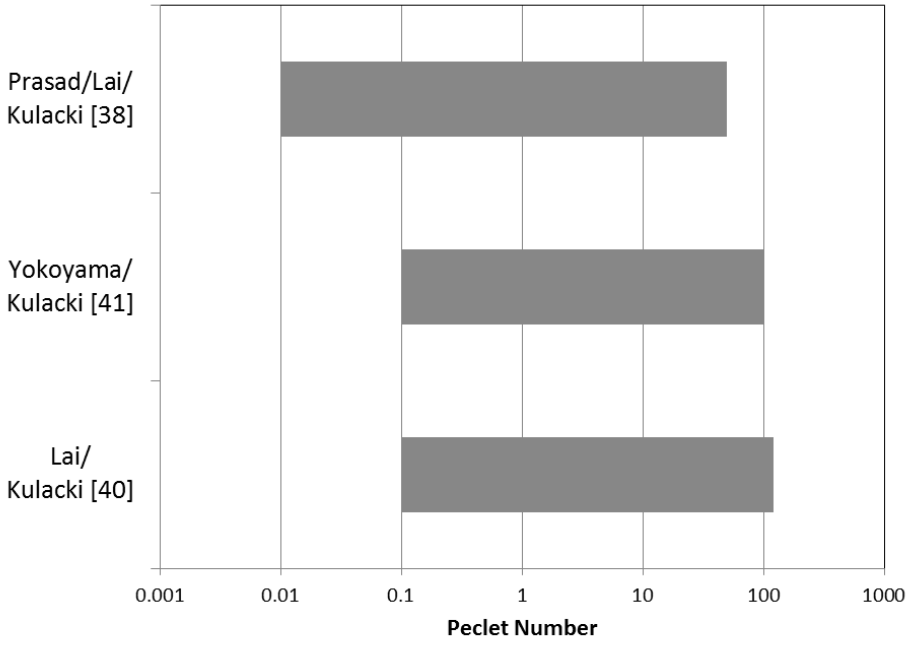


Figure 77. Peclet number range of various studies.

In conclusion, the basic dimensions of the experimental setup have been selected in order to provide a suitable range of dimensionless parameters and to minimize the error. The expected error has been shown to be within acceptable levels, and the desired range of Rayleigh number, Peclet number, heater length ratio, and porous layer height ratio can be achieved. Figure 76 and Figure 77 show several prior studies and the present study will have a similar range of parameters. Also, the pumping and power requirements have been shown to be quite reasonable.

## 5.2 Design of experiments

As briefly stated above, far too many experimental runs would be required if all the parameters were varied. The present study has the luxury of determining the experimental runs after the numerical results have been generated. Therefore, a selection has been made based on the findings of the numerical results.

The numerical results showed that increasing the Peclet number does not have any effect on the overall Nusselt number of the system below approximately a value of Pe = 10. Therefore, Peclet numbers below this value have been omitted from the experimental testing, aside from the natural convection case, where Pe = 0.

Below a Rayleigh-Darcy number of approximately 10 (based on $\Delta T$), the expected temperature difference between the minimum and maximum of the system is small enough that the expected uncertainty reaches unacceptable levels. Also, little to no difference in the overall Nusselt number is observed in the numerical results below a Rayleigh-Darcy number of 10. Therefore, the Rayleigh number range is limited to greater than 10. Also, a Rayleigh-Darcy number of 300 based on $\Delta T$ corresponds to a Rayleigh-Darcy number ranging from 2000 to 10,000 based on heat flux, which will provide sufficient range for the sake of comparison to that of existing studies. Therefore, values of 10, 30, 100, and 300 for Rayleigh-Darcy number provide a suitable range that will have acceptable uncertainty and will extend the experimental envelope beyond existing studies.

Prior studies have shown that the mixed convection results can all be collapsed to a single curve, with a single independent variable of $\mathrm{RaDa}/\mathrm{Pe}^{3/2}$, where low values indicate the forced convection regime, high values indicate the natural convection

regime, and intermediate values indicate the transition between the two, or the mixed convection regime. Therefore, achieving the full range of this parameter is necessary, but it is not necessary to achieve the full range of Rayleigh-Darcy number for each and every Peclet number, and the focus is in the transition regime. However, the critical Peclet number phenomenon is observed in this transitional zone, so enough runs should be conducted in the transitional region for each Rayleigh-Darcy number to sufficiently capture the critical Peclet number. Values of 0, 10, 30, 100, and 300 for the Peclet number provide sufficient resolution across a range of Rayleigh-Darcy number and $\eta$ values to attempt to capture the critical Peclet number behavior.

Correlations were developed numerically at six different values of the porous layer height. For comparison to existing results, experiments at $\eta = 1$ and $\eta = 0$ were required, but a limited range of intermediate values were needed to compare with the numerical results. At values from $\eta = 0.9$ down to $\eta = 0.5$, interesting behavior was observed, but at $\eta = 0.25$, no additional insights were gained. Therefore, the experimental test matrix was limited to $\eta$ values of 0, 0.5, 0.75, 0.9, and 1.

Existing studies varied the length of the heater, showing interesting streamline and isotherm patterns [40], but also showing that the overall Nusselt number of the system was not affected, provided that the characteristic length of the Nusselt number is taken as the length of the heater. Therefore, it was decided in the present study to focus on other parameters and not to vary the heater length during the experiments. It was also shown that varying the Prandtl number did not have a significant impact on the overall Nusselt number of the system [1], therefore, the Prandtl number was not varied experimentally in the present study.

Although the Darcy number can have a large effect on the heat transfer of the system [1] [46], the experimental test matrix must be limited to a reasonable number of parameters. Therefore, the size of the porous beads was kept at a constant value of a 3 mm diameter for all experiments conducted in the present study. In addition, the conductivity ratio of glass to water is ~1, and no additional conductivity ratios were experimentally tested either. Random spherical packing has a porosity in the range of 0.36-0.40 [2], which was held at a constant of 0.38 in the present study. A follow-up

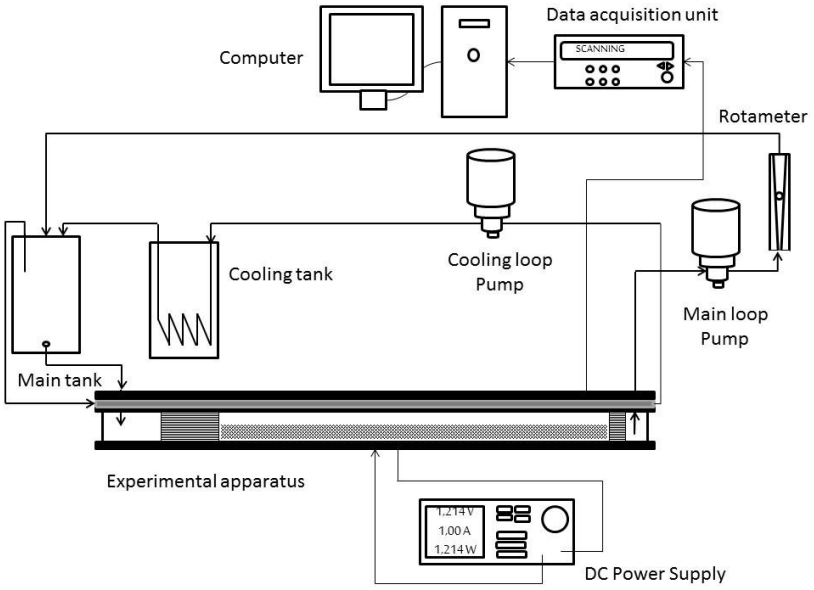


Figure 78. Schematic of experimental setup.

work could consider additional bead diameters to achieve a range of Darcy (and Forchheimer) numbers, additional types of beads to achieve a range of conductivity ratios, and additional shapes to achieve a range of porosity values.

The resulting test matrix of 75 runs covers a range of the Rayleigh number, Peclet number, and dimensionless height ratio and can be found in the appendix.

## 5.3 Experimental apparatus

The design methodology has been explained in the prior sections and it is now appropriate to discuss details of the final apparatus. The chamber constructed for the mixed convection experiments contains several sub-assemblies, which will each be explained in detail. The full apparatus is comprised of the channel assembly, the heater assembly, the flow-loop, the heat exchanger assembly, the thermocouples/data acquisition assembly, and the mounting hardware.

The chamber is assembled of five pieces of polycarbonate, each 1.27 cm thick. The base and the two side walls are each 1.7 m long and 10 cm wide. The end caps are each 10 cm by 10 cm and were machined to fit snugly into the ends of the chamber. A section of the base was machined down to make room for the heater assembly, the top of which lies flush with the rest of the base. The polycarbonate base and side walls rest on a

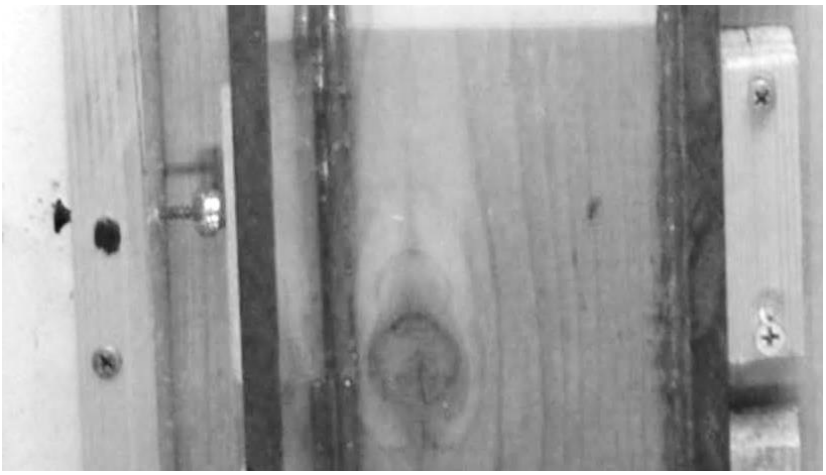

Figure 79. Side clamping mechanisms of experimental apparatus.

25 cm wide piece of cedar. To clamp the walls and the base together, individual pieces of wood were screwed into place on one side and loose pieces of wood were pressed in from the other side using screws (Figure 79), allowing individual locations to be tightened as needed.

The seams between the polycarbonate base, side walls, and end caps were joined together using silicone RTV sealant (Dow Corning 832 Multisurface RTV). Holes were drilled through the polycarbonate and wood base to feed through the heater wires. Flow straighteners were placed at the front and back of the chamber, were cut from standard plastic drinking straws, and were covered with nylon screen fine enough to keep out the glass beads. With the chamber assembled and the flow straighteners glued in place, the porous media (glass beads, 3 mm DIA) was added to the desired height and leveled by dragging a precisely cut piece of foam across the chamber.

The heater assembly consists of an electrical heater, a copper plate, and thermal grease. The electrical heater is a silicone rubber fiberglass insulated flexible heater, 10 cm x 10 cm x 1 mm (Model number SRFG-404/10). The heating elements are wire-wound and are capable of 10 Watts per square inch. The copper plate was cut precisely to size to match the dimensions of the heater and the channel, measuring 2 mm thick. This thickness was shown to be capable of maintaining a constant temperature at the surface for a variation in the convection coefficient at the surface, thus, achieving the desired constant temperature boundary condition. To maintain good thermal contact between the silicone heater and the copper plate, a moderate amount of copper-based

thermal grease was applied. The wires of the heater were fed through a hole through the bottom of the channel base and the heater was sealed into place in the channel with a bead of multi-surface RTV. The heater was powered by two DC power supplies in series, each capable of 1-40 Volts (BK Precision, Model Number 1697). Three thermocouples were attached to the surface of the copper plate using small pieces of conductive tape.

The flow loop is what produces the "mixed" rather than "natural" convection, forcing flow through the chamber. The flow loop starts with a large 2 Gal. holding tank, where water flows out from the tank through a hose to the inlet of the chamber. A gear pump (Micropump, Model Number 81808S) draws water from the outlet of the chamber and pushes it through one of two rotameters (Model Number FL-5551-ST and FL-5581-ST), each of which is metered on the outlet side by a precision Swagelok needle valve. After flowing through a rotameter, the water is then returned to the initial holding tank. A thermocouple measures the temperature in the holding tank. The main flow loop draws water from the chamber, rather than pushing it through the chamber, reducing the pressure, which greatly reduces the risk of blowing a seal and causing leaks. Standard plastic tubing was used.

The heat exchanger assembly consists of a large aluminum plate and a cedar plank, with three copper tubes sandwiched between them (Figure 80). Thermal grease was used to maintain good thermal contact between the copper tubes and the aluminum plate. In addition, the heat exchanger assembly has its own independent flow loop, consisting of a gear pump (Micropump, Model Number 81808S), several lengths of hose, and a cooling coil submerged in an additional two gallon holding tank of water. The heat exchanger assembly serves several purposes. First, the heat exchanger sits on top of the channel and acts as the ceiling of the test chamber. Second, the heat exchanger maintains the chamber ceiling at a near-constant temperature. Third, the secondary cooling coil in the heat exchanger flow loop cools the water, keeping the primary holding tank temperature from climbing over time.

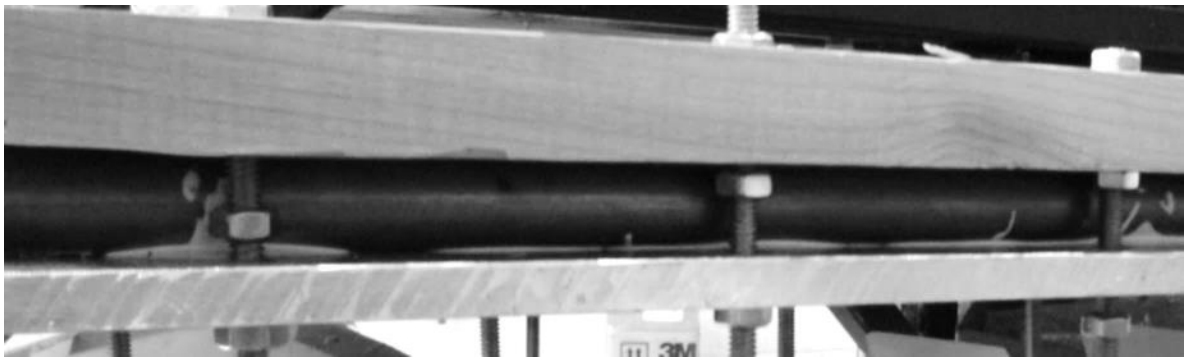

Figure 80. Side view of the heat exchanger assembly.

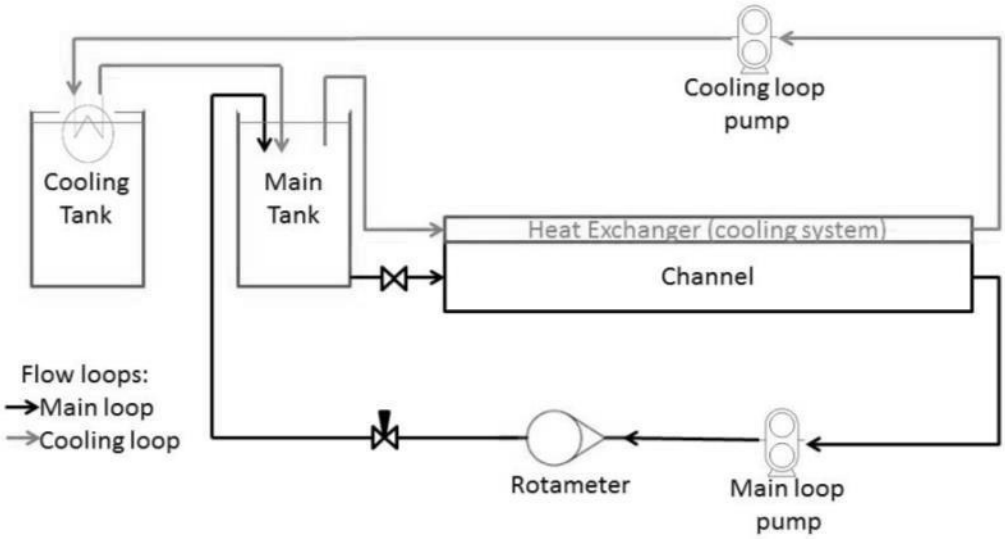


Figure 81. Flow loop diagram for experimental apparatus.

The data acquisition system consists of a computer to log the data, a scanning data acquisition unit (Hewlett Packard Model Number 34970A), and 40 J-type thermocouples. The Data acquisition unit is capable of scanning hundreds of thermocouples per second and outputting the data to a computer. Thermocouples were placed on the aluminum plate, in the main holding tank, three on the heater surface, and the remaining 35 throughout the chamber. The thermocouples were placed throughout the chamber, primarily in the vicinity of the heater, to measure the temperature profile. Seven holes were drilled and tapped into the aluminum plate on the heat exchanger and threaded rod was cut to length and screwed into place, allowing thermocouples to be attached at specific heights and at specific locations within the chamber. The thermocouple wires

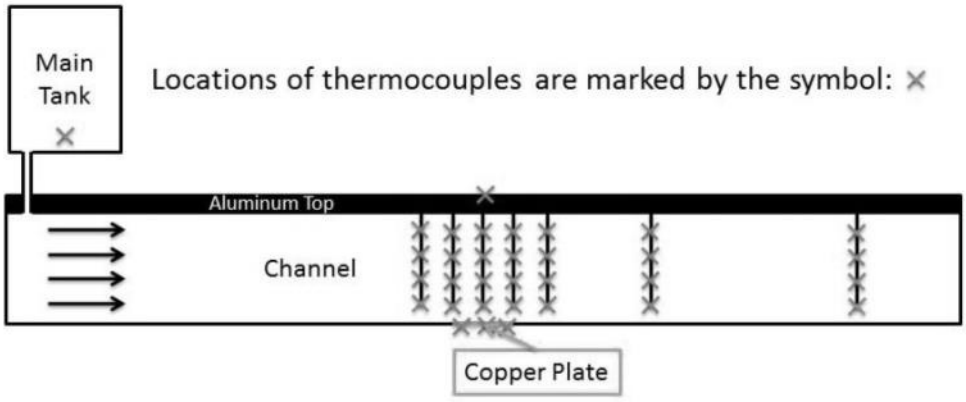


Figure 82. Diagram of thermocouple locations on experimental apparatus.

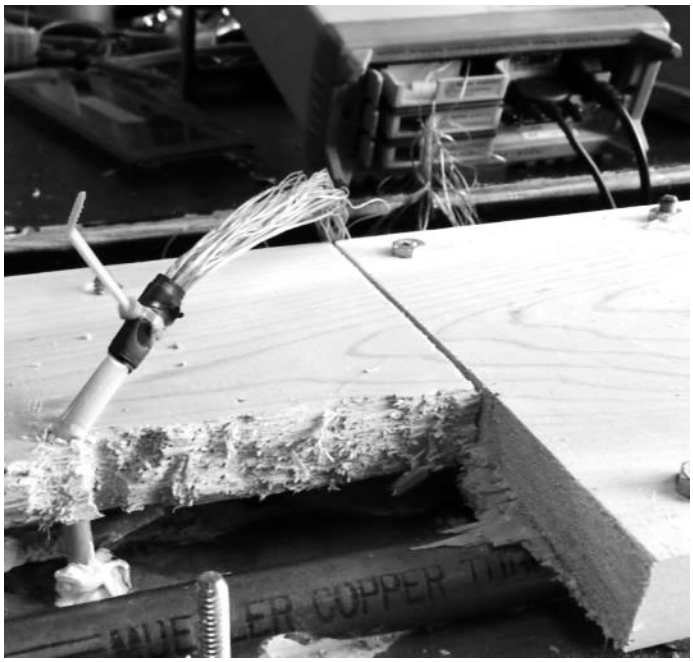

Figure 83. Thermocouple wires routed through heat exchanger to data acquisition unit.

were routed along the top of the chamber, along the aluminum plate, where they were fed up through a sealed hole and out the top of the heat exchanger assembly.

The entire assembly was held together using threaded rods. In addition, a bead of RTV was placed along the top edges of the channel to form a good seal between the polycarbonate walls and the top aluminum plate. Nuts and washers were tightened on the threaded rods to produce a clamping force, thus ensuring a good seal and avoiding any leaks.

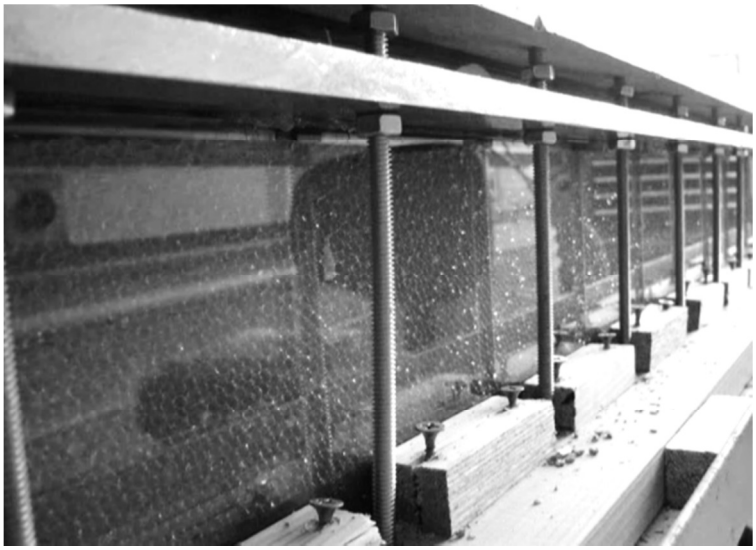

Figure 84. Threaded rod clamping heat exchanger assembly to the channel.

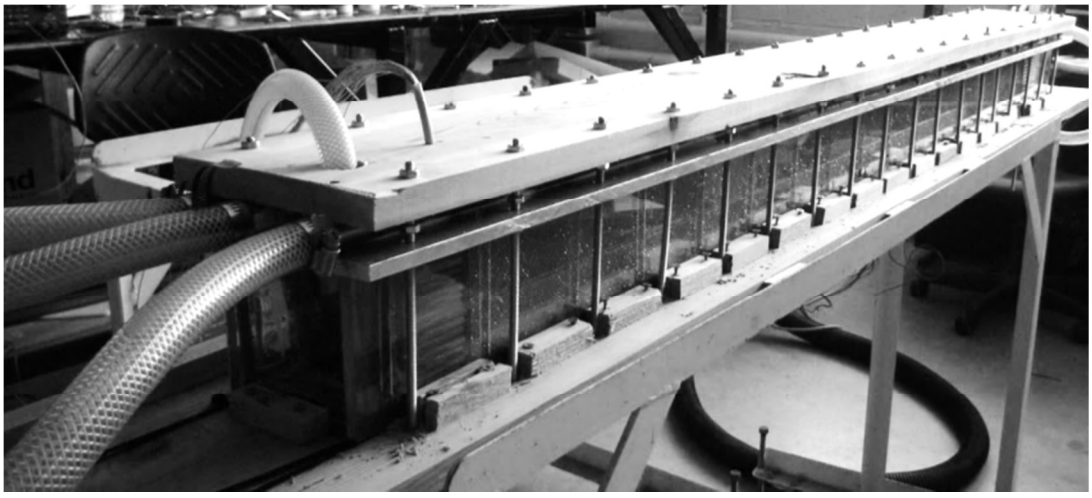

Figure 85. Photograph of final assembly of experimental apparatus.

When the height of beads needed to be changed, the RTV between the polycarbonate side walls and the aluminum plate had to be cut away and the heat exchanger assembly had to be lifted off and set aside, which was quite the laborious process. The excess RTV was scraped away from all surfaces and the sealing surfaces were thoroughly cleaned and dried before the level of beads was changed. A fresh bead of RTV was then put down and the chamber reassembled and retightened.

In conclusion, the experimental apparatus has been described in detail. The apparatus contains several sub-assemblies, the channel, the flow loop, the heat exchanger, the thermocouples/data acquisition system, and the mounting hardware, all of which are

assembled together resulting in the final product shown in Figure 85. The next section described the procedure followed while collecting data with the above apparatus.

## 5.4 Experimental procedure

In the previous sections, the design methodology was outlined in great detail, and the design and assembly of the experimental apparatus were thoroughly explained. Next, the procedure for collecting data must be thoroughly described.

First, the height of beads had to be set for the current group of runs. Five porous layer heights were tested, $\eta$ = 0, 0.5, 0.75, 0.9, and 1. As described in the previous section, the heat exchanger assembly had to be removed in order to change the porous layer height. Once the apparatus was fully assembled, it was filled with water and any remaining leaks at the top surface were stopped.

Before any data could be collected, the chamber had to be evacuated of all air bubbles. Even a thin layer of air provides a great deal of insulation and would greatly impact the heat transfer characteristic of the system. The outlet port for the main flow loop was installed in the aluminum plate at the top of the chamber in order to allow for air bubbles to escape. Even so, the chamber had to be tilted to an angle of approximately 15 degrees in order to evacuate the air bubbles from the chamber.

Water was then run through the heat exchanger and the channel, with cold water being added to the secondary holding tank in order to bring the entire chamber to a constant starting temperature of approximately 21 $^{o}$C. This was done until the aluminum plate and the primary holding tank were within 0.5 $^{o}$C of each other to maintain the constant temperature boundary condition at the top surface and the inlet. Throughout the experiments, these two temperatures were constantly monitored and maintained at approximately 21 $^{o}$C and within 0.5 $^{o}$C of each other.

The pump and the rotameter/valve in the main flow loop were then adjusted to the suitable flowrate to achieve the desired Peclet number for the current run. To achieve the correct flowrate, several adjustments had to be made over time, sometimes taking an hour before the flow rate was stable. The rotameter reading was monitored throughout each run to ensure a constant flow rate.

The power supplies for the heater were then engaged. As the heater temperature changed, the resistance changed, and the power supplies occasionally had to be adjusted to achieve the desired power. Once the temperature had stabilized, the power supplies were capable of maintaining a constant power quite well.

The data acquisition system was then engaged, logging thermocouple data every 20 seconds. Temperatures were monitored and allowed to reach steady-state over the course of many hours. As the data was logged, the computer software displayed the temperature on strip charts, clearly showing any remaining transience in the system temperature.

Once the system had reached steady state, the power was recorded, the rotameter reading was recorded, and the temperature data was saved.

# Chapter 6. Experimental Results

The experimental setup and experimental procedure were previously described and now the experimental results can be presented. The data reduction procedure is outlined, the thermal conductivity of the porous medium is defined, and finally the results are presented.

## 6.1 Data reduction

The raw data from the experimental testing is presented in the appendix. Power is measured into the heater, and temperatures of the heater, top plate, and free stream are measured. The flowrate through the chamber was measured, and the dimensions and properties of the system are known.

The convective heat transfer coefficient is determined by the usual relation.

$$q = hA(T_{heater} - T_{\infty}). \tag{114}$$

The area is known and 100 $cm^2$, but some is lost due to the sealant used to eliminate leaks in the vicinity of the heater, leaving 8.5 cm x 8.5 cm of area for the copper heat plate. The temperature of the heater is measured by taking the average of two thermocouple readings attached to the copper heating surface. Initially three thermocouples were used, but part way through the experiments, one of the thermocouples failed, so the average of the two remaining thermocouples was used for all 75 of the experimental runs. The temperature of the free stream, $T_{\infty}$, was taken as the average of the top plate temperature and the inlet temperature of the fluid. These two temperatures are within 0.5 $^oC$ of each other throughout the testing, typically less than 0.1 $^oC$, to match with the boundary conditions enforced in the numerical code. The power, q, is measured directly from the power supply, but the heat losses had to be taken into account.

To estimate the heat losses, a one-dimensional thermal resistance model is used. This model considered the heater to be a plane source of heat, with two heat paths: one with conduction up through the copper plate and convection into the test chamber and the other with conduction through the polycarbonate and wood base and convection into the

ambient air. Because of the inherently good insulating properties of wood and polycarbonate, additional insulation was not used. The temperature of the ambient air was measured to be approximately 19 $^{o}$C due to the heavy air conditioning. The convection coefficient from the bottom of the wood base into the ambient air was estimated based on several factors. Although a convection coefficient of 5-10 W/m$^2$-K is found in many textbooks for natural convection in air, this value was found to be far too high for the present situation. Estimates from the conduction model put the temperature difference between the wood base and the ambient air at a range of essentially zero up to a few degrees Celsius, which corresponds to a Rayleigh number ranging from 0 to 25 based on the heater width. This range is well below the critical Rayleigh number of 1708, which means the heat transfer is due to conduction only. Based on the present numerical results for the aspect ratio of the current system, the Nusselt number off the bottom of the wood base is approximately Nu = 2, which corresponds to a convection coefficient of ~2 W/m$^2$-K.

With all the parameters defined except for the convection coefficient into the test chamber, an iterative procedure is used to determine the unknown value. Initially, a value is calculated for the convection coefficient by assuming no heat losses. This value is then used in the thermal resistance model and the amount of heat lost to the ambient is determined. The heat input, q, is then updated (reduced) to account for the heat losses and a new convection coefficient was calculated. This new value is used in the thermal resistance model, leading to a different value for the heat loss. The procedure is repeated until the heat loss and convection coefficient were no longer changing with additional iterations. This procedure is followed for each experimental run, leading to a unique heat loss correction for each data point.

With the convection coefficient determined for each run, the thermal conductivity of the porous medium had to be determined to calculate the Nusselt number from the experimental data. The thermal conductivity of water was calculated at the film temperature between the heater and the inlet/top plate. The thermal conductivity of the glass beads was determined with great care by Aichlmayr [14] using the same glass beads used in the present study. A value of 0.64 W/m-K is used for the thermal conductivity of the beads, which corresponds to a conductivity ratio ranging from 1.02 to 1.04 based on

the variation in the fluid conductivity due to temperature. Therefore, the question of what correlation is appropriate for the stagnant thermal conductivity becomes irrelevant, because they all have negligible differences at a conductivity ratio so close to unity.

The Rayleigh number is much more straightforward to calculate. The same $\Delta T$ is used as used to calculate the convection coefficient. The permeability is known from Eqn. (50), the porosity is 0.38, the height is 10 cm, and the 3 mm diameter glass beads. The stagnant thermal conductivity was used in the thermal diffusivity, and the remaining thermo physical properties are calculated at the film temperature for each run.

The Peclet number is calculated using the stagnant thermal diffusivity, the mass average fluid velocity, and the height of the chamber.

## 6.2 Tables of results

Using the values and processes described, the Nusselt number, Rayleigh number, and Peclet number are all calculated for each experimental run. Once the Rayleigh number and Peclet number had been determined, additional numerical results were generated based on these precise values to provide a suitable comparison. The average error was approximately thirty percent between the experimental and numerical results, with a peak error of sixty-seven percent. However, due to the nature of natural and mixed convection, this is not excessively high. If the onset of convection point is missed, large errors are quite possible, as the Nusselt number changes rapidly in the vicinity of the critical value.

Table 8. Experimental Results for η = 1

| Run | η | δ | Nu experimental | Nu numerical | Ra | Pe | error |
|---|---|---|---|---|---|---|---|
| 1 | 1 | 1 | 2.29 | 2.74 | 34.95 | 0.0 | 16% |
| 2 | 1 | 1 | 6.47 | 4.91 | 85.83 | 0.0 | 24% |
| 3 | 1 | 1 | 13.07 | 8.18 | 223 | 0.0 | 37% |
| 4 | 1 | 1 | 3.32 | 3.16 | 43.63 | 9.9 | 5% |
| 5 | 1 | 1 | 6.50 | 5.25 | 96.52 | 9.9 | 19% |
| 6 | 1 | 1 | 11.60 | 7.1 | 234 | 9.7 | 39% |
| 7 | 1 | 1 | 4.15 | 6.66 | 60.45 | 30.2 | 38% |
| 8 | 1 | 1 | 7.24 | 7.21 | 126.7 | 30.0 | 0% |
| 9 | 1 | 1 | 11.83 | 8.28 | 265.6 | 29.7 | 30% |
| 10 | 1 | 1 | 6.19 | 11.29 | 78.03 | 99.8 | 45% |
| 11 | 1 | 1 | 7.44 | 11.9 | 247.8 | 100.6 | 37% |
| 12 | 1 | 1 | 14.29 | 12.21 | 358.3 | 100.0 | 15% |
| 13 | 1 | 1 | 9.74 | 19.05 | 88.28 | 300.2 | 49% |
| 14 | 1 | 1 | 13.76 | 19.13 | 223.9 | 296.6 | 28% |
| 15 | 1 | 1 | 7.78 | 19.02 | 40.32 | 301.2 | 59% |

Table 9. Experimental Results for η = 0.9

| Run | η | δ | Nu experimental | Nu numerical | Ra | Pe | error |
|---|---|---|---|---|---|---|---|
| 16 | 0.90 | 1 | 3.65 | 5.75 | 47.95 | 0.0 | 36% |
| 17 | 0.90 | 1 | 8.51 | 9.04 | 126.6 | 0.0 | 6% |
| 18 | 0.90 | 1 | 15.23 | 13.36 | 336.3 | 0.0 | 12% |
| 19 | 0.90 | 1 | 2.93 | 4.58 | 48.18 | 9.9 | 36% |
| 20 | 0.90 | 1 | 7.34 | 6.11 | 108.6 | 9.8 | 17% |
| 21 | 0.90 | 1 | 13.50 | 11.38 | 279.3 | 9.7 | 16% |
| 22 | 0.90 | 1 | 3.74 | 6.16 | 54.4 | 31.3 | 39% |
| 23 | 0.90 | 1 | 7.29 | 6.7 | 108.3 | 31.1 | 8% |
| 24 | 0.90 | 1 | 12.34 | 7.8 | 240 | 29.7 | 37% |
| 25 | 0.90 | 1 | 4.74 | 10.23 | 77.24 | 102.1 | 54% |
| 26 | 0.90 | 1 | 8.58 | 10.48 | 149.7 | 101.4 | 18% |
| 27 | 0.90 | 1 | 15.90 | 10.64 | 240 | 96.3 | 33% |
| 28 | 0.90 | 1 | 6.54 | 16.38 | 102 | 283.0 | 60% |
| 29 | 0.90 | 1 | 11.25 | 16.51 | 207.1 | 280.6 | 32% |
| 30 | 0.90 | 1 | 16.46 | 16.79 | 419.5 | 277.1 | 2% |

Table 10. Experimental Results for η = 0.75

| Run | η | δ | Nu experimental | Nu numerical | Ra | Pe | error |
|---|---|---|---|---|---|---|---|
| 31 | 0.75 | 1 | 4.66 | 10.19 | 70.23 | 0.0 | 54% |
| 32 | 0.75 | 1 | 9.50 | 13.11 | 165.1 | 0.0 | 28% |
| 33 | 0.75 | 1 | 16.26 | 17.61 | 425.1 | 0.0 | 8% |
| 34 | 0.75 | 1 | 3.80 | 9.46 | 70.75 | 8.8 | 60% |
| 35 | 0.75 | 1 | 9.06 | 12.51 | 162 | 10.9 | 28% |
| 36 | 0.75 | 1 | 15.71 | 17.41 | 426.6 | 11.8 | 10% |
| 37 | 0.75 | 1 | 3.42 | 8.3 | 54.87 | 30.2 | 59% |
| 38 | 0.75 | 1 | 7.22 | 11.29 | 117.9 | 30.0 | 36% |
| 39 | 0.75 | 1 | 14.93 | 14.24 | 392.7 | 29.5 | 5% |
| 40 | 0.75 | 1 | 4.06 | 8.22 | 69.03 | 102.2 | 51% |
| 41 | 0.75 | 1 | 7.61 | 8.62 | 133.6 | 101.6 | 12% |
| 42 | 0.75 | 1 | 12.45 | 9.42 | 275.2 | 100.5 | 24% |
| 43 | 0.75 | 1 | 5.70 | 12.5 | 87.8 | 283.3 | 54% |
| 44 | 0.75 | 1 | 9.87 | 12.72 | 174.7 | 281.2 | 22% |
| 45 | 0.75 | 1 | 14.55 | 13.21 | 358.9 | 277.9 | 9% |

Table 11. Experimental Results for $\eta = 0.5$

| Run | η | δ | Nu experimental | Nu numerical | Ra | Pe | error |
|---|---|---|---|---|---|---|---|
| 46 | 0.50 | 1 | 5.94 | 16.95 | 94.46 | 0.0 | 65% |
| 47 | 0.50 | 1 | 11.32 | 21.44 | 244 | 0.0 | 47% |
| 48 | 0.50 | 1 | 18.20 | 26.49 | 638.8 | 0.0 | 31% |
| 49 | 0.50 | 1 | 5.74 | 17.35 | 98.63 | 7.6 | 67% |
| 50 | 0.50 | 1 | 11.22 | 21.42 | 249.9 | 8.6 | 48% |
| 51 | 0.50 | 1 | 18.01 | 26.19 | 654.7 | 6.3 | 31% |
| 52 | 0.50 | 1 | 5.69 | 15.81 | 95.01 | 31.2 | 64% |
| 53 | 0.50 | 1 | 10.91 | 20.59 | 241.7 | 30.8 | 47% |
| 54 | 0.50 | 1 | 17.73 | 25.94 | 651.8 | 29.1 | 32% |
| 55 | 0.50 | 1 | 4.45 | 7.7 | 64.54 | 102.2 | 42% |
| 56 | 0.50 | 1 | 10.55 | 18.71 | 238.1 | 100.7 | 44% |
| 57 | 0.50 | 1 | 17.30 | 24.81 | 600.3 | 98.9 | 30% |
| 58 | 0.50 | 1 | 5.35 | 10.66 | 84.4 | 299.7 | 50% |
| 59 | 0.50 | 1 | 9.25 | 11 | 172.5 | 297.4 | 16% |
| 60 | 0.50 | 1 | 13.76 | 11.71 | 360.1 | 293.8 | 15% |

Table 12. Experimental Results for η = 0

| Run | η | δ | Nu experimental | Nu numerical | Ra | Pe | error |
|---|---|---|---|---|---|---|---|
| 61 | 0 | 1 | 31.30 | 30.54 | 36.99 | 0.0 | 2% |
| 62 | 0 | 1 | 51.49 | 36.88 | 91.12 | 0.0 | 28% |
| 63 | 0 | 1 | 76.17 | 44.49 | 214.1 | 0.0 | 42% |
| 64 | 0 | 1 | 26.07 | 31.74 | 44.45 | 12.2 | 18% |
| 65 | 0 | 1 | 49.40 | 36.92 | 91.32 | 6.5 | 25% |
| 66 | 0 | 1 | 71.89 | 45.1 | 226.8 | 10.9 | 37% |
| 67 | 0 | 1 | 22.85 | 32.73 | 51.16 | 30.2 | 30% |
| 68 | 0 | 1 | 52.16 | 36.69 | 87.94 | 30.1 | 30% |
| 69 | 0 | 1 | 70.35 | 45.33 | 230.8 | 29.8 | 36% |
| 70 | 0 | 1 | 25.52 | 29.94 | 34.82 | 102.5 | 15% |
| 71 | 0 | 1 | 41.90 | 36.12 | 81.89 | 101.1 | 14% |
| 72 | 0 | 1 | 74.79 | 44.94 | 217.4 | 100.9 | 40% |
| 73 | 0 | 1 | 26.55 | 25.8 | 37 | 268.1 | 3% |
| 74 | 0 | 1 | 48.58 | 29.76 | 76.71 | 316.5 | 39% |
| 75 | 0 | 1 | 68.92 | 34.73 | 179.3 | 297.5 | 50% |

## 6.3 Comparison of experimental and numerical data

The processed experimental results show some of the same trends as the numerical results. However, unlike the numerical results, the dimensionless parameters (particularly the Rayleigh number) could not be held exactly constant for a series of runs. When curves are shown of constant Rayleigh number there is really a band of Rayleigh number within which all the data points fall, which explains some of the unexpected behavior, such as the drop in Nusselt number at high Peclet number observed for several curves.

Figure 86-Figure 90 show the experimental results including the error bars. The error bars were calculated individually for each experimental run as outlined in the appendix.

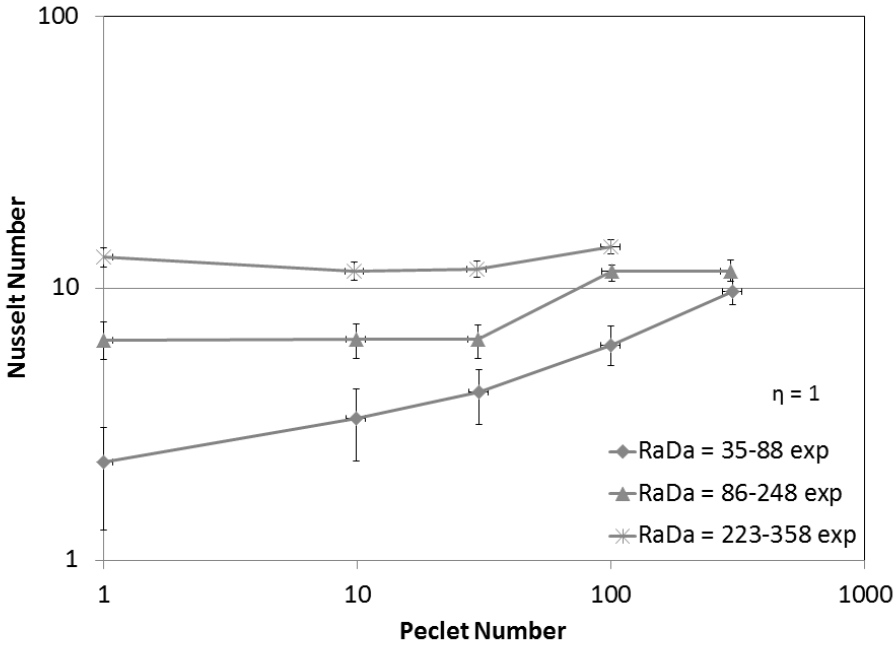


Figure 86. Experimental results of Nusselt verses Peclet number for η = 1.

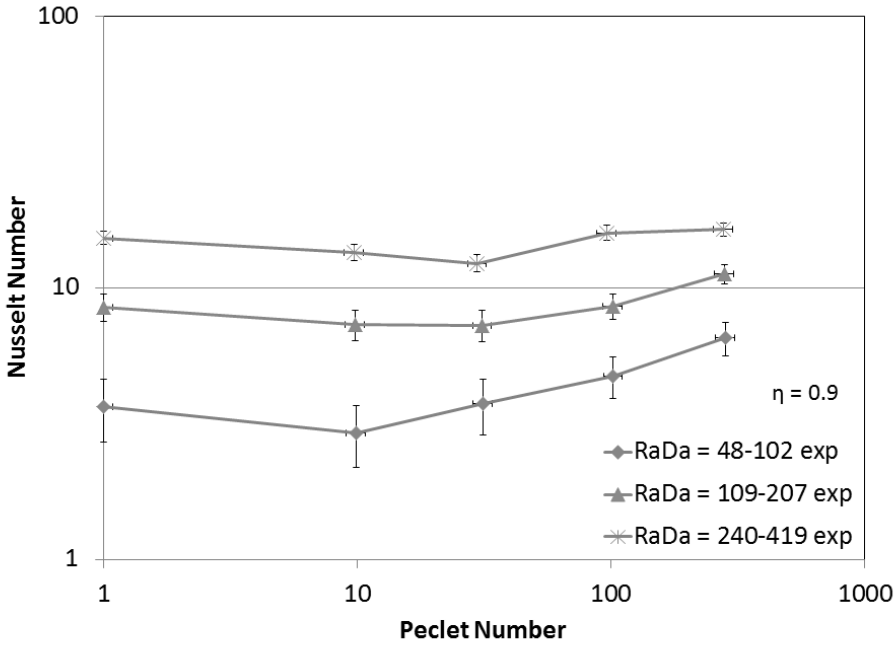


Figure 87. Experimental results of Nusselt verses Peclet number for η = 0.9.

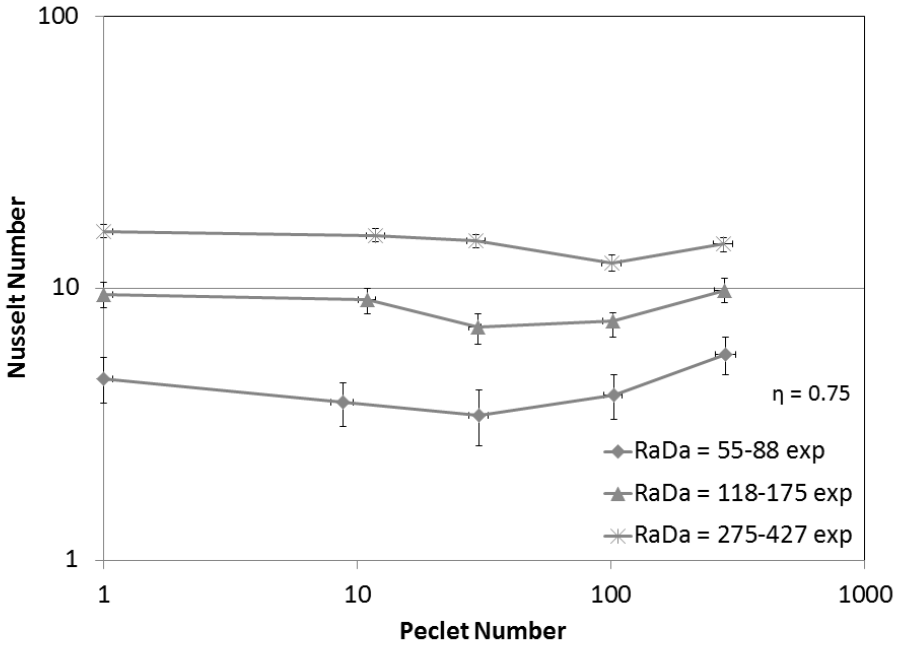


Figure 88. Experimental results of Nusselt verses Peclet number for η = 0.75.

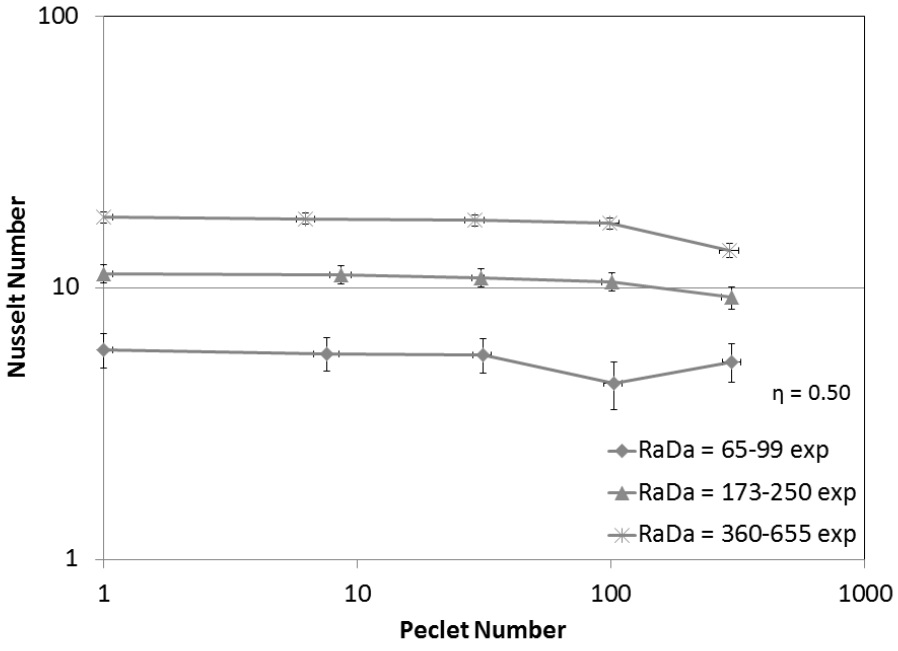


Figure 89. Experimental results of Nusselt verses Peclet number for η = 0.50.

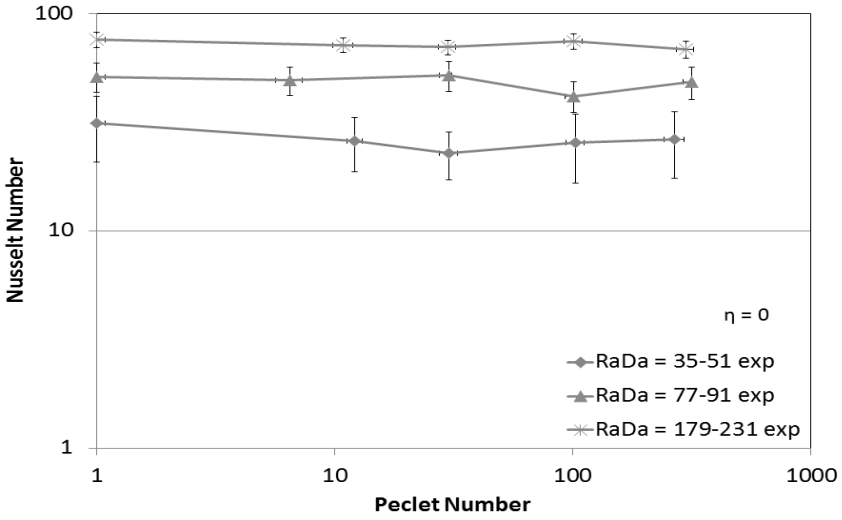


Figure 90. Experimental results of Nusselt verses Peclet number for η = 0.

Although there is no porous layer for η = 0 in Figure 90, the results were still plotted as a function of the Rayleigh-Darcy number, using the same Darcy number of 7.14E-7 as used for Figures 86-89.

The above graphs confirm several trends also found in the numerical results. First, there is a critical Peclet number where the heat transfer is a minimum. This critical Peclet number is observed in many cases and is shown to increase with the increasing Rayleigh-Darcy number. In addition, the critical Rayleigh-Darcy number is shown to increase with decreasing porous layer height ratio, η. These results confirm the trends shown in the numerical results and further discussion of these trends is found in the numerical results chapter.

As previous authors have done [38,40,59], the Nusselt, Rayleigh, and Peclet number results can be collapsed onto a single line, where the independent parameter is $\mathrm{RaDa}/\mathrm{Pe}^{1.5}$ and the dependent parameter is $\mathrm{Nu}/\mathrm{Pe}^{0.5}$. The data is presented in this form, followed by curve fits of the bounds of the uncertainty for the experimental data along with the numerical results. As can be seen, the numerical results fall generally within the experimental bounds of uncertainty, although discrepancies exist. In these cases, the Rayleigh-Darcy number is based on the heat flux, not the temperature difference as outlined in Lai and Kulacki [40].

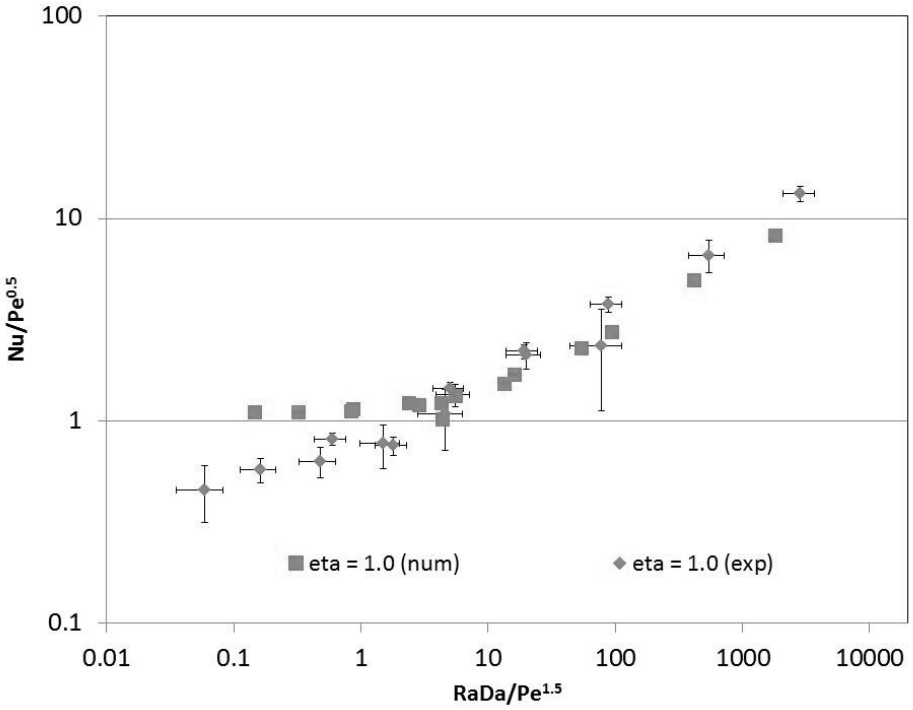


Figure 91. Experimental and numerical results for $\eta = 1$.

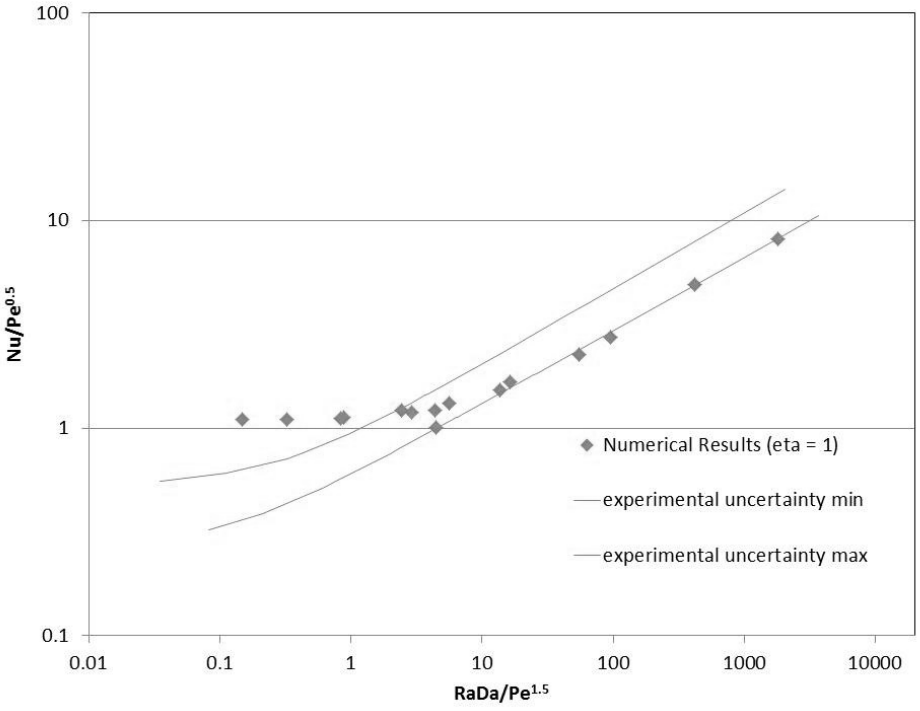


Figure 92. Comparison of numerical results to experimental uncertainty bounds ($\eta = 1$).

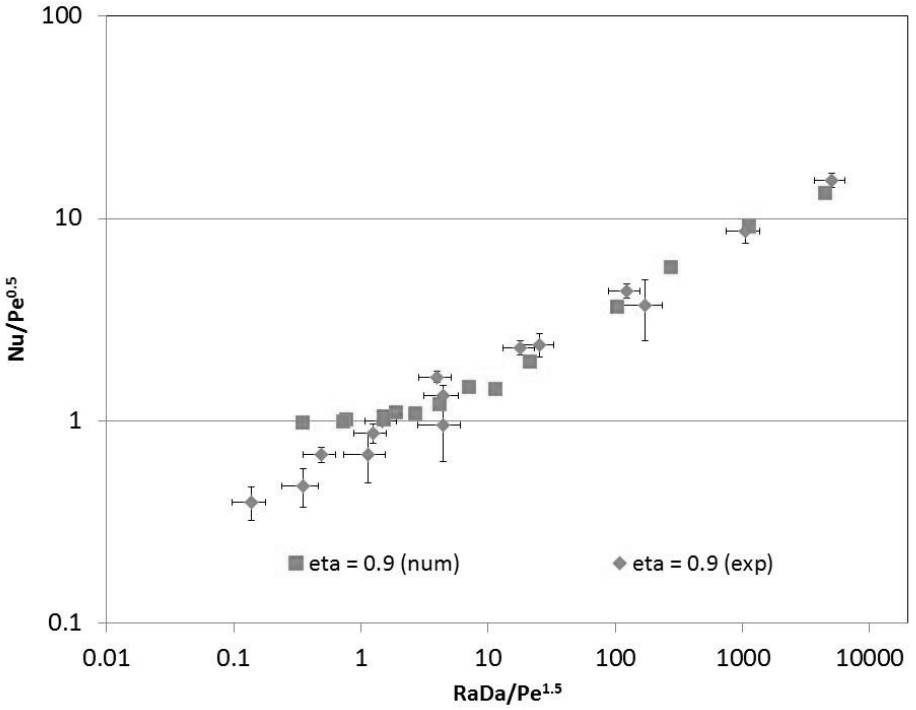


Figure 93. Experimental and numerical results for η = 0.9.

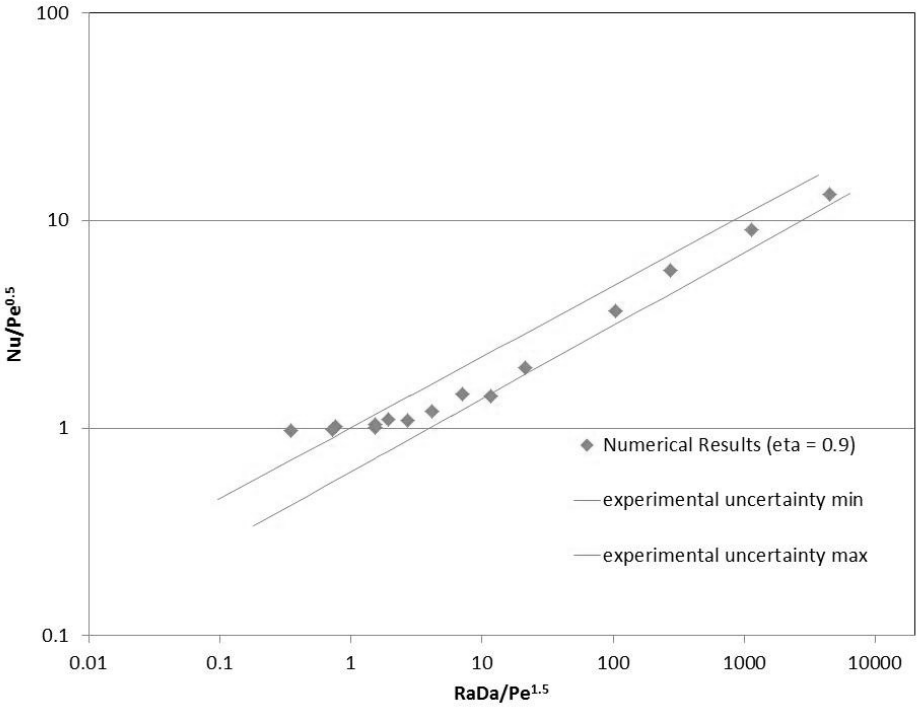


Figure 94. Comparison of numerical results to experimental uncertainty bounds (η = 0.9).

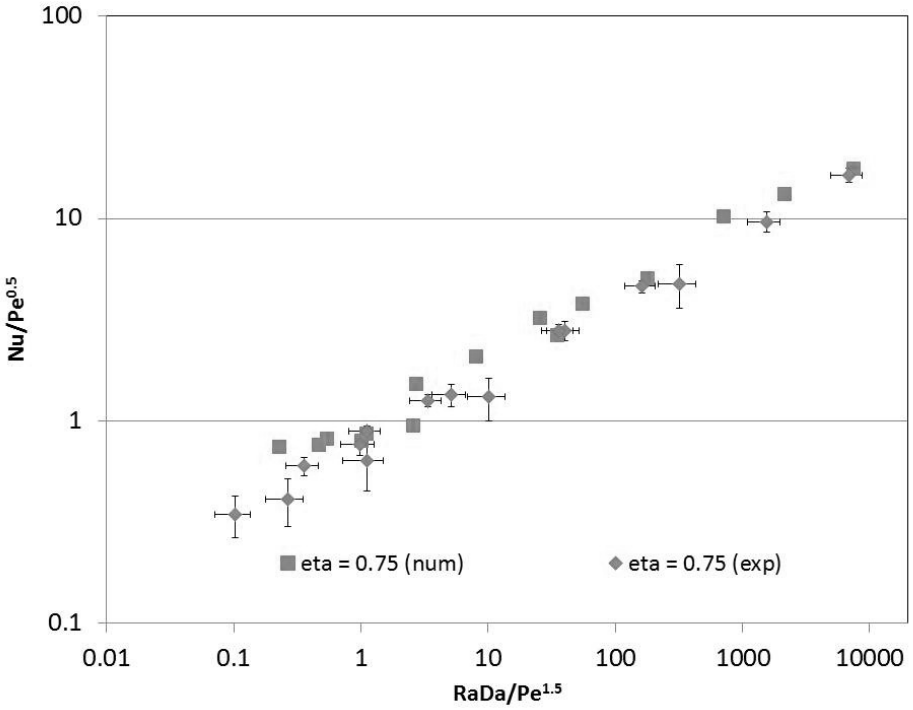


Figure 95. Experimental and numerical results for $\eta = 0.75$.

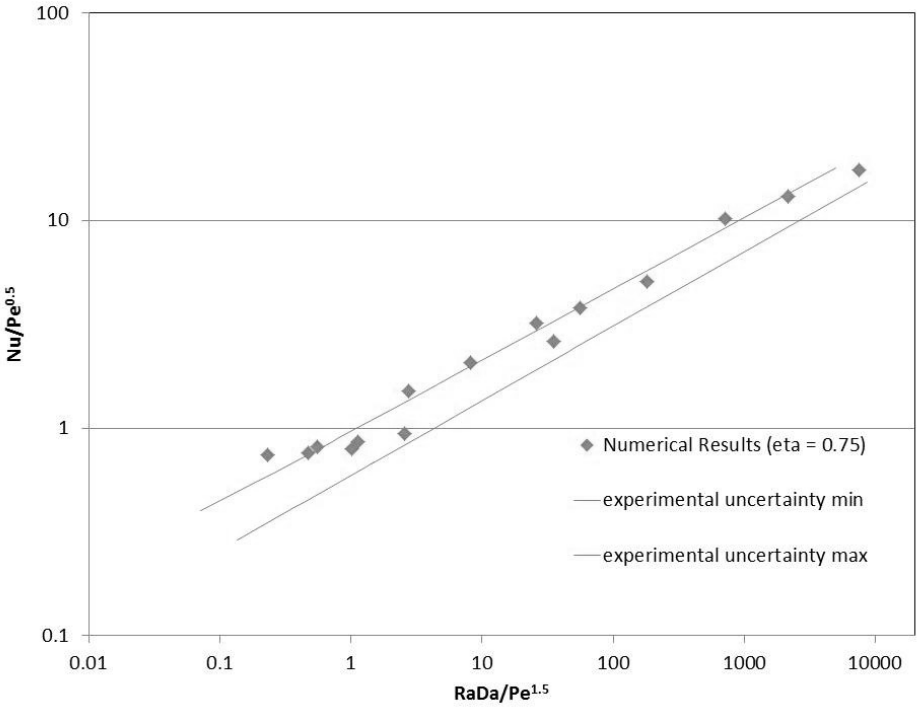


Figure 96. Comparison of numerical results to experimental uncertainty bounds ($\eta = 0.75$).

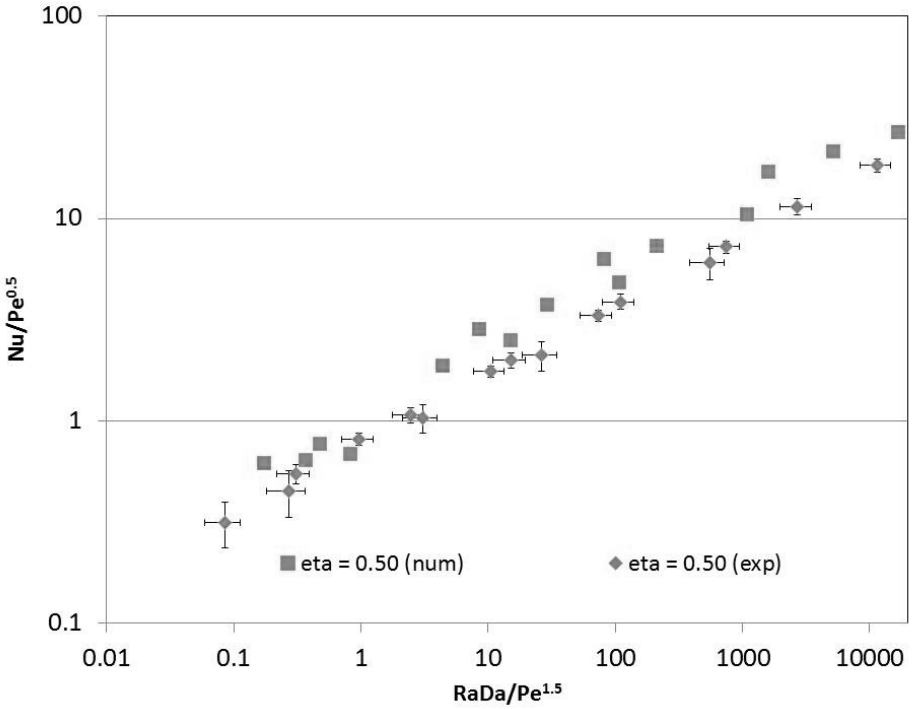


Figure 97. Experimental and numerical results for η = 0.5.

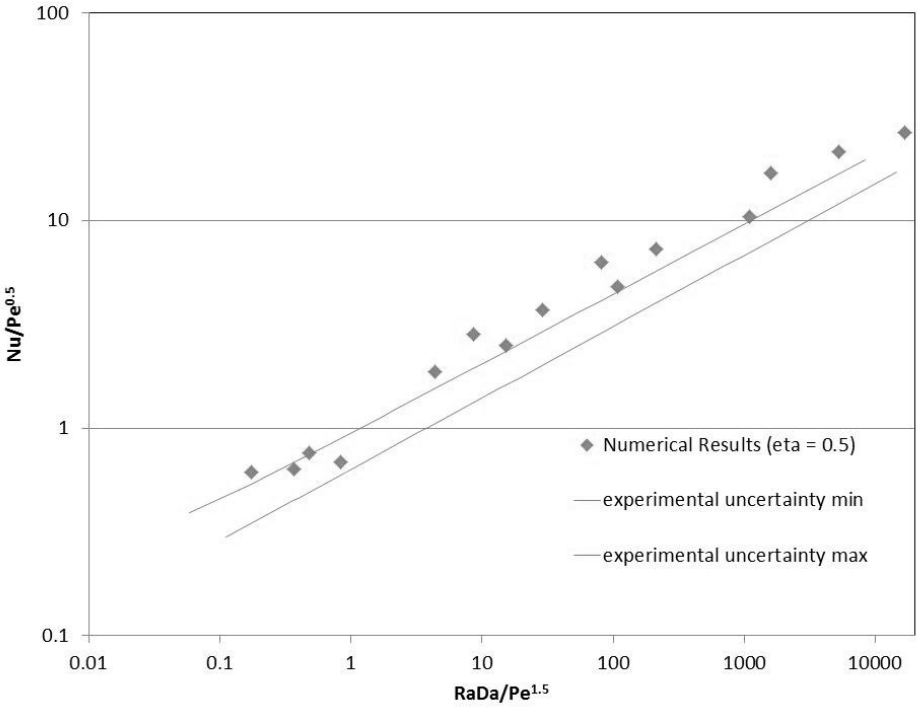


Figure 98. Comparison of numerical results to experimental uncertainty bounds (η = 0.5).

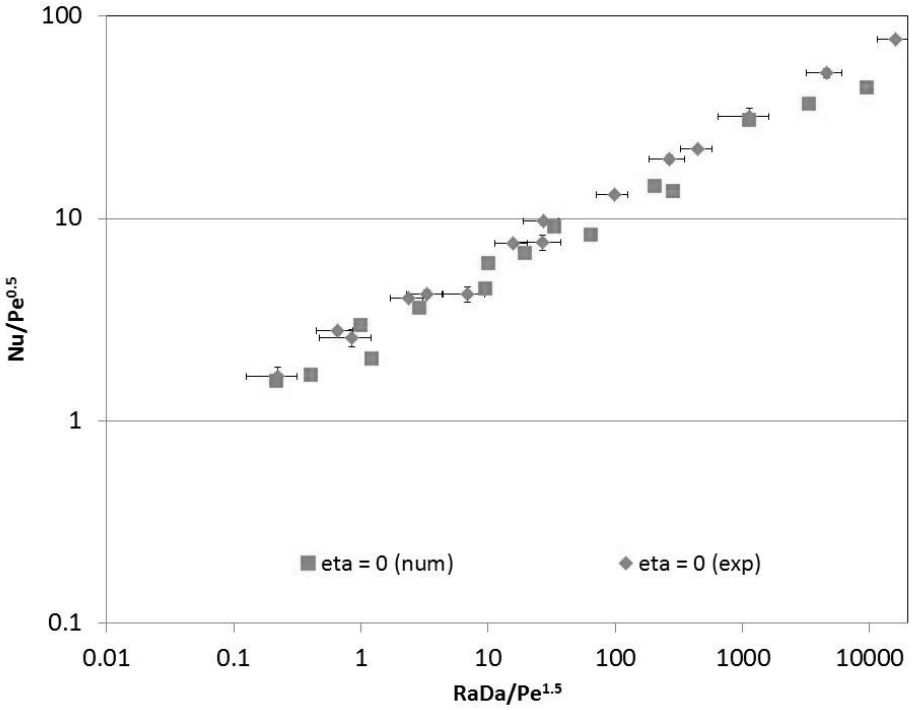


Figure 99. Experimental and numerical results for $\eta = 0$.

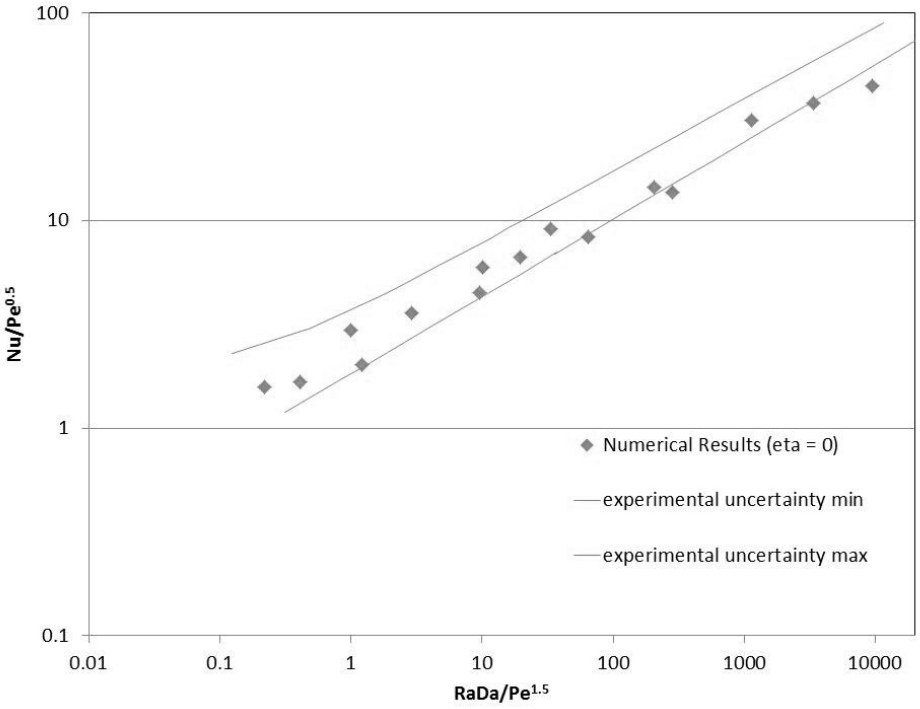


Figure 100. Comparison of numerical results to experimental uncertainty bounds ($\eta = 0$).

The above results show general agreement between experimental and numerical results with a few noteworthy exceptions. First, for $\eta = 0.75$, 0.9, and 1, the numerical results show a clear flat region on the left side, but the experimental results only show this for $\eta = 1$. The flat side on the left of the graph represents the forced convection regime, where the Rayleigh number is outweighed by the Peclet number, the asymptote to the right represents the natural convection regime, where the Rayleigh number outweighs the Peclet number, and the curve in the middle of the graph represents the mixed convection regime. Based on this, it would appear that the transition to forced convection occurs later in the experiments than in the numerical results.

For most cases, the natural convection numerical data falls within the bounds of uncertainty, but $\eta = 0.5$ does not. Actually, a trend can be seen, where $\eta = 1$ numerical results fall near the bottom bound of uncertainty, $\eta = 0.9$ fall in the middle, $\eta = 0.75$ fall along the upper bound, and $\eta = 0.5$ fall above the upper bound. This could suggest that the numerical results over predict the heat transfer due to natural convection in the fluid layer, but at $\eta = 0$, the numerical results fall nicely between the bounds of uncertainty on the experimental data. This leaves the porous layer and the interface. However, the interfacial effects would be felt similarly for all intermediate height ratios, which suggests that the discrepancy could lie in the porous layer heat transfer. As the porous layer shrinks, the numerical results over predict the experimental results.

If the permeability of the porous medium was increased in the numerical simulations, the Nusselt number would increase the most for $\eta = 1$, less for $\eta = 0.9$ through $\eta = 0.5$, and not at all for $\eta = 0$, which would better match the experimental findings. But this would cause the transition to forced convection to occur even sooner as the flow inside the porous layer would be less restricted.

The discrepancies could be due to the simplifying assumptions. Some assumptions were shown to be reasonable through simulation, design features, and experimental data, such as the constant temperature boundary condition on the copper plate above the heater, the constant temperature at the inlet and top plate, and parallel flow through the flow straightener. Others were less accurate, such as two-dimensional flow, a fully developed velocity profile at the inlet and outlet for boundary conditions, and neglecting the ¼" diameter threaded rod protruding down into the porous layer

holding the thermocouples in place. Although speculation is a valuable exercise, the exact reasons for these discrepancies are not known at this time.

## 6.4 Correlation equations

Separate correlation equations for each height ratio were produced for experimental and numerical results. These correlation equations are,

$$\frac{\mathrm{Nu}}{\mathrm{Pe}^{0.5}} = \left(0.101 + 0.379\frac{\mathrm{RaDa}}{\mathrm{Pe}^{1.5}}\right)^{0.367} \quad \eta = 1, \text{experimental}, \tag{115}$$

$$\frac{\mathrm{Nu}}{\mathrm{Pe}^{0.5}} = \left(1.238 + 0.133\frac{\mathrm{RaDa}}{\mathrm{Pe}^{1.5}}\right)^{0.382} \quad \eta = 1, \text{numerical}, \tag{116}$$

$$\frac{\mathrm{Nu}}{\mathrm{Pe}^{0.5}} = \left(0.0 + 0.508\frac{\mathrm{RaDa}}{\mathrm{Pe}^{1.5}}\right)^{0.348} \quad \eta = 0.9, \text{experimental}, \tag{117}$$

$$\frac{\mathrm{Nu}}{\mathrm{Pe}^{0.5}} = \left(0.815 + 0.205\frac{\mathrm{RaDa}}{\mathrm{Pe}^{1.5}}\right)^{0.403} \quad \eta = 0.9, \text{numerical}, \tag{118}$$

$$\frac{\mathrm{Nu}}{\mathrm{Pe}^{0.5}} = \left(0.0 + 0.458\frac{\mathrm{RaDa}}{\mathrm{Pe}^{1.5}}\right)^{0.348} \quad \eta = 0.75, \text{experimental}, \tag{119}$$

$$\frac{\mathrm{Nu}}{\mathrm{Pe}^{0.5}} = \left(0.310 + 0.375\frac{\mathrm{RaDa}}{\mathrm{Pe}^{1.5}}\right)^{0.383} \quad \eta = 0.75, \text{numerical}, \tag{120}$$

$$\frac{\mathrm{Nu}}{\mathrm{Pe}^{0.5}} = \left(0.0 + 0.466\frac{\mathrm{RaDa}}{\mathrm{Pe}^{1.5}}\right)^{0.339} \quad \eta = 0.5, \text{experimental}, \tag{121}$$

$$\frac{\mathrm{Nu}}{\mathrm{Pe}^{0.5}} = \left(0.082 + 0.818\frac{\mathrm{RaDa}}{\mathrm{Pe}^{1.5}}\right)^{0.366} \quad \eta = 0.5, \text{numerical}, \tag{122}$$

$$\frac{\mathrm{Nu}}{\mathrm{Pe}^{0.5}} = \left(1.025 + 1.15 * 10^{-5}\frac{\mathrm{Ra}}{\mathrm{Pe}^{1.5}}\right)^{0.353} \quad \eta = 0, \text{experimental}, \tag{123}$$

$$\frac{\mathrm{Nu}}{\mathrm{Pe}^{0.5}} = \left(1.915 + 5.54 * 10^{-6}\frac{\mathrm{Ra}}{\mathrm{Pe}^{1.5}}\right)^{0.355} \quad \eta = 0, \text{numerical}. \tag{124}$$

Interestingly, when the curve fits for the experimental data are plotted, there is a clear distinction between the $\eta = 0$ fit and the rest of the curve fits. Figure 101 shows all the experimental curve fits and Figure 102 shows all the numerical curve fits, each including a curve fit of all the data excluding the $\eta = 0$ case.

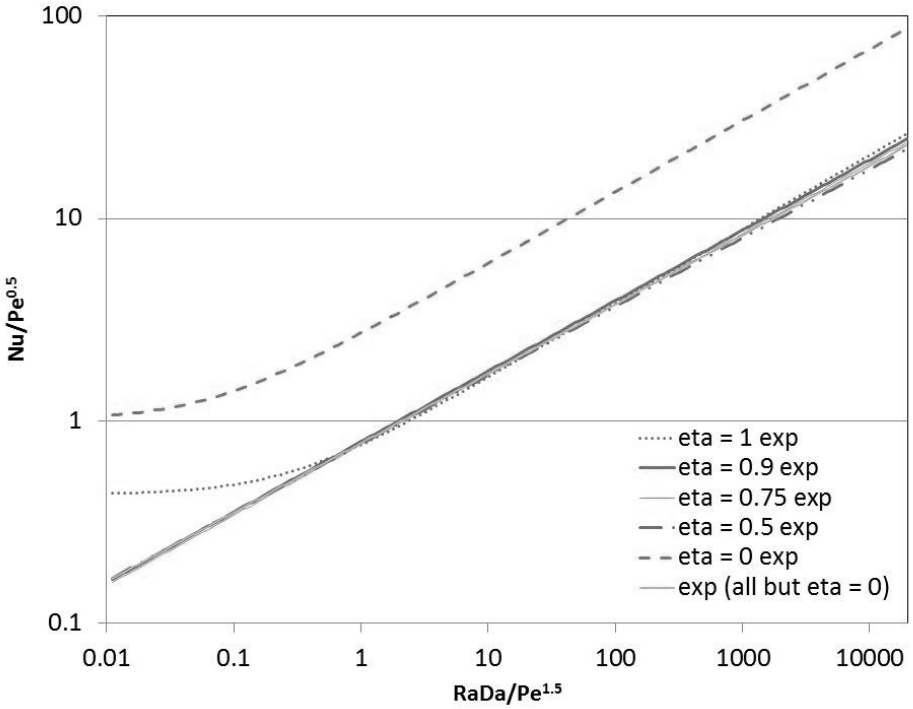


Figure 101. Curve fits for experimental data.

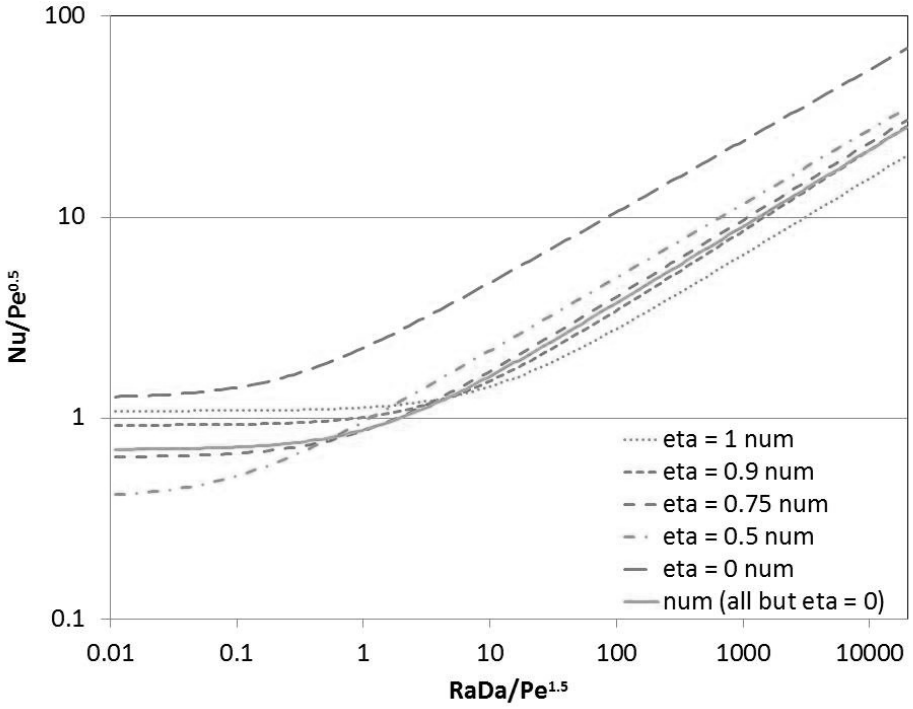


Figure 102. Curve fits for numerical data.

The experimental curve fits for $\eta = 1$ and $\eta = 0$ show the flat region to the left (forced convection regime) but the other $\eta$ values do not, but the numerical curve fits show the flat region to the left for all cases. In both cases, the $\eta = 0$ data stands apart from the rest of the data. Interestingly, the experimental curve fits for the intermediate $\eta$-values lie quite close to each other, but the numerical results do not show this same behavior. It is quite surprising that changing the porous layer height has a negligible impact on the experimental results in the two-domain system. In fact, even the experimental results for $\eta = 1$ match well except for the forced convection regime portion of the curve. It would seem that without a full porous height, the flow tends to stay out of the porous domain more than anticipated.

It was observed in the numerical results chapter that the transition to the forced convection regime occurs at higher Peclet numbers as the porous layer height gets smaller. In fact, in many cases, the transition was shown to occur well past Pe = 300. Therefore, it should be no surprise that much of the experimental data for the intermediate $\eta$-values does not show the flat portion to the left that would indicate the transition to the forced convection regime had been made. The fact that the experimental data does not show this is, in fact, confirmation of this earlier finding.

To review, a table of all the experimental results has been presented. The average error between the numerical and experimental results is approximately 30%. Several possible explanations for the error have been discussed. The experimental results show some of the same trends as the numerical results, such as the critical Peclet number and how it varies with the Rayleigh number and the porous layer height. The experimental data has some scatter to it, but with a curve fit to the data and uncertainty bounds plotted, the numerical results are shown to generally fall within these bounds. Curve fit equations were presented and plotted for experimental and numerical results, which highlighted the similarities in the experimental data for all of the cases except $\eta = 0$. In both experimental and numerical results, the correlation curve for $\eta = 0$ stands apart from the rest of the curves.

# Chapter 7. Conclusions and Recommendations

The problem of mixed convection in horizontal fluid saturated porous layers heated from below has been numerically solved. The numerical scheme uses a one-domain method, avoiding the need to explicitly define boundary conditions, and additional variable porosity terms were derived and included in the governing equations to model the interfacial effects in the vicinity of the interface. In addition, a test apparatus has been constructed and experimental data collected over a range of Rayleigh number, Peclet number, and porous layer height. The numerical and experimental data are thoroughly compared and the numerical results are found to generally fall within the bounds of experimental uncertainty.

## 7.1 New contributions and findings

Thorough analysis of the numerical results showed several interesting trends/results.

1. The critical Peclet number
    a. In any curve where the Rayleigh numbers, calculated independently for each sub-layer, were both below the critical value for their sublayer, no critical Peclet number could be observed. The critical Peclet number phenomenon is caused by the cross flow disrupting the recirculation flow, so if there is no recirculation flow there is no critical Peclet number.
    b. The value of the critical Peclet number increases with increasing Rayleigh-Darcy number.
    c. The width of the critical Peclet number effect becomes noticeably wider as the porous layer height decreases. This is because the transition to the forced convection regime occurs at a higher Peclet number when at lower $\eta$-values, and it is this transition to forced convection that "pulls" the heat transfer out of the critical Peclet number dip.
2. Numerical variation of parameters
    a. Varying the conductivity ratio between the solid and fluid phases can have a significant effect on the overall heat transfer of the system. Therefore,

the effective conductivity must be reliably determined to match numerical and experimental data.

b. The effect of dispersion has a small impact on the overall Nusselt number in the natural and mixed convection regimes and has a larger impact in the forced convection regime. In all cases, including dispersion increased the Nusselt number.

c. The Forchheimer term, the Brinkman term, and the convective terms all have negligible impact on the overall Nusselt number of the system across the range of parameters used in the present study.

d. Varying the Prandtl number by a factor of 10 in each direction has negligible impact on the Nusselt number of the system.

3. Streamlines and isotherms

   a. The majority of the cross flow occurs in the fluid layer (assuming $\eta < 1$)

   b. The thermal plume increases dramatically in strength when it emerges from the porous layer. The plume narrows because there is less time to conduct heat outward.

   c. The recirculating streamlines due to natural convection are locally contained for a full porous layer but quickly extend to reach the far boundaries of the system when in a fluid layer.

   d. At high enough Peclet number, the isotherms show the thermal energy being washed out the outlet before having a chance to emerge from the porous layer.

4. Experimental results

   a. Surprisingly, there is very little change in the Nusselt number when the porous layer height is varied from $\eta = 1$ to $\eta = 0.5$ (where all the resolution for the current study is focused), but there is significant change from $\eta = 0.5$ down to $\eta = 0$ (where there is no resolution from the present study).

   b. Within the bounds of uncertainty, the numerical results generally agree with the experimental results.

   c. The critical Peclet number was confirmed experimentally.

5. Correlation equations were presented for both numerical and experimental results for a range of η-values.

## 7.2 Suggestions for future research

Several suggestions for future research have arisen throughout the current research. These suggestions could be completed using the same test apparatus as used in the present study.

1. Investigate smaller heater lengths down to a line or wire source of heat. This would change the character of the plume and produce interesting results.
2. Conduct experiments at lower porous layer heights. It is suspected that the penetrating effects from the fluid layer into the porous layer would better reach the heater and may produce more noticeable changes in the Nusselt number with a smaller porous layer.
3. Change the size of the porous beads to vary the Darcy number.
4. Increase the Peclet number for the experiments to determine if/when the transition to forced convection occurs at intermediate η-values.

## Bibliography


[1] A. Bagchi, Natural Convection in Horizontal Fluid-Superposed Porous Layers Heated Locally From Below, *PhD Dissertation,* University of Minnesota, 2010.

[2] D. Nield and A. Bejan, Convection in Porous Media, 3rd Edition, New York: Springer-Verlag, 2006.

[3] S. Whitaker, The Method of Volume Averaging, Dordrecht, The Netherlands: Kluwer Academic Publishers, 1999.

[4] D. Joseph, D. Nield and G. Papanicolaou, Nonlinear Equation Governing Flow in a Saturated Porous Medium, *Water Resources Research,* vol. 18, no. 4, pp. 1049-1052, 1982.

[5] M. Kaviani, Principles of Heat Transfer in Porous Media, New York: Springer, 2006.

[6] H. Brinkman, A Calculation of the Viscous Force Exerted by a Flowing Fluid on a Dense Swarm of Particles, *Applied Scientific Research,* vol. A1, no. 1, pp. 27-34, 1947.

[7] R. Wooding, Steady State Free Thermal Convection of Liquid in a Saturated Permeable Medium, *Journal of Fluid Mechanics,* vol. 2, no. 3, pp. 273-285, 1957.

[8] M. Carr and B. Straughan, Penetrative convection in a fluid overlying a porous layer, *Advances in Water Resources,* vol. 26, no. 3, pp. 263-276, 2003.

[9] V. M. Polyaev, A. P. Mozhaev, B. A. Galitseysky and A. L. Lozhkin, A study of internal heat transfer in nonuniform porous structures., *Expt. Therm. Fluid Sci,* vol. 12, pp. 426-432, 1996.

[10] A. G. Dixon and D. L. Cresswell, Theoretical prediction of effective heat transfer mechanisms in regular shaped packed beds, *AIChE Journal,* vol. 25, pp. 663-676, 1979.

[11] B. Alazmi and K. Vafai, Analysis of variants within the porous media transport models, Transactions ASME, *Journal of Heat Transfer,* vol. 122, pp. 303-326, 2000.

[12] F. N. A. K. H. Kuwahara, A Numerical Study of Thermal Dispersion in Porous Media, Transactions ASME, *Journal of Heat Transfer,* vol. 118, pp. 756-761, 1996.

[13] H. Rubin, Heat dispersion effect on thermal convection in a porous medium layer, *Journal of Hydrology,* vol. 21, pp. 173-185, 1974.

[14] Aichlmayr, Effective Thermal Conductivity, *Masters Thesis*, University of Minnesota, 2011.

[15] J. Delgado, Longitudinal and transverse dispersion in porous media, *Chemical Engineering Research and Design,* vol. 85, no. A9, pp. 1245-1252, 2007.

[16] J. V. A. Bear, Modelling Groundwater flow and pollution, New York: Springer, 1987.

[17] G. Beavers and D. Joseph, Boundary conditions at a naturally permeable wall, *Journal of Fluid Mechanics,* vol. 30, no. 1, pp. 197-207, 1967.

[18] G. Neale and W. Nader, Practical Significance of Brinkman's Extension of Darcy's Law. Coupled Parallel Flows Within a Channel and a Bounding Porous Medium, *Canadian Journal of Chemical Engineering,* vol. 52, no. 4, pp. 475-478, 1974.

[19] I. Jones, Low Reynolds number flow past a porous spherical shell, *Proceedings Cambridge Philosophical Society,* pp. 231-238, 1973.

[20] D. Nield, The Beavers-Joseph Boundary Condition and Related Matters: A Historical and Critical Note, *Transport in Porous Med,* vol. 78, pp. 537-540, 2009.

[21] J. Ochoa-Tapia and S. Whitaker, Momentum Transfer at the Boundary Between a Porous Medium and a Homogeneous Fluid - 1. Theoretical Development, *International Journal of Heat and Mass Transfer,* vol. 38, no. 14, pp. 2635-2646, 1995.

[22] J. Ochoa-Tapia and S. Whitaker, Momentum Transfer at the Boundary Between a Porous Medium and a Homogeneous Fluid - II. Comparison With Experiment, *International Journal of Heat and Mass Transfer,* vol. 38, no. 14, pp. 2647-2655, 1995.

[23] J. Ochoa-Tapia, J. Del Rio and S. Whitaker, Bulk and Surface Diffusion In Porous Media: An Application Of The Surface-Averaging Theorem, *Chemical Engineering Science,* vol. 48, no. 11, pp. 2061-2082, 1993.

[24] M. Sahraoui and M. Kaviani, Slip and No-Slip Temperature Boundary Conditions at

the Interface of Porous, Plain Media: Convection, *International Journal of Heat and Mass Transfer,* vol. 37, no. 6, pp. 1029-1044, 1994.

[25] B. Alazmi and K. Vafai, Analysis of Fluid Flow and Heat Transfer Interfacial Conditions Between a Porous Medium and a Fluid Layer, *International Journal of Heat and Mass Transfer,* vol. 44, pp. 1735-1749, 2001.

[26] A. Nabovati and A. Sousa, Fluid Flow Simulation at Open-Porous Medium Interface Using the Lattice Boltzmann Method, *International Journal of Numerical Methods in Fluids,* vol. 56, pp. 1449-1456, 2008.

[27] H. Bai, P. Yu, S. Winoto and H. Low, Lattice Boltzmann Method for Flows in Porous and Homogeneous Fluid Domains Coupled at the Interface by Stress Jump, *International Journal of Numerical Methods in Fluids,* vol. 60, pp. 691-708, 2009.

[28] S. Hirata and B. Goyeau, Stability of Natural Convection in Superposed Fluid and Porous Layers: Equivalence of the One- and Two-Domain Approaches, *International Journal of Heat and Mass Transfer,* vol. 52, pp. 533-536, 2009.

[29] R. A. Wooding, Convection in a saturated porous medium at large Reynolds number or Peclet number, *Journal of Fluid Mechanics,* vol. 15, pp. 527-544, 1963.

[30] M. Prats, The effects of horizontal fluid flow on thermally induced convection currents in porous mediums., *International Journal of Heat and Mass Transfer,* vol. 50, pp. 1455-1468, 1966.

[31] F. M. Sutton, Onset of convection in a porous channel with net through flow., *Physics of Fluids,* vol. 13, pp. 1931-1934, 1970.

[32] G. M. Homsy and A. E. Sherwood, Convective instabilities in porous media with through flow., *AIChE Journal,* vol. 22, pp. 168-174, 1976.

[33] M. A. Combarnous and P. Bia, Combined free and forced convection in porous media., *Society of Petrolium Engineers,* vol. 11, pp. 399-405, 1971.

[34] D. C. Reda, Mixed Convection in a Liquid-Saturated Porous Medium, Transactions ASME, *Journal of Heat Transfer,* vol. 110, pp. 147-154, 1988.

[36] F. C. Lai and F. A. Kulacki, Oscillatory mixed convection in a horizontal porous

layer locally heated from below, *International Journal of Heat and Mass Transfer,* vol. 34, no. 3, pp. 887-890, 1991.

[37] F. C. Lai and F. A. Kulacki, Non-Darcy Mixed Convection Along a Vertical Wall in a Saturated Porous Medium, Transactions ASME, *Journal of Heat Transfer,* vol. 113, pp. 252-255, 1991.

[38] F. Lai, V. Prasad and F. Kulacki, Aiding and Opposing Mixed Convection in a Vertical Porous Layer With a Finite Wall Heat Source, *International Journal of Heat and Mass Transfer,* vol. 31, no. 5, pp. 1049-1061, 1988.

[39] F. Lai, I. Pop and F. Kulacki, Free and Mixed Convection From Slender Bodies of Revolution in Porous Media, *International Journal of Heat and Mass Transfer,* vol. 33, no. 8, pp. 1767-1769, 1990.

[40] F. Lai and F. Kulacki, Experimental Study of Free and Mixed Convection in Horizontal Porous Layers Locally Heated From Below, *International Journal of Heat and Mass Transfer,* vol. 34, no. 2, pp. 525-541, 1991.

[41] Y. Yokoyama, F. Kulacki and R. Mahajan, Mixed Convection in a Horizontal Porous Duct With a Sudden Expansion and Local Heating From Below, Transactions ASME, *Journal of Heat Transfer,* vol. 121, pp. 653-661, 1999.

[42] I. Pop, D. Ingham and I. Miskin, Mixed Convection in a Porous Medium Produced by a Line Heat Source, *Transport in Porous Media,* vol. 18, pp. 1-13, 1995.

[43] J. Jang and C. Shiang, The Mixed Convection Plume Along a Vertical Adiabatic Surface Embedded in a Non-Darcian Porous Medium, *International Journal of Heat and Mass Transfer,* vol. 40, no. 7, pp. 1693-1699, 1997.

[44] A. Nakayama, A Unified Theory for Non-Darcy Free, Forced, and Mixed Convection Problems Associated With A Horizontal Line Heat Source in a Porous Medium, Transactions ASME, *Journal of Heat Transfer,* vol. 116, pp. 508-513, 1994.

[45] J. Zhou and F. Lai, Aiding and Opposing Mixed Convection from a Cylinder in a Saturated Porous Medium, *Journal of Porous Media,* vol. 5, no. 2, pp. 103-111, 2002.

[46] J. P. Kumar, J. C. Umavathi and I. Pop, Fully Developed Mixed Convection Flow in a Vertical Channel Containing Porous and Fluid Layers with Isotherma or Isoflux Boundaries, *Transport in Porous Media,* vol. 80, pp. 117-135, 2009.

[47] D. Bhargavi, Forced Convection Heat Transfer With Viscous Dissipation In Parallel Plate Channels Partially Filled With Porous Material, *PhD Thesis,* India Institute of Technology Kharagpur, 2011.

[48] J. W. Elder, Steady free convection in a porous medium heated from below, *Journal of Fluid Mechanics,* vol. 27, no. 1, pp. 29-48, 1967.

[49] V. Prasad and F. A. Kulacki, Natural convection in horizontal porous layers with localized heating from below, Transactions ASME, *Journal of Heat Transfer,* vol. 109, no. 3, pp. 795-798, 1987.

[50] V. Prasad and F. A. Kulacki, Effects of the size of heat source on natural convection in horizontal porous layers heated from below, Transactions ASME, *Journal of Heat Transfer,* vol. 5, pp. 2677-2682, 1986.

[51] P. Cheng, A. Chowdhury and C. T. Hsu, Forced convection in packed tubes and channels with variable porosity and thermal dispersion effects, *Convective Heat and Mass Transfer in Porous Media,* vol. 196, pp. 625-653, 1991.

[52] G. A. O. Altamirano, Direct Numerical Simulation of Natural Convection Flows, Unpublished manuscript, 2007.

[53] V. Geraldes, V. Semiao and M. N. Pinho, Numerical modelling of mass transfer in slits with semi-permeable membrane walls, *Engineering Computations,* vol. 17, no. 3, pp. 192-217, 2000.

[54] K. Hollands, G. Raithby and L. Konicek, Correlation equations for free convection heat transfer in horiztonal layers of air and water, *International Journal of Heat and Mass Transfer,* vol. 18, pp. 879-884, 1975.

[55] R. M. Clever and F. H. Busse, Transition to time-dependent convection, *Journal of Fluid Mechanics,* vol. 6, pp. 625-635, 1974.

[56] N. Ouertatani, N. B. Cheikh, B. B. Beya and T. Lili, Numerical simulation of two-dimensional Rayleigh-Benard convection in an enclosure., *Comptes Rendus*

*Mecanique,* vol. 336, no. 5, pp. 464-470, 2008.

[57] J. P. Caltagirone, Thermoconvective instabilities in a horizontal porous layer, *Journal of Fluid Mechanics,* vol. 72, no. 20, pp. 269-287, 1975.

[58] R. J. Buretta and A. S. Berman, Convective heat transfer in a liquid saturated porous layer, *Journal of Applied Mechanics,* vol. 98, pp. 249-253, 1976.

[59] V. Prasad, F. Lai and F. Kulacki, Mixed Convection in Horizontal Porous Layers Heated From Below, *Journal of Heat Transfer,* vol. 110, pp. 395-402, 1988.

[60] Y. Katto and Y. Masuoka, Criterion for the onset of convective flow in a fluid in a porous medium, *International Journal of Heat and Mass Transfer,* vol. 10, no. 3, pp. 297-309, 1967.

[61] F. Chen and C. Chen, Experimental investigation of convective stability in a superposed fluid and porous layer when heated from below, *J. Fluid Mech.,* vol. 207, pp. 311-321, 1989.

[62] V. Prasad, Flow Instabilities and Heat Transfer in Fluid Overlying Horizontal Porous Layers, *Experimental Thermal and Fluid Science,* vol. 6, pp. 135-146, 1993.

[63] S. Kim and C. Choi, Convective heat transfer in porous and overlying fluid layers heated from below, *Int. J. Heat Mass Transfer,* vol. 39, no. 2, pp. 319-329, 1996.

[64] K. Vafai and S. Kim, Fluid mechanics of the interface region between a porous medium and a fluid layer - an exact solution, *International Journal of Heat and Fluid Flow,* vol. 11, no. 3, pp. 254-256, 1990.

[65] K. Vafai and R. Thiyagaraja, Analysis of flow and heat transfer at the interface region of a porous medium, *International Journal of Heat and Mass Transfer,* vol. 30, no. 7, pp. 1391-1405, 1987.

[66] A. Singh and G. Thorpe, Natural Convection in a confined fluid overlying a porous layer -a comparison study of different models, *Indian Journal of Pure and Applied Mathematics,* vol. 26, no. 1, pp. 81-85, 1995.

[67] P. Saffman, On the Boundary Condition at the Interface of a Porous Medium, *Studies in Applied Mathematics.,* vol. 1, pp. 93-101, 1971.

[68] M. Quintard and S. Whitaker, Convection, Dispersion, and Interfacial Transport of

Contaminants: Homogeneous Porous Media, *Advances in Water Resources,* vol. 17, pp. 221-239, 1994.

[69] J. Ochoa-Tapia and S. Whitaker, Heat Transfer at the Boundary Between a Porous Medium and a Homogeneous Fluid, *International Journal of Heat and Mass Transfer,* vol. 40, no. 11, pp. 2691-2707, 1997.

[70] T. Masuoka, Y. Takatsu, S. Kawamoto, H. Koshino and T. Tsuruta, Buoyant Plume through a Pemeable Porous Layer Located above a Line Heat Source in an Infinite Fluid Space, *JSME International Journal,* vol. 38, no. 1, pp. 79-85, 1995.

[71] V. Kurdyumov and A. Linan, Free and Forced Convection Around Line Sources if Heat and Heated Cylinders in Porous Media, *Journal of Fluid Mechanics,* vol. 427, pp. 389-409, 2001.

[72] W. Jager and A. Mikelic, On The Interface Boundary Condition of Beavers, Joseph, and Saffman, *J. Appl. Math,* vol. 60, no. 4, pp. 1111-1127, 2000.

[73] A. J. Goldman, R. G. Cox and H. Brenner, The slow motion of two identical arbitrarily oriented spheres through a viscous fluid, *Chemical Engineering Science,* vol. 21, pp. 1151-1170, 1966.

[74] A. d'Hueppe, M. Chandesris, D. Jamet and B. Goyeau, Boundary Conditions at a Fluid-Porous Interface For a Convective Heat Transfer Problem: Analysis of the Jump Relations, *International Journal of Heat and Mass Transfer,* vol. 54, pp. 3683-3693, 2011.

[75] D. Cimpean, I. Pop, D. Ingham and J. Merkin, Fully Developed Mixed Convection Flow Between Inclined Parallel Plates Filled with a Porous Medium, *Transport in Porous Media,* vol. 77, pp. 87-102, 2009.

[76] M. S. B. Carr, Penetrative convection in a fluid overlying a porous layer, *Advances in Water Resources,* vol. 26, no. 3, pp. 263-276, 2003.

[77] P. Cheng, Combined free and forced convection flow about inclined surfaces in porous media., *International Journal of Heat and Mass Transfer,* vol. 20, pp. 807-814, 1977.

[78] P. Cheng, Similarity solutions for mixed convection from horizontal impermeable

surfaces in saturated porous media., *International Journal of Heat and Mass Transfer,* vol. 20, pp. 893-898, 1977.

[79] R. M. Fand and R. T. Pand, Combined forced and natural convection heat transfer from a horizontal cylinder embedded in a porous medium, *International Journal of Heat and Mass Transfer,* vol. 30, pp. 1351-1358, 1987.

# Appendices

## A – Data Tables

The raw data from the 75 experimental runs are given in the tables below. Appropriate averages were taken once the data had reached steady state.

Table 13. $\eta = 1$ raw experimental data.

| Run | η | δ | Volumetric flowrate [cc/min] | Measured power [W] | Estimated heat losses | Top plate temp [C] | Inlet temp [C] | Heater temp [C] |
|---|---|---|---|---|---|---|---|---|
| 1 | 1 | 1 | 0.0 | 0.37 | 18.5% | 20.6 | 20.4 | 23.5 |
| 2 | 1 | 1 | 0.0 | 1.97 | 5.4% | 20.8 | 20.6 | 27.2 |
| 3 | 1 | 1 | 0.0 | 8.13 | 2.4% | 21.3 | 20.7 | 34.6 |
| 4 | 1 | 1 | 8.4 | 0.61 | 11.9% | 20.7 | 20.5 | 24.2 |
| 5 | 1 | 1 | 8.4 | 2.23 | 5.0% | 20.5 | 20.1 | 27.5 |
| 6 | 1 | 1 | 8.4 | 7.55 | 2.7% | 21.1 | 20.5 | 34.7 |
| 7 | 1 | 1 | 25.7 | 0.98 | 9.0% | 20.8 | 20.7 | 25.5 |
| 8 | 1 | 1 | 25.7 | 3.03 | 4.5% | 20.8 | 20.5 | 29.5 |
| 9 | 1 | 1 | 25.7 | 8.54 | 2.6% | 21.0 | 20.5 | 36.3 |
| 10 | 1 | 1 | 85.1 | 1.75 | 5.7% | 20.8 | 20.6 | 26.6 |
| 11 | 1 | 1 | 87.0 | 5.16 | 4.2% | 21.0 | 20.9 | 35.6 |
| 12 | 1 | 1 | 87.0 | 12.70 | 2.1% | 21.0 | 20.6 | 39.9 |
| 13 | 1 | 1 | 255.6 | 3.07 | 3.2% | 20.2 | 20.0 | 26.9 |
| 14 | 1 | 1 | 255.6 | 8.83 | 2.2% | 20.5 | 20.3 | 34.3 |
| 15 | 1 | 1 | 255.6 | 1.23 | 5.1% | 20.8 | 20.6 | 24.0 |

Table 14. $\eta = 0.9$ raw experimental data.

| Run | η | δ | Volumetric flowrate [cc/min] | Measured power [W] | Estimated heat losses | Top plate temp [C] | Inlet temp [C] | Heater temp [C] |
|---|---|---|---|---|---|---|---|---|
| 16 | 0.90 | 1 | 0.0 | 0.72 | 10.8% | 20.7 | 20.4 | 24.6 |
| 17 | 0.90 | 1 | 0.0 | 3.52 | 3.9% | 20.8 | 19.3 | 29.6 |
| 18 | 0.90 | 1 | 0.0 | 12.91 | 2.0% | 20.9 | 19.8 | 39.1 |
| 19 | 0.90 | 1 | 8.4 | 0.60 | 13.1% | 20.6 | 20.4 | 24.4 |
| 20 | 0.90 | 1 | 8.4 | 2.71 | 4.6% | 20.8 | 20.6 | 28.5 |
| 21 | 0.90 | 1 | 8.4 | 10.14 | 2.2% | 20.8 | 20.3 | 36.7 |
| 22 | 0.90 | 1 | 26.6 | 0.81 | 10.3% | 20.8 | 20.7 | 25.1 |
| 23 | 0.90 | 1 | 26.6 | 2.68 | 4.6% | 20.9 | 20.7 | 28.5 |
| 24 | 0.90 | 1 | 25.7 | 8.18 | 2.5% | 21.2 | 20.6 | 35.2 |
| 25 | 0.90 | 1 | 87.0 | 1.37 | 7.4% | 20.6 | 20.5 | 26.5 |
| 26 | 0.90 | 1 | 87.0 | 4.07 | 3.7% | 20.8 | 20.6 | 30.8 |
| 27 | 0.90 | 1 | 83.1 | 10.55 | 1.9% | 21.1 | 20.6 | 35.2 |
| 28 | 0.90 | 1 | 241.7 | 2.31 | 5.2% | 20.7 | 20.6 | 28.1 |
| 29 | 0.90 | 1 | 241.7 | 6.77 | 2.8% | 20.8 | 20.7 | 33.7 |
| 30 | 0.90 | 1 | 241.7 | 16.34 | 1.8% | 20.8 | 20.5 | 42.1 |

Table 15. $\eta = 0.75$ raw experimental data.

| Run | η | δ | Volumetric flowrate [cc/min] | Measured power [W] | Estimated heat losses | Top plate temp [C] | Inlet temp [C] | Heater temp [C] |
|---|---|---|---|---|---|---|---|---|
| 31 | 0.75 | 1 | 0.0 | 1.22 | 8.2% | 21.1 | 20.8 | 26.4 |
| 32 | 0.75 | 1 | 0.0 | 4.80 | 3.4% | 20.9 | 20.0 | 31.7 |
| 33 | 0.75 | 1 | 0.0 | 16.10 | 1.8% | 21.1 | 20.3 | 42.4 |
| 34 | 0.75 | 1 | 7.4 | 1.05 | 9.2% | 20.6 | 20.2 | 25.9 |
| 35 | 0.75 | 1 | 9.4 | 4.54 | 3.5% | 21.0 | 20.6 | 31.5 |
| 36 | 0.75 | 1 | 10.3 | 15.86 | 1.9% | 20.9 | 20.1 | 42.3 |
| 37 | 0.75 | 1 | 25.7 | 0.76 | 11.4% | 20.9 | 20.7 | 25.1 |
| 38 | 0.75 | 1 | 25.7 | 2.84 | 4.6% | 20.9 | 20.6 | 29.1 |
| 39 | 0.75 | 1 | 25.7 | 14.24 | 2.0% | 21.0 | 20.1 | 41.1 |
| 40 | 0.75 | 1 | 87.0 | 1.08 | 8.8% | 20.7 | 20.4 | 25.9 |
| 41 | 0.75 | 1 | 87.0 | 3.34 | 4.2% | 20.7 | 20.4 | 29.8 |
| 42 | 0.75 | 1 | 87.0 | 9.21 | 2.4% | 21.0 | 20.5 | 36.7 |
| 43 | 0.75 | 1 | 241.7 | 1.78 | 6.2% | 21.0 | 20.8 | 27.3 |
| 44 | 0.75 | 1 | 241.7 | 5.21 | 3.3% | 21.0 | 20.8 | 32.2 |
| 45 | 0.75 | 1 | 241.7 | 12.88 | 2.1% | 21.1 | 20.8 | 40.0 |

Table 16. $\eta = 0.5$ raw experimental data.

| Run | η | δ | Volumetric flowrate [cc/min] | Measured power [W] | Estimated heat losses | Top plate temp [C] | Inlet temp [C] | Heater temp [C] |
|---|---|---|---|---|---|---|---|---|
| 46 | 0.50 | 1 | 0.0 | 2.01 | 5.5% | 20.3 | 20.2 | 27.4 |
| 47 | 0.50 | 1 | 0.0 | 7.70 | 2.7% | 20.7 | 20.4 | 35.3 |
| 48 | 0.50 | 1 | 0.0 | 23.67 | 1.6% | 21.0 | 20.2 | 49.0 |
| 49 | 0.50 | 1 | 6.5 | 1.99 | 5.9% | 20.8 | 20.6 | 27.9 |
| 50 | 0.50 | 1 | 7.4 | 7.70 | 2.8% | 21.0 | 20.9 | 35.7 |
| 51 | 0.50 | 1 | 5.5 | 23.88 | 1.6% | 21.1 | 20.5 | 49.4 |
| 52 | 0.50 | 1 | 26.6 | 1.92 | 6.0% | 20.6 | 20.6 | 27.6 |
| 53 | 0.50 | 1 | 26.6 | 7.35 | 2.8% | 21.0 | 20.7 | 35.3 |
| 54 | 0.50 | 1 | 25.7 | 23.44 | 1.6% | 21.2 | 20.6 | 49.3 |
| 55 | 0.50 | 1 | 87.0 | 1.10 | 8.3% | 20.7 | 20.8 | 25.8 |
| 56 | 0.50 | 1 | 87.0 | 7.03 | 2.9% | 20.9 | 20.8 | 35.1 |
| 57 | 0.50 | 1 | 87.0 | 21.67 | 1.7% | 21.3 | 20.5 | 47.9 |
| 58 | 0.50 | 1 | 255.6 | 1.63 | 6.6% | 20.8 | 20.8 | 27.1 |
| 59 | 0.50 | 1 | 255.6 | 4.84 | 3.5% | 21.0 | 20.9 | 32.1 |
| 60 | 0.50 | 1 | 255.6 | 12.20 | 2.2% | 21.1 | 20.9 | 40.1 |

Table 17. $\eta = 0$ raw experimental data.

| Run | η | δ | Volumetric flowrate [cc/min] | Measured power [W] | Estimated heat losses | Top plate temp [C] | Inlet temp [C] | Heater temp [C] |
|---|---|---|---|---|---|---|---|---|
| 61 | 0 | 1 | 0.0 | 4.31 | 1.4% | 21.0 | 20.1 | 24.0 |
| 62 | 0 | 1 | 0.0 | 15.54 | 0.7% | 21.0 | 19.8 | 27.7 |
| 63 | 0 | 1 | 0.0 | 45.28 | 0.4% | 21.1 | 19.8 | 34.1 |
| 64 | 0 | 1 | 10.3 | 4.31 | 1.5% | 20.9 | 20.6 | 24.3 |
| 65 | 0 | 1 | 5.5 | 15.24 | 0.7% | 20.9 | 20.3 | 27.4 |
| 66 | 0 | 1 | 9.4 | 45.31 | 0.4% | 21.2 | 20.1 | 34.5 |
| 67 | 0 | 1 | 25.7 | 4.25 | 1.7% | 21.0 | 20.9 | 25.0 |
| 68 | 0 | 1 | 25.7 | 15.54 | 0.6% | 20.8 | 20.5 | 27.2 |
| 69 | 0 | 1 | 25.7 | 45.44 | 0.4% | 20.9 | 19.8 | 34.6 |
| 70 | 0 | 1 | 87.0 | 3.36 | 1.7% | 21.1 | 20.7 | 23.8 |
| 71 | 0 | 1 | 86.0 | 12.06 | 0.8% | 20.7 | 19.7 | 26.5 |
| 72 | 0 | 1 | 87.0 | 45.61 | 0.4% | 21.2 | 20.3 | 34.1 |
| 73 | 0 | 1 | 227.8 | 3.62 | 1.7% | 21.4 | 21.1 | 24.2 |
| 74 | 0 | 1 | 269.5 | 12.95 | 0.7% | 21.0 | 20.2 | 26.5 |
| 75 | 0 | 1 | 255.6 | 36.59 | 0.4% | 21.0 | 20.0 | 32.2 |

## B – Uncertainty Analysis

A standard approach to the uncertainty was used to estimate the error in the experimental data of the present study. In this approach, to calculate the uncertainty of a function, the partial derivative of that function with respect to each independent variable is taken and the square root of the sum of the squares is used as the uncertainty according to the following formula,

$$\frac{\Delta F}{F} = \sqrt{\left(\frac{\partial F/\partial a}{F}\right)^2 + \left(\frac{\partial F/\partial b}{F}\right)^2 + \left(\frac{\partial F/\partial c}{F}\right)^2 + \cdots}, \tag{125}$$

where $\Delta F$ represents the expected error in the value of F.

Table 18. Error of various parameters used in the uncertainty analysis.

| | Error used in uncertainty analysis |
|---|---|
| Heater power | 1.5% |
| Thermocouple temperature | 0.5 $^{o}$C |
| Thermal conductivity | 2.5% |
| Volumetric flowrate from rotameter | 8% |
| Volumetric expansion coefficient | 5% |
| Diameter of glass beads | 3% |
| Porosity | 5.3% |

The heater power error was provided in the user manual for the power supplies. The thermocouple temperature error is commonly used and was confirmed to be approximately accurate by allowing the entire test apparatus to reach a constant temperature overnight and observing the spread of all of the thermocouples, which was approximately half of a degree Celsius. The thermal conductivity error of 2.5% is approximate based on the findings of Aichlmayr [14]. The flowrate uncertainty was provided in the specification sheets from the manufacturer of the rotameters. The uncertainty in the volumetric expansion coefficient was approximated by allowing the temperature to vary by +/- 0.5 $^{o}$C, resulting in a 5% shift in the value. The diameter of

glass beads plays a rather insignificant part in the overall uncertainty of the system, even when increased substantially, so an estimate of roughly 3% was determined to be acceptable. The porosity error was determined by the range of porosity values given for spherical packings [2].

Using the values in Table 18, the error in the Nusselt number, Rayleigh number, and Peclet number was estimated for each of the 75 experimental runs performed. Thermophysical properties were calculated using EES software at atmospheric pressure and at the average of the heater and free stream temperatures. Heat losses were estimated using a one-dimensional conduction model as described in the Experimental Results chapter. Detailed results are also found in the Experimental Results chapter.

## C – Drawings of the Apparatus

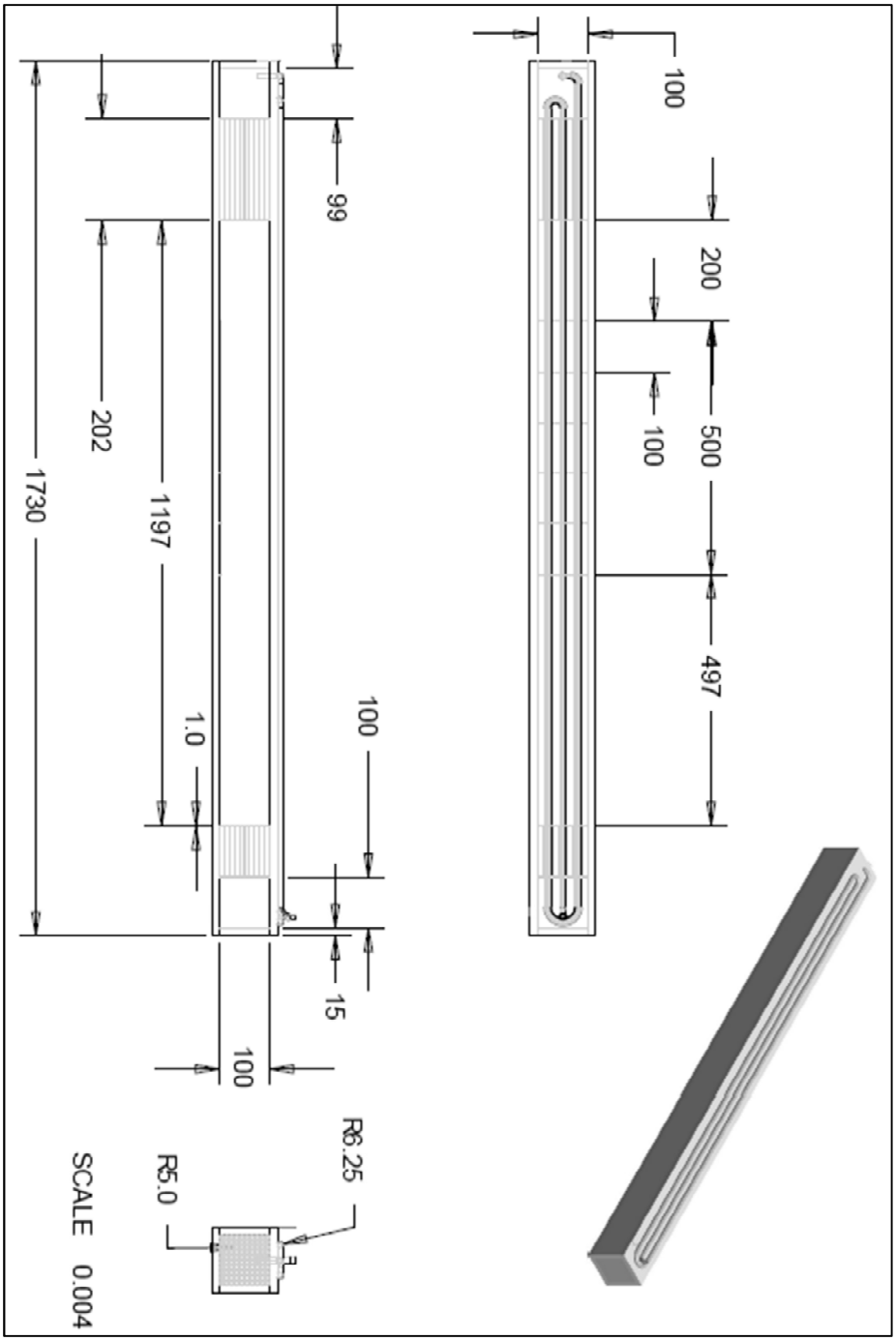

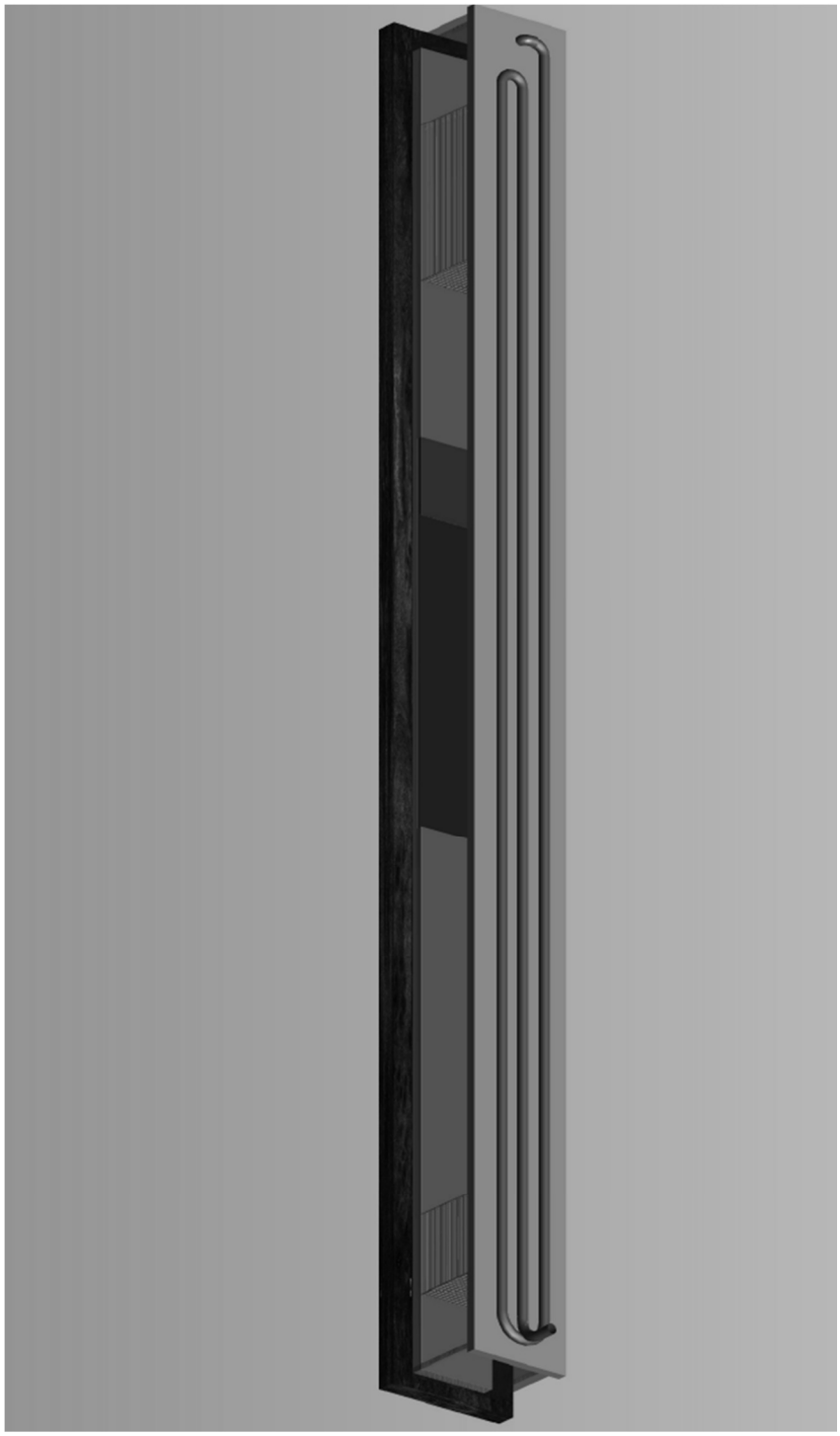

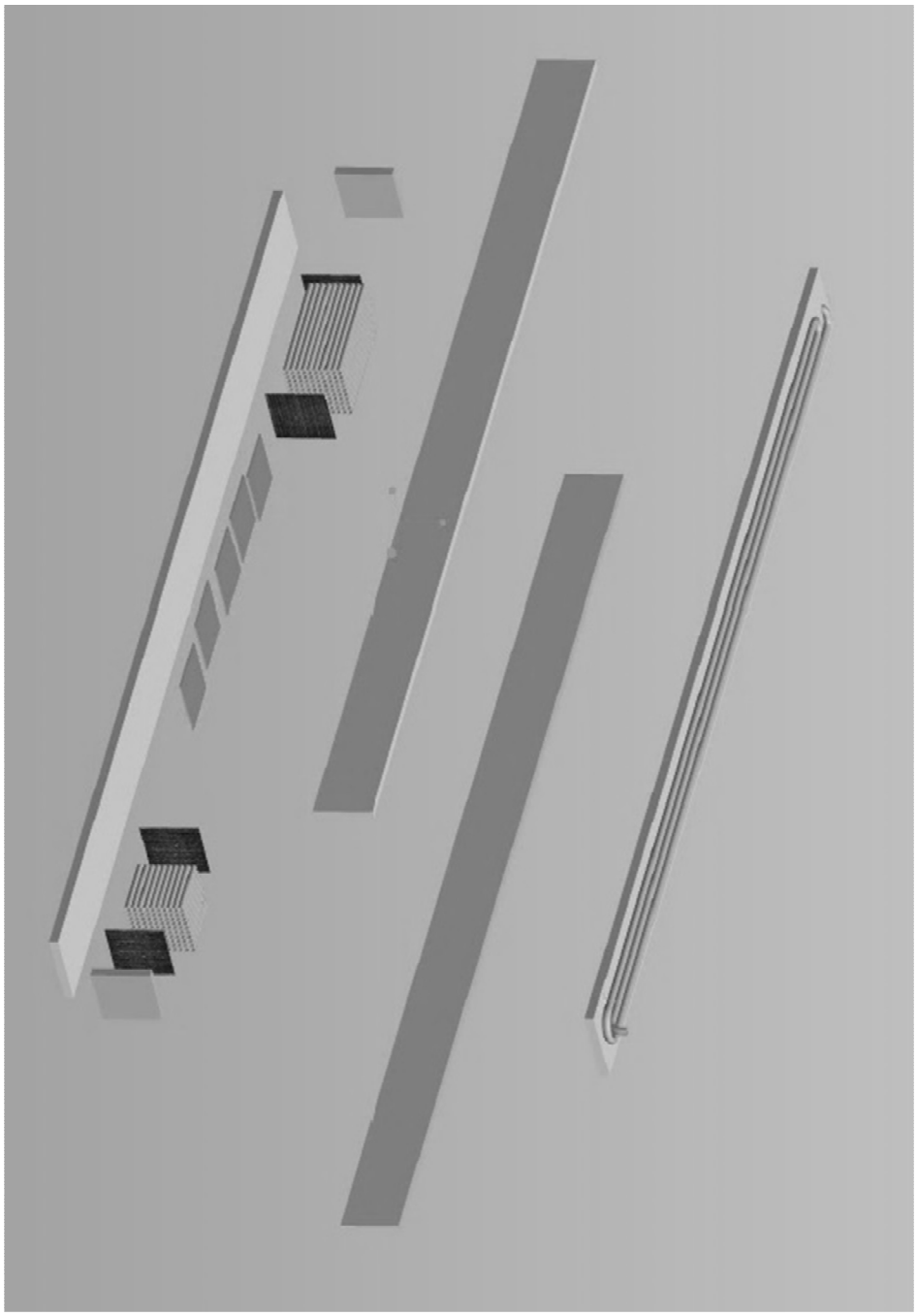

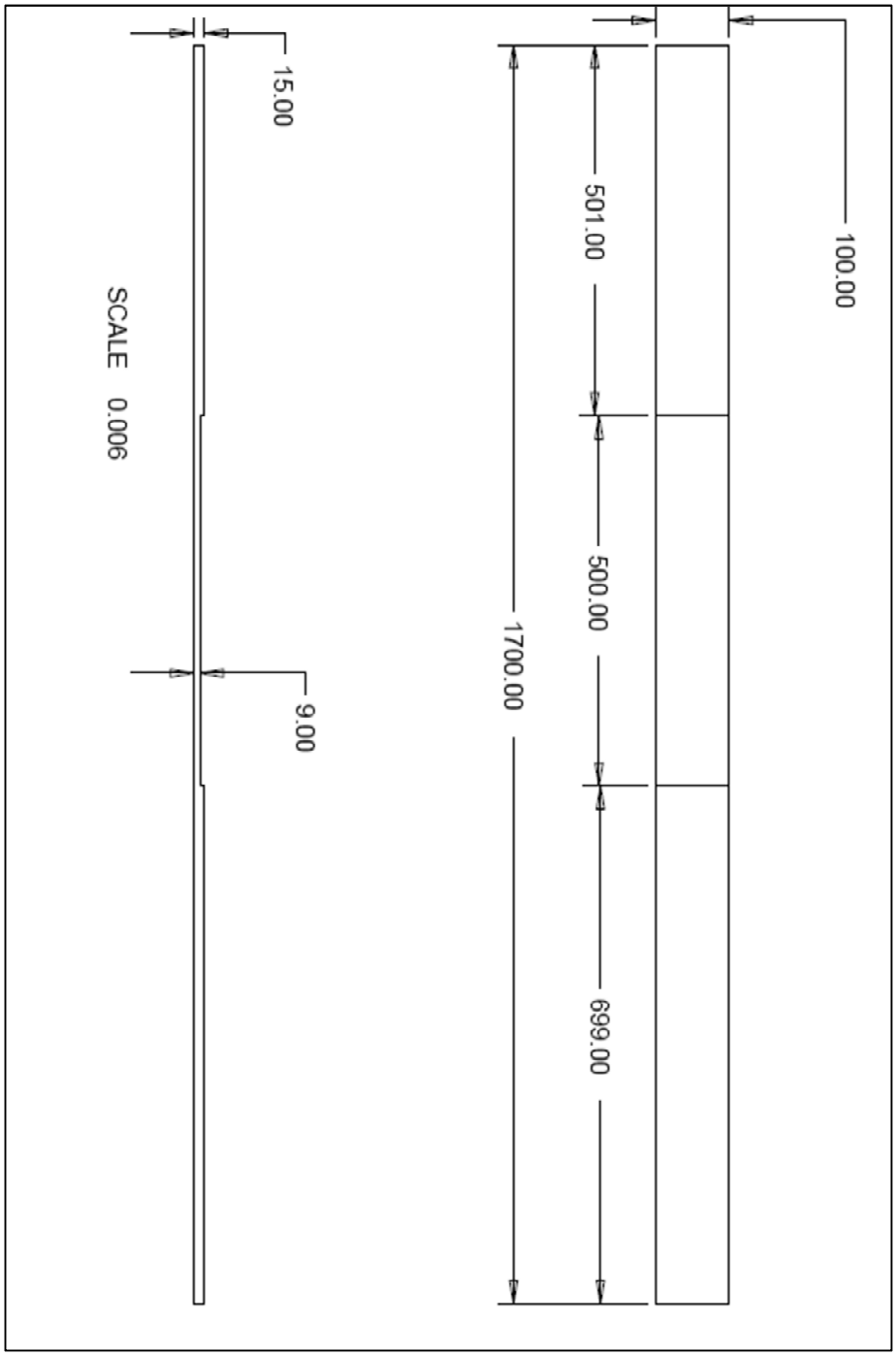
100.00
501.00
500.00
699.00
1700.00
15.00
9.00
SCALE 0.006

## D – Numerical comparison of variable porosity terms

The variable porosity terms were turned on and off to investigate the impact on the overall Nusselt number of the system. In addition, the streamlines and velocity profiles were plotted for further comparison. As can be seen, without the variable porosity terms, an unrealistic flow field develops, where the flow velocities are higher in the porous region instead of the less-restricted fluid region. It is believed that this is a result of the stream function-vorticity method, although it is not fully understood.

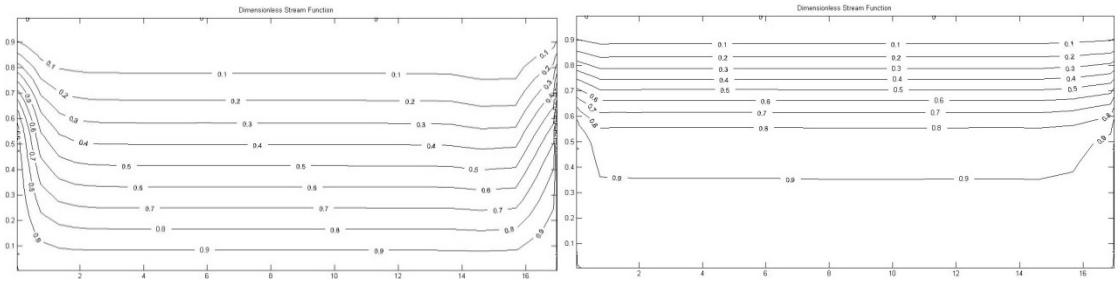


Figure 103. Streamlines for η = 0.5, RaDa = 1, Pe = 300 a) without variable porosity terms b) with variable porosity terms

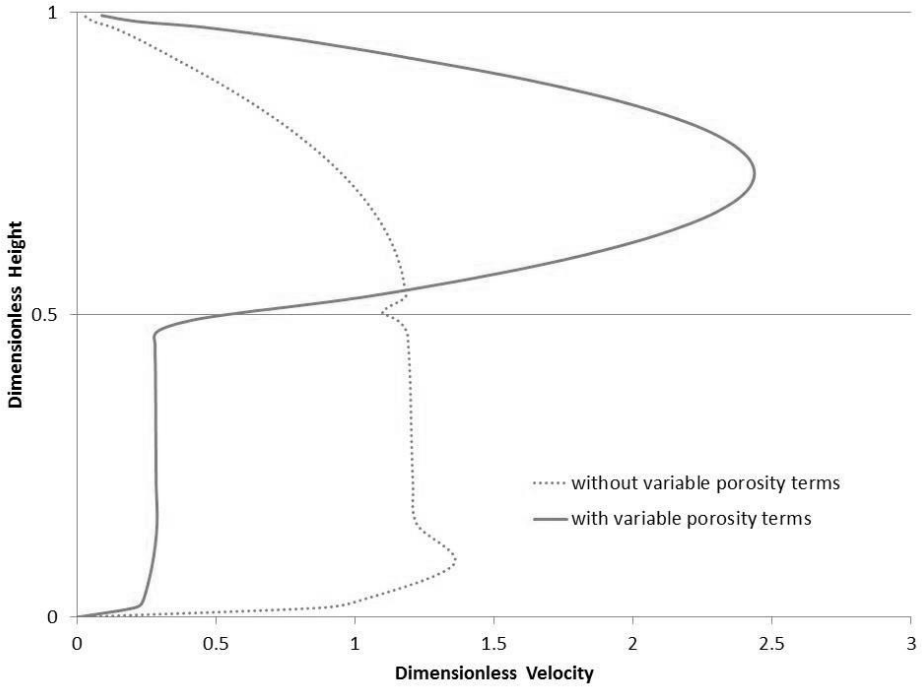


Figure 104. Velocity profile for η = 0.5, RaDa = 1, Pe = 300 with and without variable porosity terms.